EUROPEAN ORGANIZATION FOR NUCLEAR RESEARCH

L3 Note 2241
March 24, 1998

Standard Model Higgs Searches at $\sqrt{s}$=183 GeV

L3 Higgs Working Group: M.Biasini, J.Branson, F.DiLodovico, A.Dominguez, J.P.Ernenwein, R.Faccini, M.Felcini, I.Fisk, S.Hou, A.Kopp, A.Kunin, J.P.Martin, M.Pieri, G.Raven, I.Vorobiev

Abstract

Searches for the Standard Model Higgs boson are performed with the data sample collected by the L3 experiment at centre of mass energies of about 183 GeV with an integrated luminosity of 55.3 pb^{-1}. The observed candidates are in agreement with the expectations from Standard Model processes without a Higgs signal. The lower Higgs mass limit is found to be in the range 87.3 – 87.8 GeV.

1 Introduction

This note describes all the analyses done to search for the SM Higgs boson in the data collected by the L3 experiment in 1997, when the centre of mass energy was raised up to about 183 GeV. The SM Higgs mass lower limit previously published by L3 was 69.5 GeV. The increase in the centre of mass energy allowed to extend the search in the mass region up to about 90 GeV.

2 Data and Monte Carlo samples

SM processes	cross-section (pb)	Generator	Events
$\gamma\gamma \to \mathrm{ee q\bar{q}}$	$13.5 \cdot 10^3$	Pythia	10^6
$\mathrm{q\bar{q}}(\gamma)$	105.3 (Zfitter)	Pythia	728000
Zee	3.26	Pythia	26800
$\mathrm{Z}/\gamma^*\mathrm{Z}/\gamma^* \to$all	0.594	Pythia	29600
$\mathrm{Z}/\gamma^*\mathrm{Z}/\gamma^* \to$qqee	0.672	Excalibur	
$\mathrm{W/W^*W/W^*} \to \mathrm{q\bar{q}'}e\nu$		Excalibur	40000
WW$\to$ all	15.5	Koralw	252800

Table 1: Standard Model processes cross sections, generators, and number of MC events, at $\sqrt{s}$ =182.72. GeV, used in the analysis. All the cross sections are those calculated by the generators mentioned in the table, except for $\mathrm{q\bar{q}}(\gamma)$ production, for which the cross section is calculated with Zfitter for $\sqrt{s'} > 10$ GeV (cut also applied to the Pythia generated $\mathrm{q\bar{q}}(\gamma)$ events).

3 The $HZ \to q\bar{q}q'\bar{q}'$ channel

3.1 Weight analysis

The weight analysis as described in detail in [1] and published in [2] has been repeated on 1997 data.

No bad runs are subtracted but, in order to account for the incorrect simulation of the bad runs of the TEC both background and signal expectations are scale of 3%. The considered integrated luminosity is 55.3 pb^{-1}.

Table 2 reports the tight and loose cuts used both in the construction of the ξ variable and for the preselection (the loose ones). The tight cuts were obtained optimising the selection for 100pb^{-1}, the loose ones for 10^{-1} for $M_H = 80$ GeV. With respect to the previous runs the importance of the y_{cut} has increased and above all the cuts devised against the WW background have gained relevance. Only one cut that was not found to be useful previously has been introduced: the maximum angle between pairs of jets ($\Delta\theta$).

After these cuts 385 events survived with 278.0 events expected from WW, 63.0 events from QQ and 8.4 events from ZZ (349.4 in total). The efficiency on an 85 GeV Higgs Boson (H→ $b\bar{b}$) is 77.2%.

The tagging variable, combination of the 3D NNET outputs per jet, whose integrated distribution is shown in figure 1, is then required to be greater than 1.6. 26 events survive the selection with 13.5 expected from WW, 12.7 from QQ and 2.1 from ZZ(28.3 in total). The efficiency is 46.8%. Figure 2 shows the distributions of the ξ, $\chi 2$ and D_{tag} variables after the selection on data, background and 85 GeV signal. Figure 3 shows the background expectations versus the efficiency for an 85 GeV Higgs boson. As far as the mass dependence is concerned at 60fb of background the efficiency for Higgs bosons of 75,80 and 85 GeV of mass the efficiencies are 20.5,25.1 and 28.7% respectively. The drop in efficiency is related to the preselection criteria that reject topologies close to the W one, that is Higgs masses close to 70 GeV. Figure 4 shows the number of events expected from the background and found of data above a given value of the weight (in abscissa), for the hypothesis $M_H = 85$ GeV. The lower plot shows the mass dependence of the weight: applying the weight with a mass hypothesis which is 5 GeV wrong (about 2 times the resolution) the performances are reduced in the relevant region of a factor about 2. That is why the search is performed scanning on all the mass hypothesis with a 100 MeV step. It is to be noted that the mass does not enter explicitly in the weight calculation, but indirectly in the evaluation of the χ^2.

Table 2: The two sets of cuts used in the construction of the ξ variable for the four jets channel.

cut		loose selection	tight selection
$N_{\rm gtk}$	>	20.1	20.1
$N_{\rm cl}$	>	40.1	40.1
$\frac{E_{\rm vis}-\sqrt{s}}{\sqrt{s}}$	<	0.381	0.317
$\cos\theta_{\rm th}$	<	0.999	0.964
$\frac{M_{vis}}{\sqrt{s}}$	>	0.400	0.400
$\sqrt{\frac{s'}{s}}$	>	0.601	0.627
Y_{34}	>	0.0055	0.0437
$\cos(\theta_{\rm J})$	<	0.99	0.99
$\frac{E_{min}}{\sqrt{s}}$	>	0.0234	0.154
$\frac{E_\gamma}{E_{jet}}$	<	0.969	0.909
$\frac{\Delta E_{ij}}{\sqrt{s}}$	<	0.857	0.254
$\frac{M_{ij}^{\rm min}}{\sqrt{s}}$	>	0.113	0.208
$\frac{M_{ij}^{\rm max}}{\sqrt{s}}$	<	0.659	0.574
$\cos(\Delta\theta)$	>	-0.9938	-0.8455

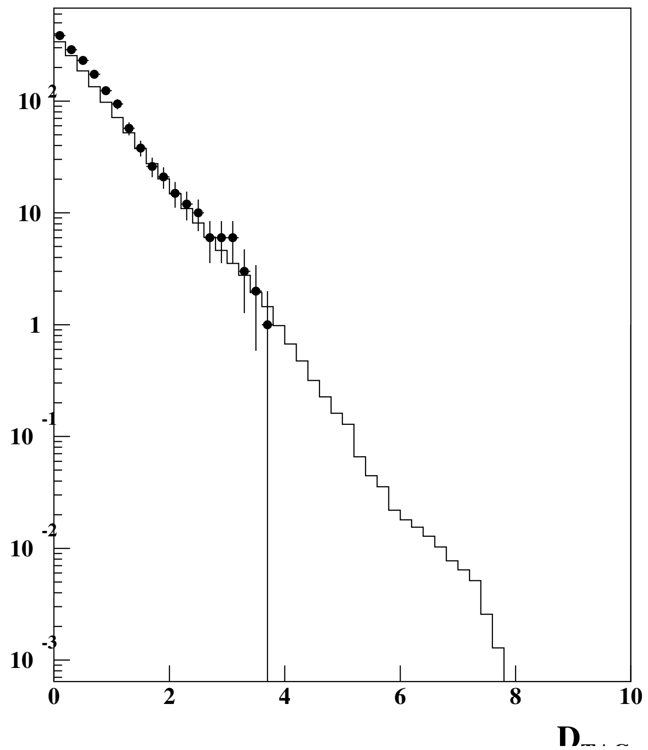

Figure 1: Integrated distribution of the B-tagging discriminant after the kinematic preselection.

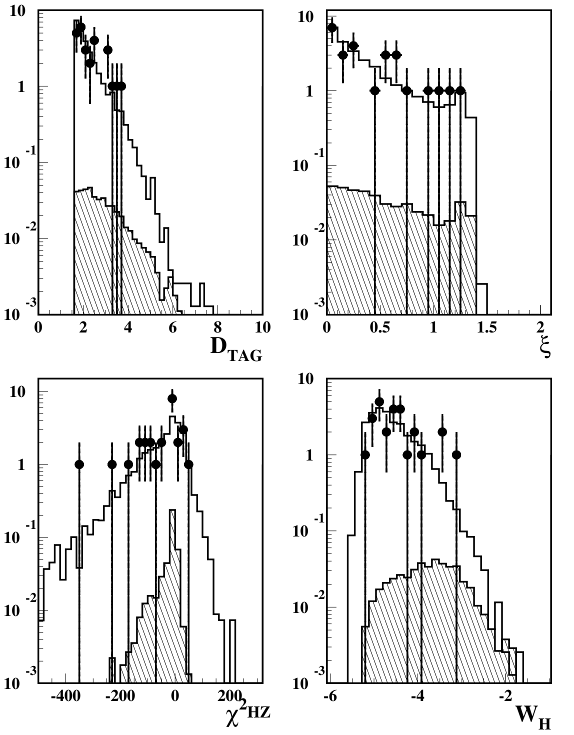

Figure 2: Distribution of the ingredients of the weight and of the weight itself on background, data and signal (arbitrary scale).

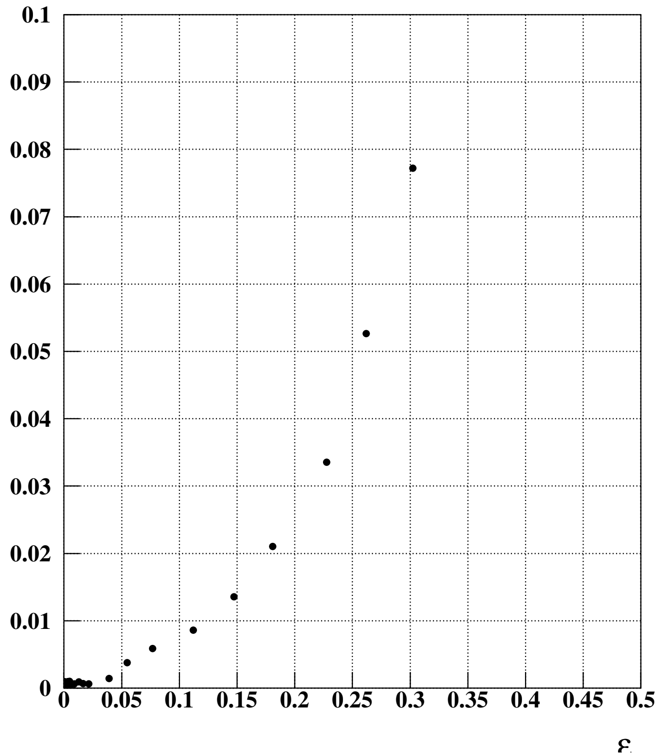

Figure 3: Background expectations as a function on the efficiency on an 85 GeV Higgs boson (H→ $b\bar{b}$)

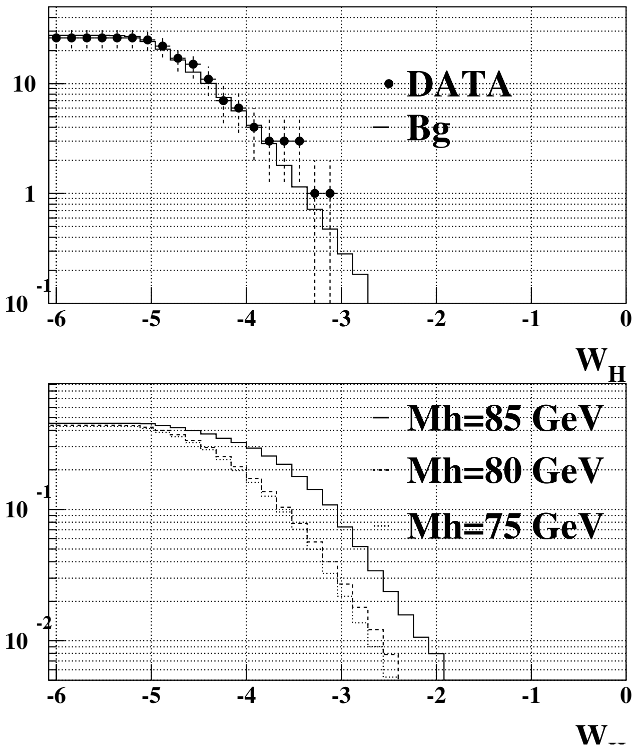

Figure 4: Integrated distribution of the weight for $M_H = 85$ GeV. The lower plot shows the integrated efficiency for the correct mass hypothesis and for other two signal on which the wrong mass hypothesis has been done.

3.2 Optimised cuts and discriminant analysis

This analysis is similar in spirit to the weight analysis described in Section 3.1 since it uses simple cuts and combines a few powerful variables in one final variable to distinguish signal from background. The integrated luminosity used was 55.3 pb^{-1}and the same philosophy regarding "bad TEC runs" was used as in the weight analysis.

Even though the centre-of-mass energy varied ($\sqrt{s} = 180.8, 181.7, 182.7, 183.8$ GeV), 90% of the data were collected at 182.7 GeV. In addition, the Monte Carlo (MC) simulations were performed at 182.7 GeV, subsequently, the analysis was optimised at this centre-of-mass energy and the cross-sections corresponding to this $\sqrt{s}$ were used to weight the MC signal and background events.

3.2.1 B-Tagging

The identification of events enriched with b-hadrons is central to the H$q\bar{q}$ channel at these centre-of-mass energies and is explained in detail in [2,3]. The only important difference in the b-tag (other than bug fixes) this year as compared to last is in the use of the N-event vertex [4] instead of the fill vertex as a constraint for the primary vertex. Since the beam optics used in the 1997 runs increased the size of the beam-spot to 42μm in Y and 220μm in X, the N-event vertex was given a weight of $1/(42\mu\text{m})^2$ in Y and $1/(220\mu\text{m})^2$ in X during the primary vertex fit.

3.2.2 Preselection

The analysis relies on three levels of selection to arrive at a single "final" variable. The first level of cuts is called the preselection because it is designed to select full energy, high multiplicity, hadronic events with a high number of jets and reduces the data set from 3.7 million pass-1 events to approximately 650 events while keeping the signal efficiency very high. The preselection cuts are listed in Table 3 and the number of observed events, MC background and signal efficiencies are shown in Table 5.

The only exceptional cut is the one placed on the maximum energy in the EGAP calorimeter since it is not specifically designed to separate signal and background. This cut is made to avoid selecting events with too much noise in the EGAP, but is, otherwise, an extremely loose cut. The MC background and signal events are then fed to a cut optimiser which chooses the second set of selection cuts to maximise the exclusion potential of the H$q\bar{q}$ channel.

3.2.3 The final variable and cut optimisation

The cut optimiser employs the simple method of analysis optimisation outlined in [5] which is, in fact, the basis for the final confidence level (CL) calculations presented in Section 7.3. The optimiser has two main ingredients–the building of a final variable, and the calculation of the CL from the distributions of this variable for MC background and signal.

Cut		Hadronic Selection
Number of ASRC's	$\geq$	45
Number of good tracks	$\geq$	15
Visible Energy/$\sqrt{s}$	$\geq$	0.60
Visible Energy/$\sqrt{s}$	$\leq$	1.40
Perpendicular Energy Imbalance	$\leq$	0.40
Parallel Energy Imbalance	$\leq$	0.30
Maximum Photon Energy	$\leq$	$0.1 \cdot \sqrt{s}$
Maximum Lepton Energy	$\leq$	50.0 GeV
$\sqrt{s'}/\sqrt{s}$	$\geq$	0.80
Y34(DURHAM)	$\geq$	0.002
Total EGAP Energy	$\leq$	80.0 GeV

Table 3: The cuts used for high multiplicity hadronic selection.

The final variable consists of a combination of b-tag and mass χ^2 for events that pass the preselection and the optimised cuts listed in the left hand column of Table 4. The preselected events are forced to have exactly four jets using the DURHAM algorithm and the neural network b-tag [3] is considered for each jet. The b-tagging variable actually used in the analysis describes the probability that all four jets are consistent with jets containing no b quarks. This probability is estimated using the jet-tags for the MC background events that have passed preselection and contain no b-hadrons (shown in Fig. 5a as the histogram with the solid line). This histogram is normalised and integrated bin-by-bin and used to give the confidence level, P_j^{jet}, that a jet is consistent with containing no b hadrons. The confidence levels for all four jets in the event are then combined into a single confidence level which is then used to define the b-tag variable, $B_{\mathrm{tag}}^{\mathrm{event}}$ (see Fig. 5b),

$$B_{\mathrm{tag}}^{\mathrm{event}} = -\log(\Pi_0 \sum_{i=0}^{3} \frac{(-\ln \Pi_0)^i}{i!}), \quad \text{where } \Pi_0 = \prod_{j=1}^{4} P_j^{jet}. \tag{1}$$

After the preselected events are forced into a four jet configuration, a (4C) kinematic fit is performed with a 4-momentum conservation constraint to improve the jets' energy resolution. The one jet combination out of the possible three that minimises the following mass χ^2 is chosen,

$$\min(\chi_i^2) = \min\left((\Sigma - (m_i + m_i')^2/(4\ \mathrm{GeV})^2 + (\Delta - |m_i - m_i'|)^2/(6\ \mathrm{GeV})^2)\right),$$

where Σ and Δ are $(m_{\mathrm{Z}} + m_{\mathrm{H}})$ and $|m_{\mathrm{Z}} - m_{\mathrm{H}}|$, respectively, and m_i and m_i' are the two dijet masses in the i^{th} jet combination.

The mass χ^2 variable, χ_{mass}, is then defined to be

$$\chi_{\mathrm{mass}} = \log(Prob(\min(\chi_i^2))), \tag{2}$$

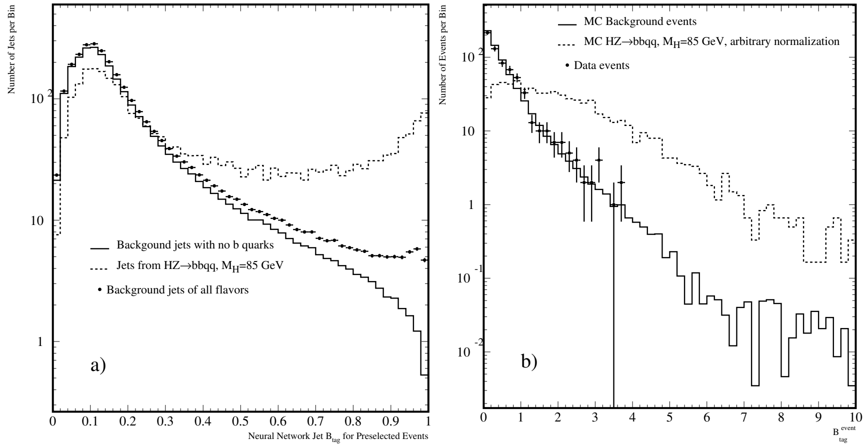

Figure 5: **a)** Output of neural network jet tag on MC jets for events passing the preselection. The neural network b-tag for MC jets with no b-hadrons (solid histogram) is integrated and normalised and then used to calculate the probability, P_j^{jet}, to have a neural network output greater than the one observed. The P_j^{jet} for all four jets are then combined into a single probability, $B_{\mathrm{tag}}^{\mathrm{event}}$ (see Eq. 1). The dotted histogram shows the jet tag for an 85 GeV Higgs signal, arbitrarily normalised. **b)** $B_{\mathrm{tag}}^{\mathrm{event}}$ for the data (dots), MC background (solid histogram) and 85 GeV $\mathrm{Hq\bar{q}}$ signal (dotted histogram).

where $Prob$ is the χ^2 probability function with two degrees of freedom. The distribution of χ_{mass} for MC and data is shown in Fig. 6 after the preselection cuts have been applied for the Higgs mass hypothesis $m_{\mathrm{H}} = 85$ GeV.

The $B_{\mathrm{tag}}^{\mathrm{event}}$ and χ_{mass} variables are combined into a single variable in much the same way as the four neural net b-tags are combined into an event tag in Eq. 1. In place of the jet probabilities, P_j^{jet}, the probabilities for $B_{\mathrm{tag}}^{\mathrm{event}}$ and χ_{mass} to each be consistent with their respective MC background distributions is calculated and the sum and product in Eq. 1 only runs to 2 instead of 4. This variable is called $F(m_{\mathrm{H}})$ and depends on the Higgs mass hypothesis. The binned distribution of $F(m_{\mathrm{H}})$ for MC background and signal events passing a given set of cuts is then used to calculate the CL.

The CL is chosen to maximise the $\mathrm{Hq\bar{q}}$ channel's contribution to the final likelihood

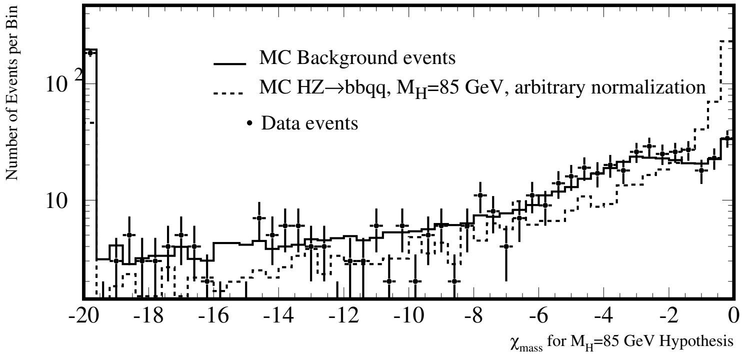

Figure 6: χ_{mass} variable after preselection for the data (dots), MC background (solid histogram), and $\mathrm{Hq\bar{q}}$ signal for $m_{\mathrm{H}} = 85$ GeV arbitrarily normalised (dotted histogram). All values of $\chi_{\mathrm{mass}} < -20$ are placed in the left-most bin at -20.

used in Section 7.3. The optimised CL is defined to be, $\widehat{CL}$,

$$L(s,b) = e^{-(s+b)} \prod_{i=1}^{N_{\mathrm{bins}}} \frac{(f_i+g_i)^{g_i}}{\Gamma(g_i+1)} \tag{3}$$

$$\widehat{CL} = \frac{\int_{\sigma}^{\infty} L(s,b)ds}{\int_{0}^{\infty} L(s,b)ds} \ ,$$

where s and b are the total number of selected signal and background events passing a given set of cuts and f_i and g_i are the number of signal and background events in a given bin of the distribution of the final variable, $F(m_{\mathrm{H}})$, for signal and background, respectively. The total number of expected $\mathrm{Hq\bar{q}}$ signal events, σ, depends on m_{H} through the cross section. The gamma function, $\Gamma(g_i+1)$, is used in place of the factorial because the bin contents, g_i, need not be integers.

$\widehat{CL}$ is an estimate of the average Bayesian confidence level for the upper limit σ. Since $\widehat{CL}$ is only an estimator for the Bayesian average, the cut optimiser suffers somewhat from the statistical fluctuations due to the imperfect approximation of the true average. However, a trade off of accuracy for speed had to be made since the many iterations of the cut optimiser would have made the true average calculation prohibitively slow.

The variables and their cuts which are optimised by minimising Eq. 3 are listed in Table 4.

Variable		Optimised Cut
Minimum Dijet Mass/$\sqrt{s}$	$\geq$	0.143
Maximum Dijet Mass/$\sqrt{s}$	$\leq$	0.658
Minimum Jet Energy/$\sqrt{s}$	$\geq$	0.123
$\cos\theta$ minimum between jets	$\geq$	-0.9945
Maximum ΔE of jets	$\leq$	0.223
Y34 Durham	$\geq$	0.4368E-02
Visible Energy/$\sqrt{s}$	$\geq$	0.647
Parallel Imbalance/$\sqrt{s}$	$\leq$	0.261
χ_{mass}	$\leq$	-13.29
$B_{\mathrm{tag}}^{\mathrm{event}}$	$\geq$	0.0641

Table 4: The cuts returned by the cut optimiser, rounded to the nearest digit of precision.

3.2.4 Optimisation of Weighted Final Variable

The last stage of the analysis deals with the relative distinguishing power that the χ_{mass} and $B_{\mathrm{tag}}^{\mathrm{event}}$ variables separately bring with them to the final variable. These two variables do not necessarily have the same ability to separate signal from background and to use the unweighted combination of their background probabilities as in Eq. 1 could be suboptimal. After all the optimised cuts of Table 4 have been applied, the relative weight, α, is optimised by once again minimising $\widehat{CL}$. However, instead of using $F(m_{\mathrm{H}})$ as the final variable, the same technique as the weighted 3D b-tag [2,3] is used to combine $B_{\mathrm{tag}}^{\mathrm{event}}$ and χ_{mass} into a final variable, $F_w(m_{\mathrm{H}})$:

$$F_w(m_{\mathrm{H}}) = -\log\left(\frac{\alpha P_B^{1/\alpha} P_\chi - P_B P_\chi^\alpha}{\alpha - 1}\right), \tag{4}$$

where P_B and P_χ are the probabilities of the $B_{\mathrm{tag}}^{\mathrm{event}}$ and χ_{mass} each being consistent with their respective background distributions.

The optimal weight was found to be $\boldsymbol{\alpha = 1.13}$.

3.2.5 Results

The distribution of the weighted final variable, $F_w(m_{\mathrm{H}})$, for an 85 GeV Higgs after all the optimised cuts have been applied is shown in Fig. 7.

The results of the analysis at different stages is shown in Tables 5 and 6. Since χ_{mass} depends on m_{H}, the cut on this variable changes the number of accepted data and background MC for different m_{H} hypotheses in the final set of cuts.

Up to this point, only the $\mathrm{HZ} \to \mathrm{b\bar{b}q\bar{q}}$ contribution to the $\mathrm{Hq\bar{q}}$ channel has been discussed. Even though the analysis was optimised for the $b\bar{b}$ decay mode of the H, there

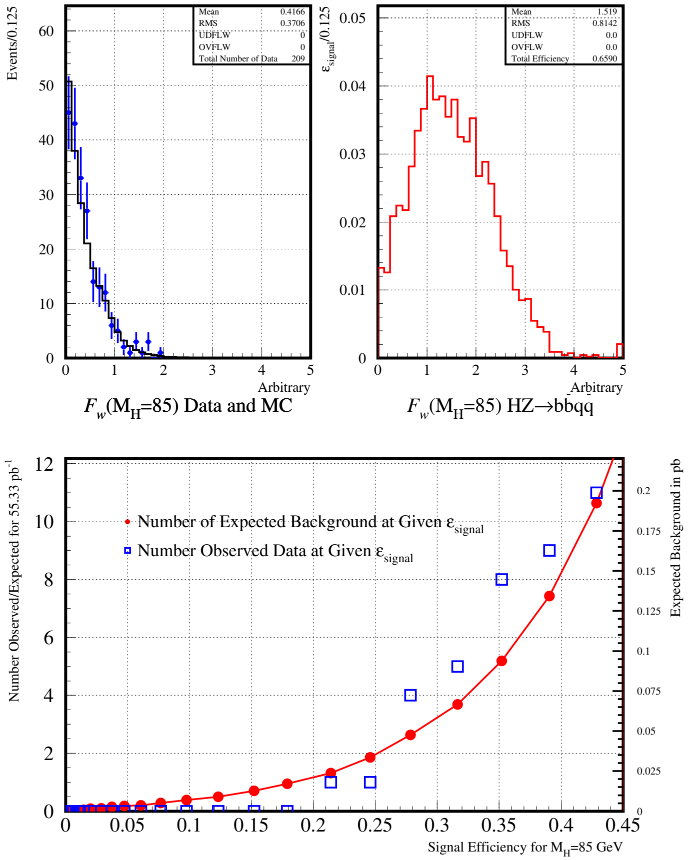

Figure 7: The final variable, $F_w(m_{\mathrm{H}})$ (see Eq. 4), for data, MC and signal after all optimised cuts have been applied. Shown in the lower plot is the profile of the bin-by-bin integration for a portion of the upper plots.

Analysis Stage	Data	All background	$q\bar{q}$	WW	ZZ	HZ (85 GeV)
Preselected	652	655.6	296.4	348.9	11.5	91.2%
Optimised	251	237.1	27.2	204.5	5.5	67.1%
Final(85 GeV)	209	201.2	23.9	172.5	4.8	65.9%

Table 5: Analysis flow. Observed data and MC background are listed in numbers of events, while the efficiency for the 85 GeV $\mathrm{HZ} \to \mathrm{b\bar{b}q\bar{q}}$ signal is shown in the last column. For the optimised cuts row, the cuts on $B_{\mathrm{tag}}^{\mathrm{event}}$ and χ_{mass} *have not* been applied, whereas for the final cuts row, they have been applied.

Stage	HZ (87 GeV)	HZ (85 GeV)	HZ (80 GeV)	HZ (75 GeV)
ϵ_{pre} for HZ	91.1%	91.2%	89.8%	88.9%
ϵ_{opt} for HZ	66.2%	67.1%	61.7%	56.8%
ϵ_{fin} for HZ	65.0%	65.9%	60.4%	56.4%
N_{data} Final	208	209	211	211
$N_{\mathrm{background}}$ Final	199.2	201.2	203.0	203.3

Table 6: Analysis flow for different signal mass points and the number of observed data events and expected background after the final set of cuts for different mass hypotheses.

is, nevertheless, some sensitivity to the less important decay modes $\mathrm{HZ} \to \mathrm{c\bar{c}q\bar{q}}$ and $\mathrm{ggq\bar{q}}$. These have been included with their proper (mass dependent) branching fractions in the total $\mathrm{Hq\bar{q}}$ signal efficiency as shown in Figure 8 and have been used in the calculation of the mass limit (see Section 7.3).

The candidates in data for the 85 and 80 GeV mass hypothesis are shown in Table 7.

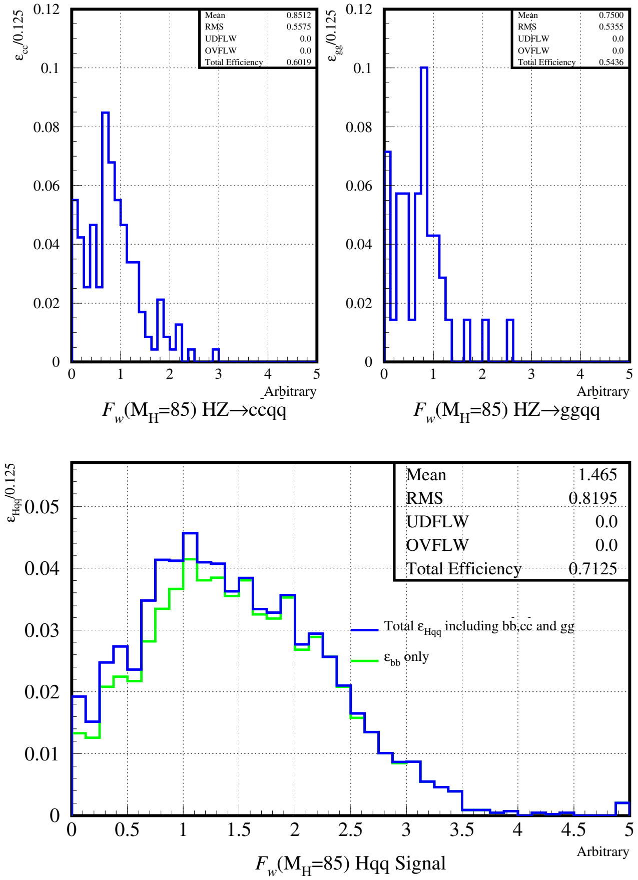

Figure 8: Charm and gluonic decay modes of the H. Shown in the upper two plots are the distributions for $F_w(m_{\mathrm{H}}=85)$ for $\mathrm{HZ}\to \mathrm{c\bar{c}q\bar{q}}$ and $\mathrm{ggq\bar{q}}$. In the lower plot the final variable for the charm, gluon and bottom decay modes of the H have been added, weighted with their respective branching ratios. The total $\mathrm{Hq\bar{q}}$ efficiency is compared to the $b\bar{b}$ mode.

m_{H}	Run	Event	$F_w(m_{\mathrm{H}})$	$B_{\mathrm{tag}}^{\mathrm{event}}$	M_{dijets1}	M_{dijets2}	M_{dijets3}
85 GeV	673208	1033	1.73	1.44	(66.0,31.4)	(99.0,63.9)	**(85.8,89.6)**
	677512	1432	1.73	2.50	(105.2,44.7)	(74.2,50.9)	**(91.7,78.2)**
	680911	1082	1.68	3.76	(107.9,43.1)	(79.9,52.4)	**(80.1,79.4)**
	685703	3598	1.93	3.00	(107.1,45.4)	(67.2,44.9)	**(93.2,78.2)**
	686911	87	1.53	1.78	(91.1,57.1)	**(82.6,87.5)**	(71.0,73.6)
80 GeV	677512	1432	2.60	2.50	(105.2,44.7)	(74.2,50.9)	**(91.7,78.2)**
	680911	1082	1.65	3.76	(107.9,43.1)	(79.9,52.4)	**(80.1,79.4)**
	679313	3217	1.58	0.73	(103.6,49.4)	**(90.8,79.4)**	(63.9,59.6)
	685703	3598	2.58	3.0	(107.1,45.4)	(67.2,44.9)	**(93.2,78.2)**
	686911	87	1.62	1.78	(91.1,57.1)	**(82.6,87.5)**	(71.0,73.6)
	687314	3316	1.66	0.85	(114.3,60.2)	(61.4,43.2)	**(91.1,80.1)**

Table 7: Candidates for the 80 and 85 GeV mass hypothesis that would pass a cut on $F_w(m_{\mathrm{H}}=80,85)>1.5$. The dijet masses are after the 4C fit and the combination which gives the best χ_{mass} is shown in bold face.

3.3 Neural network analysis I

The four-jet channel has the largest branching fraction for the Higgs mass range accessible at LEP. The signature of these events is four jets with two of them usually containing b quarks and the invariant mass of the other jet pair being consistent with the Z^0 mass. The dominant background comes from the W^+W^- hadronic decays and the $q\bar{q}$ events with hard gluon radiation. These two channels are highly suppressed for decays into b-jets. The ZZ background can not be distinguished if one of the Z boson decays into $b\bar{b}$.

A neural network method is developed for the Higgs search in four-jet final state. The network input variables are optimised for the independence of Higgs mass hypothesis. The network performance is studied for different training schemes.

3.3.1 Preselection

The event selection requires high multiplicity hadronic events with at least 10 tracks and 30 calorimetric clusters. The number of jets reconstructed is required to be at least four, using the JADE clustering algorithm with $Y_{cut}=0.02$. The Durham algorithm is then applied allowing the Y_{cut} to be varied with exactly four jets reconstructed. The constraint of four-momentum conservation is applied in the kinematic fit to improve the invariant mass resolution of jet pairs.

The selection cuts are imposed on the energy variables. The visible energy is required to be close to the centre-of-mass energy within 110 to 250 GeV and the missing energy to be less than 45 GeV; distributions of these two variables are shown in Fig. 9. The $q\bar{q}$ events are often accompanied with prompt leptons, which are rejected by requiring the most energetic lepton or photon to be smaller than 60 GeV.

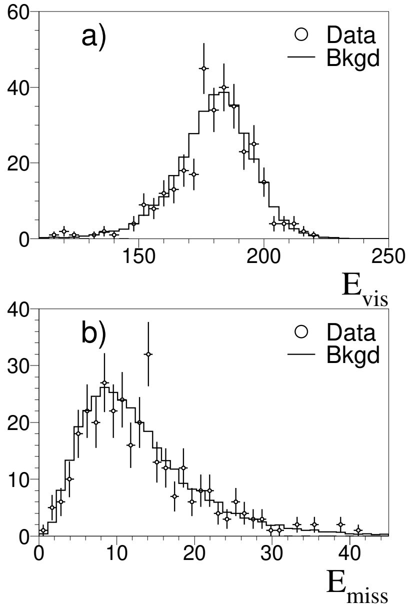

Figure 9: Distributions of the a) visible and b) missing energies for four-jet events.

The inputs for the neural network contain twelve variables in three categories. They are:

I. Multiplicities of good tracks, calorimetric clusters, and the sum of lepton and missing energies.

II. Topological variables of event thrust, spherocity, and centrality. The event centrality is the transverse energy divided by the total energy.

III. Kinematic variables including the minimum sum of di-jet masses, the di-jet mass (m_Z) of constraint fit for Z^0, χ^2 of 5C constraint fit, and a variable of the jet-pair for Higgs, $(\pi - \Omega)/(\pi - 2\text{atan}\frac{m_H}{p_H})$, where Ω is the measured opening angle of the two jets normalised to the value calculated using the Higgs mass and momentum of 5C constraint fit.

	$q\bar{q}$	W^+W^-	ZZ	HZ			
m_H [GeV]				75	80	85	90
MC events	330315	115586	29048	4540	4563	4509	4378
ϵ(E cuts)	0.0393	0.388	0.323	0.727	0.732	0.755	0.768
ϵ(NN cuts)	0.0121	0.276	0.217	0.637	0.675	0.688	0.686
σ [pb]	105.3	15.5	0.594	0.685	0.537	0.369	0.155
Events(55.3 pb^{-1})	70.5	237.8	7.1	14.4	11.9	8.3	3.5
Sum		315.4					

Table 8: Statistics for background channels and signal of four mass hypotheses. Signal samples contain only for $HZ \to b\bar{b}q\bar{q}$ (branching ratio is 0.594). The efficiencies are listed for those after the energy cuts (ϵ(E)), and neural network preselection cuts (ϵ(NN)). The number of expected events are calculated for a total integrated luminosity of 55.3 pb^{-1}.

IV. Two b-tagging variables formed by b-tags of jets (x_i in descending order); the non-B probability, $B_\eta = (1 - x_1)(1 - x_2)$, and the discriminant

$$B_{dis} = -\log_{10} P; \quad P = \left(\prod_{i=1}^{4} x_i\right) \sum_{j=0}^{3} \frac{[-\log(\prod_{i=1}^{4} x_i)]^j}{j!}. \tag{5}$$

The $q\bar{q}$ background can be discriminated by most of the network variables. The dominant W^+W^- background are distinguished largely by the kinematic and the b-tagging variables. The distributions of kinematic and b-tagging variables are shown in Fig. 10. The kinematic variables, illustrated in Fig. 11, are chosen to have the least dependence to the Higgs mass. The variable of the normalised opening angle of jet-pair for Higgs has retained the kinematic information with the mass dependence very much reduced.

The four-jet events are trimmed for the interval of input variables chosen to have good signal containment. The selection efficiency (ϵ(NN)) that enters the neural network are listed in Table 8. The Monte Carlo samples for signal and background are divided into two sets for training and test. The branching ratios applied are $BR(H \to b\bar{b}) = 0.85$ and $BR(Z^0 \to q\bar{q}) = 0.699$. The cross sections used for background and signal are listed in Table 8. The total integrated luminosity used is 55.3 pb^{-1}, the number of events selected is 321 and the background expected is 315.4 events. The standard model predictions for $HZ \to b\bar{b}q\bar{q}$ are also listed for four different mass hypotheses.

3.3.2 Network training and test

The neural network is trained for signal of mass hypothesis m_H=85 GeV with 12 input nodes and 24 hidden nodes. The background applied contains the dominant W^+W^- and $q\bar{q}$ of expected fractions. To enhance the recognition of $H \to b\bar{b}$, events of low b-tags are excluded in training by requiring the event tag $B_{tag} > 0.2$ and jet tags $(x_1 + x_2) > 0.5$.

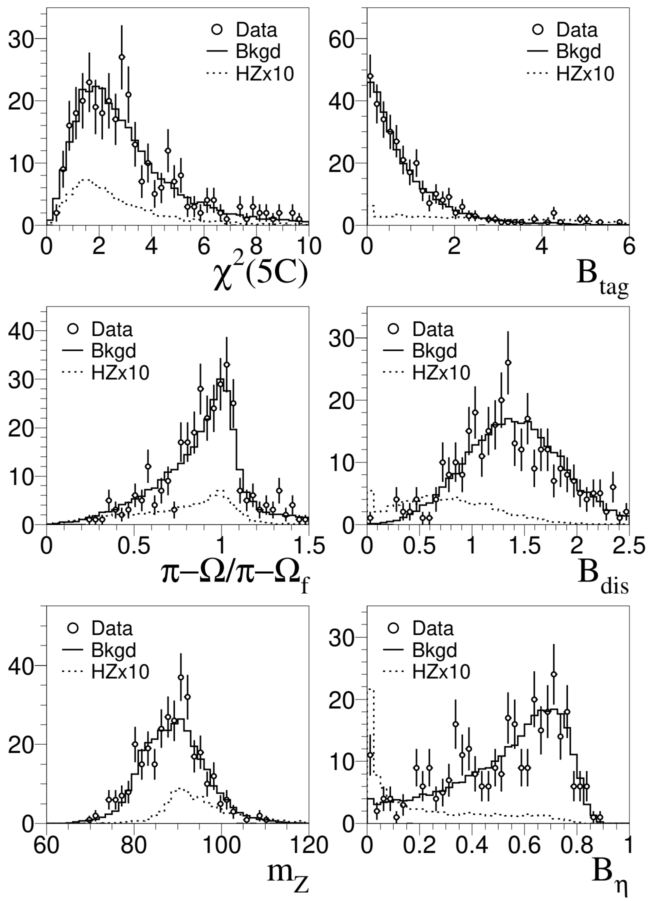

Figure 10: Distributions of kinematic and b-tagging variables for four-jet events of data (circles) expected background (solid lines) and signal of Higgs mass equals 85 GeV (dotted lines).

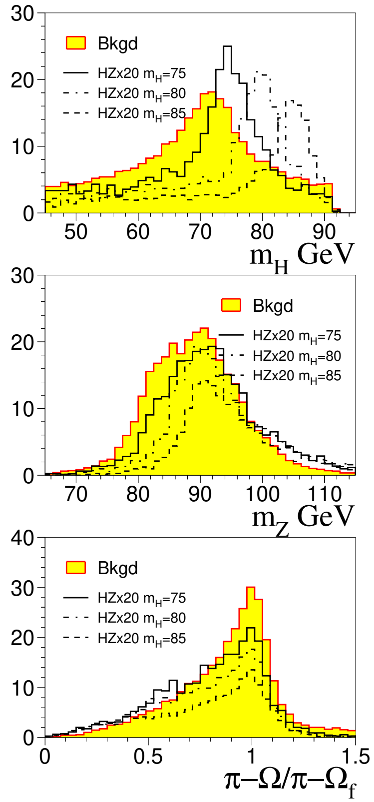

Figure 11: Distributions of variables relevant to the Higgs mass hypothesis; normalisation is applied to the total expected events (Table 1).

The distributions of network test outputs for data, background, and signal are shown in Fig. 12.a. The corresponding integrated distributions are shown in Fig. 12.b. The five most significant candidates are listed in Table 9.

The network variables are streamlined such that the systematic deviations can be un-

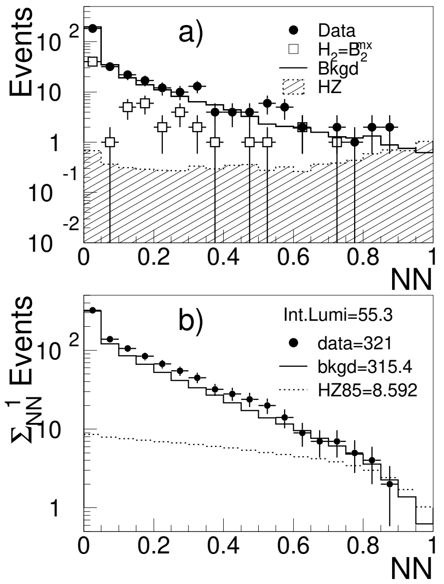

Figure 12: Distributions of the network outputs for data, background and signal are shown in a); the corresponding integrated distributions are shown in b).

derstood. The training cuts on b-tagging variables aim to increase the discrimination power for events rich in b-jets, such that the weights for kinematic variables are trained to be sensitive for them. If these cuts are taken out, the shapes of the network outputs alter, however, the selection efficiencies are still compatible.

Run	Event	E_{vis}	m_H(5C)	m_Z(4C)	B_{tag}	NN
677512	1432	209.5	78.6	91.7	3.80	0.89
685703	3598	186.5	79.9	93.2	4.34	0.88
678206	2740	173.2	83.3	98.0	2.30	0.85
677814	289	189.2	52.7	96.0	4.11	0.83
687808	2761	179.3	67.0	94.1	3.07	0.77

Table 9: The HZ candidates.

Data contains many low m_H evens distributed in low network output region. With a mass threshold of $m_H > 50$ GeV, the distribution is shown in Fig. 13, corresponding to 299 events observed for 297 background and 8.1 signal events expected. The mass dependence of the network training is examined by comparing the test outputs using the network trained at mass equals 90 GeV. Compatible results are observed, the test outputs are shown in Fig. 13.b. The ZZ background has many features common to $HZ \to b\bar{b}q\bar{q}$. The final states are identical in the case that one of the Z^0 decays into $b\bar{b}$. Confusion is introduced to the training if the background contains ZZ. The outputs are shown in the right column of Fig. 13.c. The spectra of signals tend to have a bump in the middle in particular for higher Higgs mass. The bump shifts closer to 1 if the ZZ fraction is reduced. The efficiencies obtained are compatible to those trained without ZZ.

3.3.3 Selection purity

The Higgs mass and the network output as two independent measurements are convoluted for the final analysis. The distributions of the Higgs mass (m_H) of 5C fit and the network outputs (NN) are shown in Fig. 14 for the mass hypotheses of 65 to 90 GeV. These distributions are parameterised as shown by the curves.

For a specified mass hypothesis, the purity of a given event is the probability is calculated using

$$P(m_H) = \frac{f_{sgnl}(m_H) \cdot g_{sgnl}(NN)}{\sum_{bkgd} f_i(m_H) \cdot g_i(NN) + f_{sgnl}(m_H) \cdot g_{sgnl}(NN)}, \tag{6}$$

where $f(m_H)$ and $g(NN)$ are the parameterisations for the distributions of m_H and network output. The purity distributions tested for four mass hypotheses are shown in Fig. 15. The significant candidate events are populated in m_H around 80 GeV, more data events are distributed in high purity region. The number of accumulated background events as a function of selection efficiency is illustrated in Fig. 16 for 85 GeV mass hypothesis.

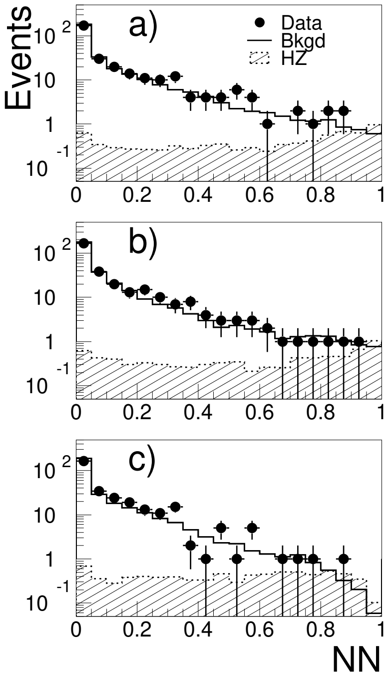

Figure 13: Distributions of network test outputs for data, background and 85 GeV signal events for a) training using 85 GeV signal sample, b) training using 90 GeV sample, c) training at 85 GeV with background containing 10% ZZ events.

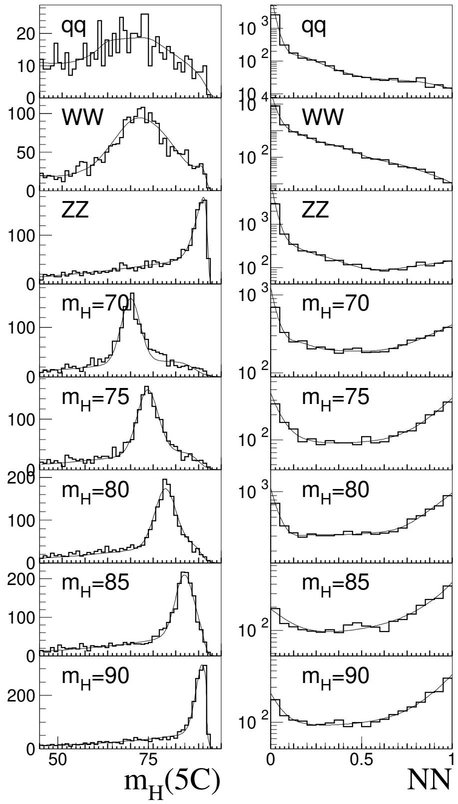

Figure 14: Distributions of Higgs mass of 5C fit and the network outputs for the mass hypotheses as labelled.

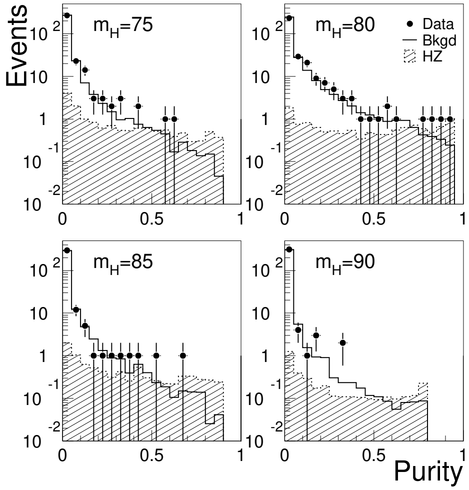

Figure 15: Distributions of the selection purity for the mass hypotheses as labelled.

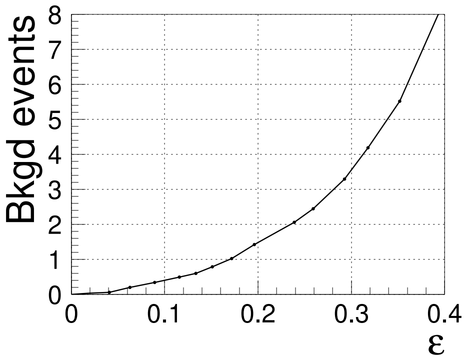

Figure 16: The number of accumulated background events versus selection efficiency for 85 GeV Higgs.

3.4 Neural Network Analysis II

A neural network based analysis has been developed to search for SM Higgs in the four-jets channel. In the following sections a detailed description of the strategy, the preselection, the neural network and the reconstruction of the Higgs mass is given.

3.4.1 Strategy

The analysis proceeds in three different steps:

- Selection based on the optimised procedure described in the *published weight analysis* section. It must be underlined that the btagging variable is included in the optimisation.
- Neural network which aims at reducing mass dependence of the performances, at least in the region close to the expected exclusion limit.
- Combination of Neural Network Output with 5C reconstructed Higgs Mass to build a final variable, in order to enhance the performances in the low background region.

The following subsections describe the three steps and discuss the results obtained.

3.4.2 Selection

Table 10 shows the cuts used in the optimised selection, the number of events expected from MC and found in data, as well as the efficiency for the Higgs signal ($H \to b\bar{b}$). The b-tagging variable D_{TAG} is obtained from the combination of the btag 3D neural network for the 4 jets. Figure 17 shows the selection efficiency as a function of the Higgs mass.

Figure 18 shows the 5C reconstructed Higgs mass for the selected events, and for the expectations from MC. From the distribution for 85 GeV Higgs a resolution of 2.9 GeV can be estimated for the central part.

3.4.3 Neural Network

The following 17 variables are used as input to a neural network:

1) Y_{34} from Durham

2) $Thrust$

3) $log(min(\chi^2_{HZ}))$ based on sum and difference of dijet masses

4) D_{TAG}

5) $NN_{btag}^{higgsjet1}$

6) $NN_{btag}^{higgsjet2}$

7) $log(\chi^2_{HZ/4C})$

8) $max(\cos\Delta\theta)$

9) N_{cl}

10) $log(\chi^2_{WW})$

11) $\frac{E_{jet}^{min}}{\sqrt{s}}$

12) $\frac{\Delta E_{ij}}{\sqrt{s}}$

13) Sphericity

14) Spherocity

15) $\frac{M_{ij}^{min}}{\sqrt{s}}$

16) $\frac{M_{ij}^{max}}{\sqrt{s}}$

17) Y_{34} from Jade

Figure 19 shows the distribution of 4 input variables (nr. 2,3,13,16) for data and the different MC contribution.

The network has 25 hidden nodes, and the training procedure is done with two independent MC sample, split on the basis of even/odd event number. In the learning phase, only events from qq and WW are used, with proportion approximately equal to the expected one. The network has three outputs (qq/WW/Higgs) and only the Higgs node is used in the analysis. The training is done with a Higgs signal of 85 GeV, and the same network is then used for other masses. Due to the limited MC statistics (especially qq), the btag preselection cut applied in the learning phase (0.5) is looser than the one later used in the analysis. In this way about 4000 events are used in the learning phase, of which 1300 are signal events. The network optimisation is done at about 30% efficiency for the signal.

The distribution of the NNET output are shown in figure 20 for data, background and 85 GeV Higgs. Figure 21 shows the background expectation as a function of the efficiency for a 80 and 85 GeV Higgs. Figure 22 shows the integrated distribution of the NNET output for the same two masses, together with the efficiency multiplied by 10.

3.4.4 Final Variable from NNET and Mass

In order to enhance the performances at low level of background, the resolution on the 5C reconstructed Higgs mass can be exploited. From the signal-to-background distribution of the NNET output and the 5C Higgs mass, a single variable is built (W=log($(S/B)_{mass} * (S/B)_{NNET}$) The distribution of this final variable is shown in figure 23 for data, background and 85 GeV Higgs. It must be underlined that there is an implicit lower cut on the 5C reconstructed Higgs mass when the final variable is built.

Figures 24 shows the integrated distribution for the final variable, while figure 25 shows the background expectations and number of data events as a function of the efficiency, for 85 GeV Higgs.

3.4.5 Most significant candidates

Table 11 shows the event characteristics for the 18 selected events. The NNET output refers to the 80 GeV mass hypothesis. Table 12 gives the same information for the 85 GeV mass hypothesis.

Variable	cut	DATA	MC	HZ (85 GeV)
N_{cl}	40			
$\vert\frac{E_{vis}-\sqrt{s}}{\sqrt{s}}\vert$	0.38			
N_{gtk}	20			
$\frac{M_{vis}}{\sqrt{s}}$	0.4			
$\frac{\sqrt{s'}}{\sqrt{s}}$	0.601			
Y_{34}	0.055	569	529	86.4%
$\max(\frac{E_{jet}^{BGO}}{E_{jet}})$	0.969	516	477	85.6%
$\cos\theta_{jet}$	0.99			
$\frac{E_{jet}^{min}}{\sqrt{s}}$	0.0234	503	466	83.0%
$\frac{\Delta E_{ij}}{\sqrt{s}}$	0.857			
$\cos\Delta\theta$	-0.99387	492	457	81.8%
$\frac{M_{ij}^{min}}{\sqrt{s}}$	0.113			
$\frac{M_{ij}^{max}}{\sqrt{s}}$	0.659	395	356 (72.5 qq / 274.5 WW / 8.7 ZZ)	75.9%
D_{TAG}	1.6	18	20.2 (9.0 qq/9.4 WW / 1.8 ZZ)	43.9%

Table 10: Selection cuts

Run	Event	5C Higgs Mass	NN out (80 GeV)	Evis
67460.4	513.	65.154	0.3513	172.815
67751.2	1432.	78.6324	0.9935	209.523
67760.2	5167.	72.5971	0.4009	202.643
67940.3	4685.	62.3154	0.4784	188.314
68090.2	5368.	70.2755	0.3445	153.815
68091.1	1082.	70.5779	0.8341	180.227
68160.8	1736.	54.5381	0.7474	176.865
68170.8	3594.	59.4344	0.1372	172.661
68441.2	4030.	84.9285	0.9851	115.47
68560.1	1657.	72.8813	0.8071	151.023
68570.3	3598.	79.8507	0.9927	186.477
68691.1	87.	57.0281	0.9607	188.358
68750.8	1787.	69.9329	0.4701	199.94
68760.6	3681.	59.6488	0.3335	163.206
68780.8	2761.	66.9586	0.4237	179.295
68840.3	5081.	43.3649	0.7832	196.206
68870.6	5347.	86.6226	0.5436	181.984
68990.4	1706.	66.0329	0.3909	154.697

Table 11: Event characteristics for the 18 selected events. The NNET output is for 80 GeV hypothesis.

Run	Event	NN out (85 GeV)	5C Higgs mass	Evis
6746.04	513.	0.2967	65.154	172.815
6775.12	1432.	0.9242	78.6324	209.523
6776.02	5167.	0.4905	72.5971	202.643
6794.03	4685.	0.4184	62.3154	188.314
6809.02	5368.	0.2516	70.2755	153.815
6809.11	1082.	0.7728	70.5779	180.227
6817.08	3594.	0.1163	59.4344	172.661
6844.12	4030.	0.9982	84.9285	115.47
6856.01	1657.	0.5486	72.8813	151.023
6857.03	3598.	0.9639	79.8507	186.477
6875.08	1787.	0.3942	69.9329	199.94
6876.06	3681.	0.2785	59.6488	163.206
6878.08	2761.	0.4135	66.9586	179.295
6887.06	5347.	0.5069	86.6226	181.984
6899.04	1706.	0.2262	66.0329	154.697

Table 12: Event characteristics for the events which enters the distribution of the final variable. The test hypothesis is 85 GeV.

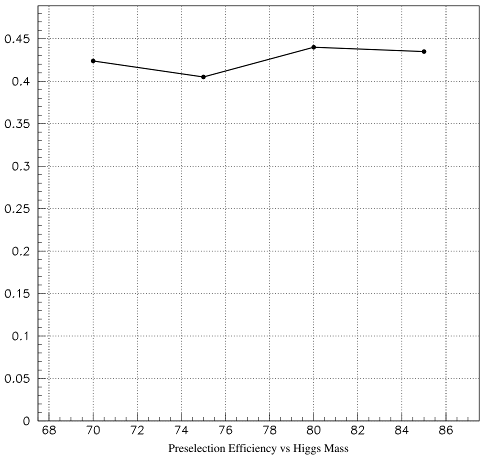

Figure 17: Selection efficiency as a function of the Higgs mass.

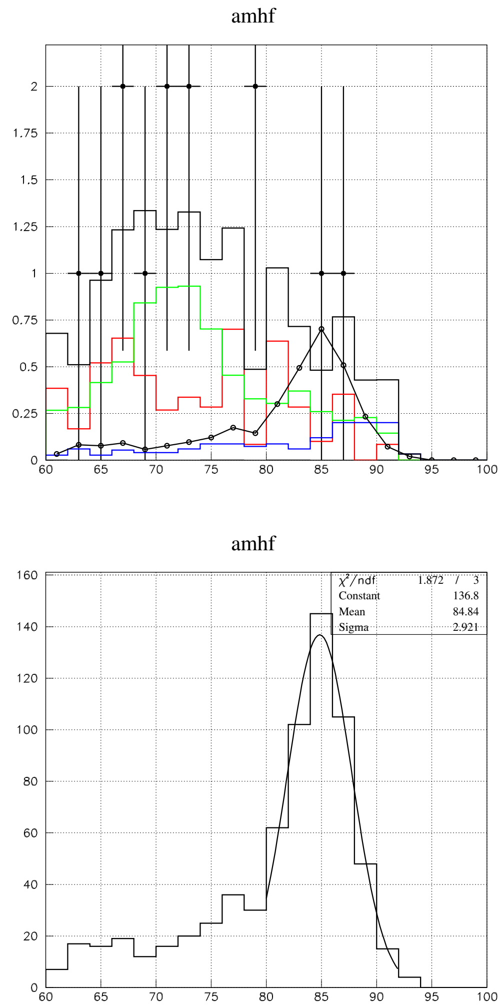

Figure 18: Distribution of the 5C reconstructed Higgs mass for data, background and 85 GeV Higgs. The different contribution to the background are shown (qq red, WW green, ZZ blue).

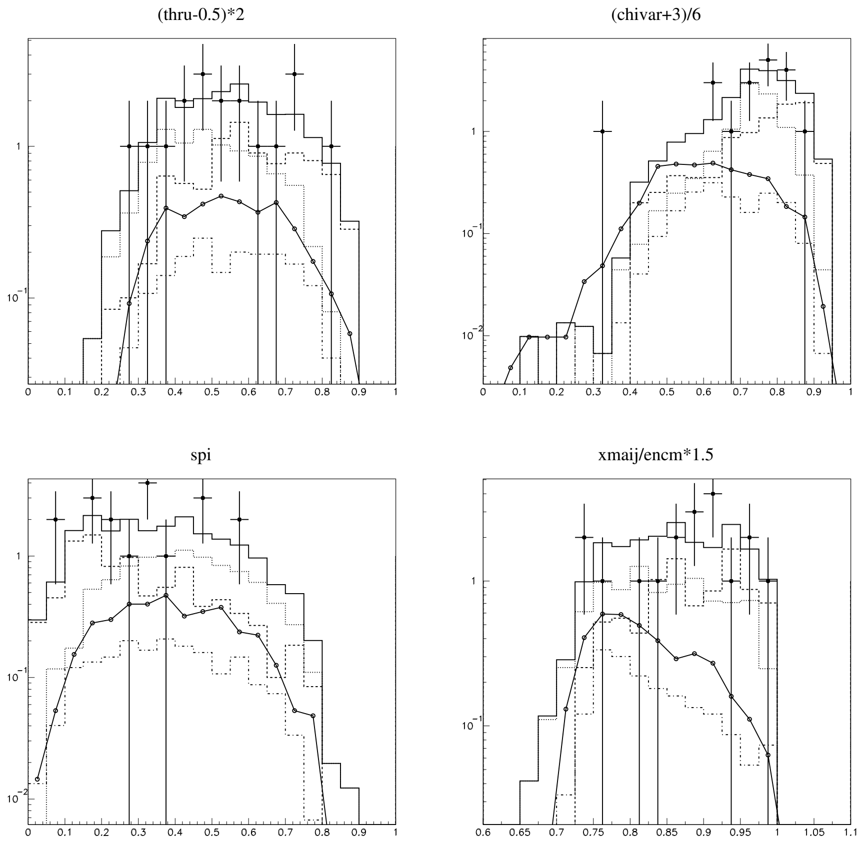

Figure 19: Distribution of 4 NN input variables (nr. 2,3,13,16) for data (points), qq (dashed line), WW (dotted line), ZZ (dashed-dotted line) and all MC (solid line)

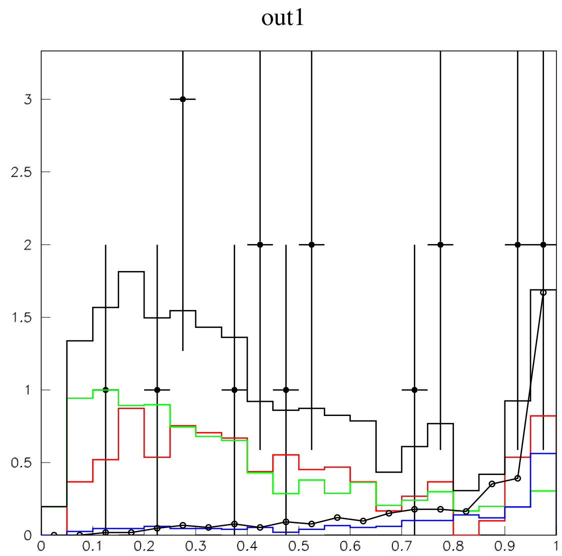

Figure 20: Distribution of the NNET output for data, background and 85 GeV Higgs. The different contribution to the background are shown (qq red, WW green, ZZ blue).

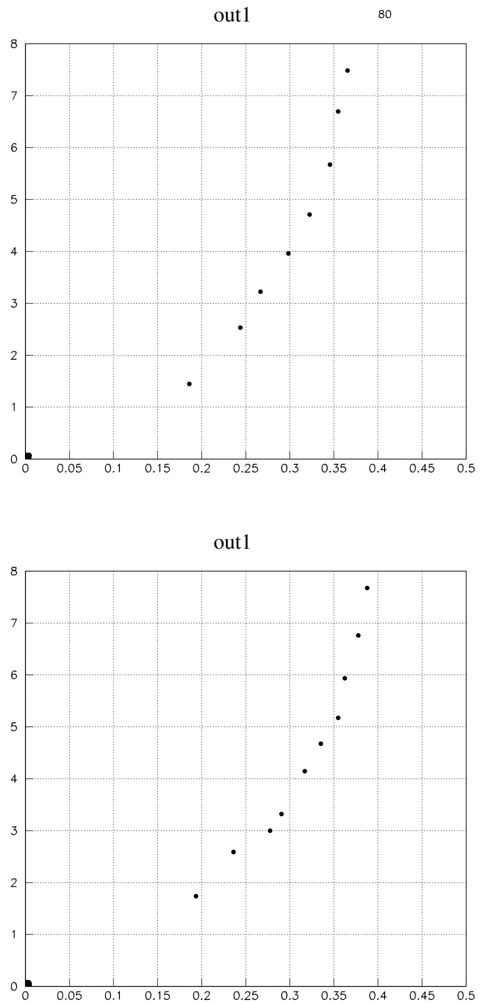

Figure 21: Background expectations as a function of the efficiency for 80 (top) and 85 (bottom) GeV Higgs from the NNET output

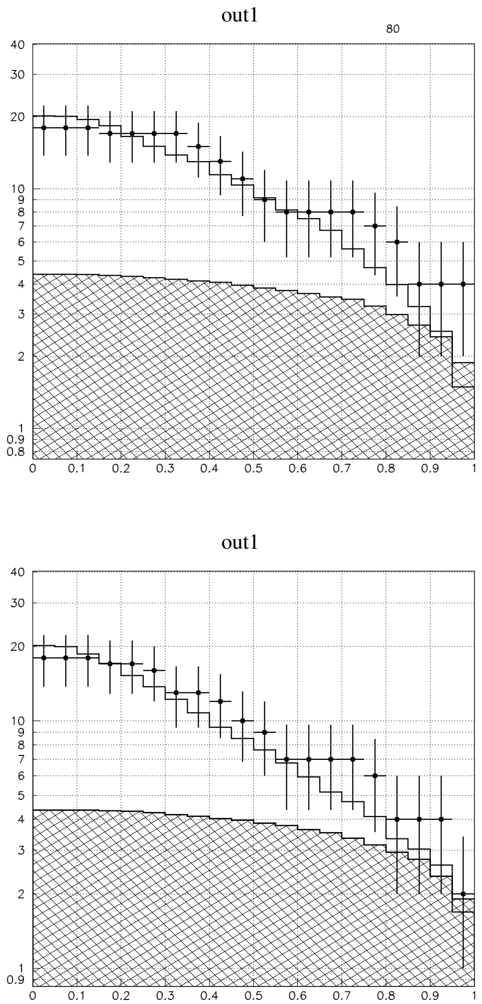

Figure 22: Integrated distribution of the NNET output for data and MC, and efficiency (x 10) for 80 (top) and 85 (bottom) GeV Higgs

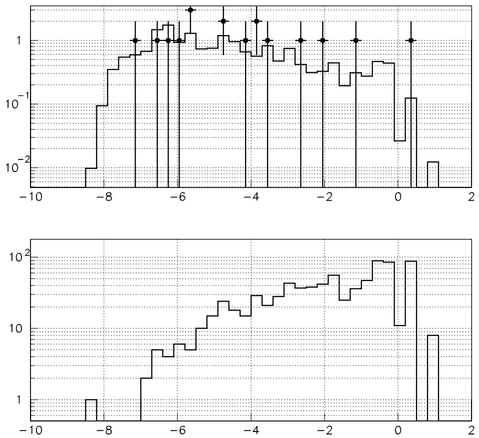

Figure 23: Distribution of the final variable NNET*MASS for data and background (top), and for Higgs signal of 85 GeV (bottom).

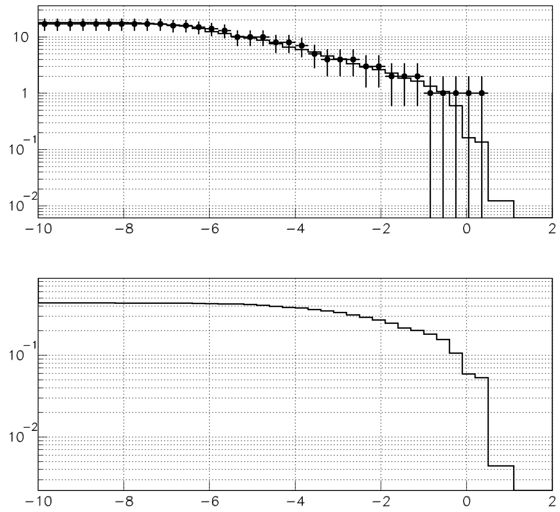

Figure 24: Integrated distribution of the final variable NNET*MASS for data and MC (top), and efficiency (x 10) for 85 GeV Higgs (bottom).

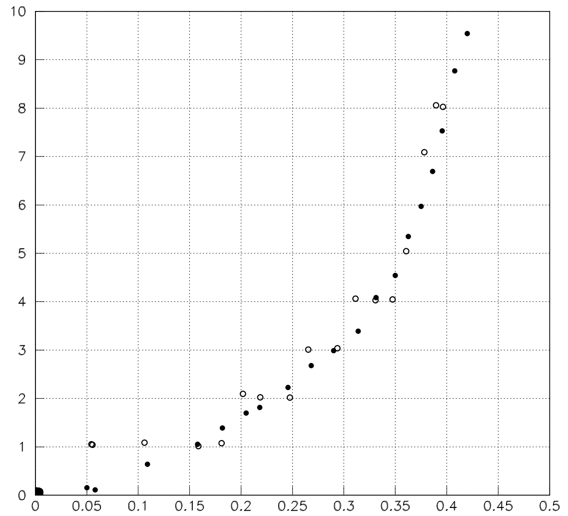

Figure 25: Background expectations (black dots) and data events (open dots) as a function of the efficiency for 85 GeV Higgs from the final variable NNET*MASS.

4 The $HZ \rightarrow q\bar{q}\nu\bar{\nu}$ channel

5 Weight analysis for $\mathrm{H}\nu\bar{\nu}$

The weight analysis as described in detail in [1] and published in [2] has been repeated on the data collected at 182.7 GeV center of mass energy. The total integrated luminosity used in the analysis is 55.3 pb^{-1}.

A first preselection has been applied to reduce the data sample:

- $0.2 < E_{\mathrm{vis}}/E^{CM} < 0.8$
- $E_{BGO} > 2$ GeV
- $N_{\mathrm{cl}} > 10$
- $N_{\mathrm{natk}} > 4$
- $N_{\mathrm{gtk}} > 1$
- $P_t > 5$ GeV
- $NAMU + NSCT > 0$
- $\sin(\theta_{miss}) > 0.2$
- $E_{EGAP}/E_{\mathrm{vis}} < 0.3$
- $|P_L|/E_{\mathrm{vis}} < 0.8$

Table 13 reports the loose cuts used for the selection and the tight cuts used in the construction of the ξ variable.

The loose cuts are obtained optimising the selection for 5.53 pb^{-1}, at this point the btag cut is fixed and the optimisation for the tight cuts is carried out assuming a luminosity of 553 pb^{-1}. Both optimisations are performed using as signal the HZ process with $\mathrm{Z} \rightarrow \nu\bar{\nu}$ and $\mathrm{H}^0 \rightarrow \mathrm{b}\bar{\mathrm{b}}$ with $M_H = 81, 83, 85, 87, 89$ and 91 GeVtogether.

After these cuts 5 events survived with 6.8 events expected from the background. The efficiency ($\mathrm{e}^+\mathrm{e}^- \rightarrow \mathrm{ZH}^0 \rightarrow \nu\bar{\nu}\mathrm{b}\bar{\mathrm{b}}$) is 55.3 for an 80 GeV Higgs Boson, 59.3 for an 85 GeV Higgs Boson and 48.1 for a 90 GeV Higgs Boson.

Figure 26 shows the distributions of the ξ, B_{tag} and rescaled mass variables after the selection on data, background and 85 GeV signal. Figure 27 shows the background expectations versus the efficiency for an 85 GeV Higgs boson.

Table 13: The two sets of cuts used in the construction of the ξ variable for the Hnunu channel.

cut		loose selection	tight selection
E_{vis} (GeV)	$>$	46.51	46.51
E_{vis} (GeV)	$<$	105.9	105.9
$\vert P_L\vert/E_{\text{vis}}$	$<$	0.5	0.5
$\vert P_T\vert/E_{\text{vis}}$	$>$	0.05	0.05
N_{cl}	$>$	16	16
N_{gtk}	$>$	3	3
P_T (GeV)	$>$	7.161	7.161
$\sin(\theta_{miss})$	$>$	0.3349	0.4524
E^{ISO}_{LEPT} (GeV)	$<$	5.434	3.307
$\min(\sin\theta_{J1}, \sin\theta_{J2}$	$>$	0.1333	0.1885
M_{miss} (GeV)	$>$	71.86	82.29
M_{miss} (GeV)	$<$	147.2	147.2
$\pi - ACOL$	$<$	0.8630	0.8282
$BTAG3D$	$>$	1.147	1.147
$ETTJ$ (GeV)	$>$	1.950	3.514
$ECM60$ (GeV)	$<$	60.59	39.16
$ECMF40$ (GeV)	$<$	34.08	17.54
$EM25$ (GeV)	$<$	20.71	20.71
E_{LUM} (GeV)	$<$	8.272	4.136
E_{ALR} (GeV)	$<$	8.321	8.321

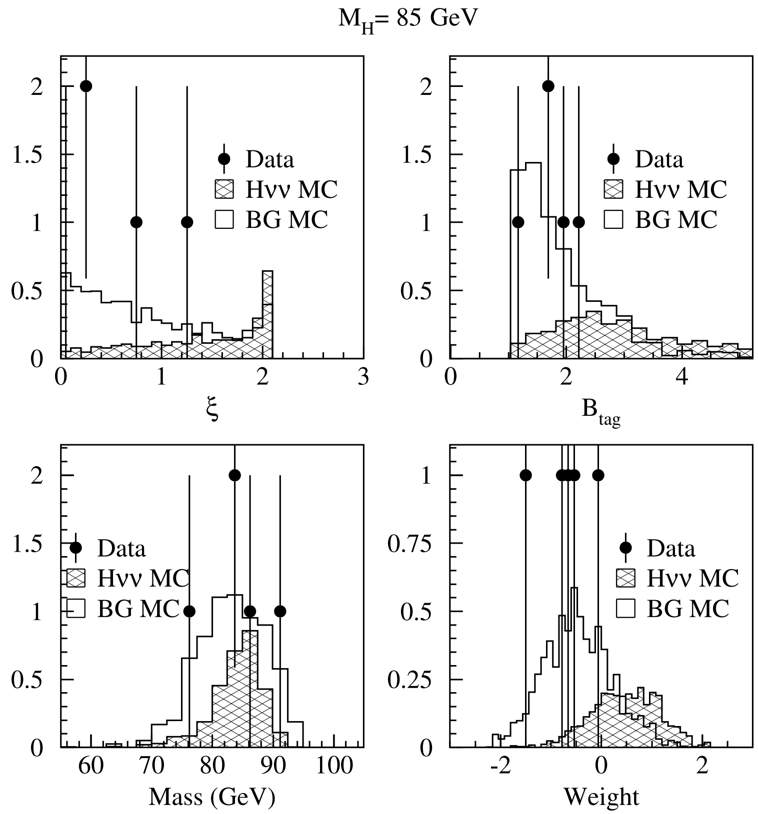

Figure 26: The variables used as an input to calculate event weights for the H$\nu\bar{\nu}$ analysis: kinematic variable ξ_{kin}, B_{tag} variable, the invariant mass of the two jets, after forcing the recoil mass to be equal to $m_Z M_{\text{vis}}$; and the final event weight spectrum for 183 GeV data sample. The superimposed hatched histograms correspond to the 85 GeV Higgs boson signal with arbitrary normalization.

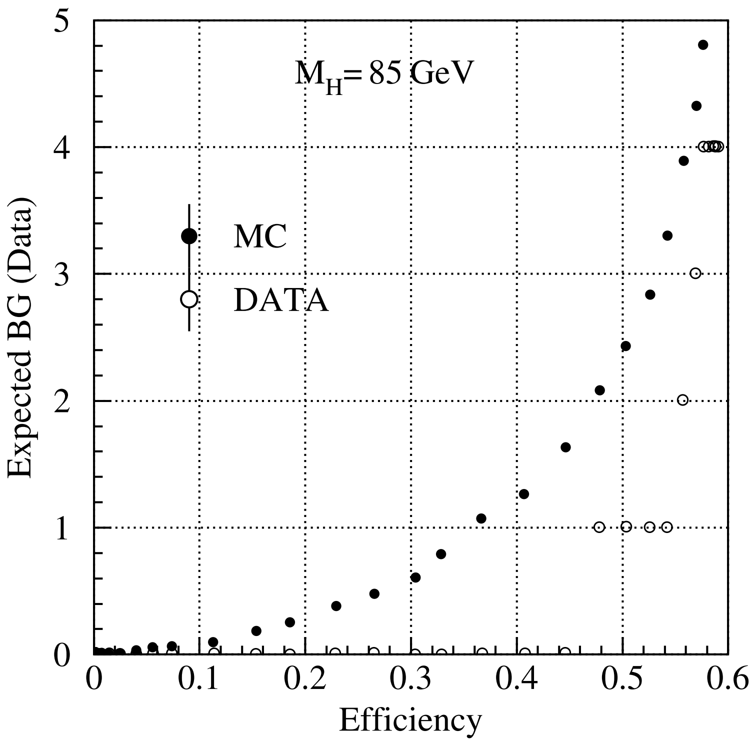

Figure 27: Plot of background versus efficiency for 85 GeV Higgs boson signal, the empty points indicate the data candidates.

5.1 Neural Network analysis

The preselection of candidates for the process $e^+e^- \rightarrow H\nu\bar{\nu}$, $H \rightarrow b\bar{b}$ is based on the following requirements: two acoplanar hadronic jets, large missing transverse energy and secondary vertices due to B-hadron decays.

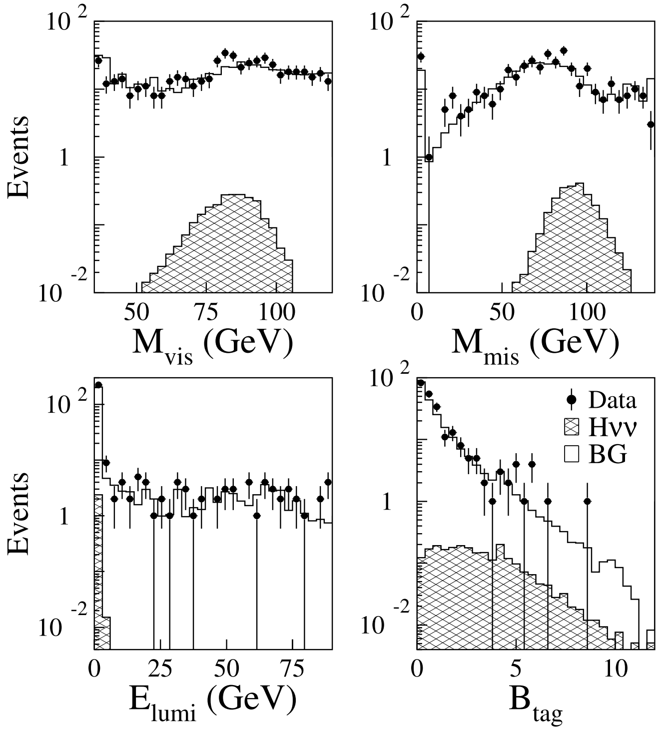

Figure 28: Data, expected background and 87 GeV signal for the most important variables used in the $H\nu\bar{\nu}$ preselection. The cuts are applied as discussed in the text.

High multiplicity hadronic events with more than three charged tracks and at least fifteen calorimetric energy clusters are selected. All energy clusters in the event are combined to form two hadronic jets using the DURHAM algorithm. The invariant mass of these jets, M_{VIS}, is required to exceed 40 GeV (Fig 28a). These cuts reduce contributions from the pure leptonic final states $e^+e^- \rightarrow e^+e^-(\gamma)$, $\mu^+\mu^-(\gamma)$, $\tau^+\tau^-(\gamma)$ and two-photon interactions

$e^+e^- \to e^+e^-q\bar{q}$ while keeping a significant fraction of hadronic events from $e^+e^- \to Z(\gamma)$ and $e^+e^- \to W^+W^-$. It is reduced by requiring $M_{\rm VIS} < 115$ GeV (see Figure 28a). The recoil mass is required to be in the range $50 < M_{\rm MIS} < 130$ GeV (see Figure 28b).

To reject further events from the two fermion production process $e^+e^- \to q\bar{q}(\gamma)$ the transverse missing energy, $E_\perp$, is required to exceed 5 GeV. The missing momentum vector must be at least 0.32 rad away from the beam axis. The longitudinal momentum must be smaller than 70% of $E_{\rm vis}$. The opening angle between the two jets is required to be greater than 69° . The energy in the forward luminosity calorimeters is required to be smaller than 15 GeV (Fig 28c). In addition the B-tagging variable, $B_{\rm tag}$, is required to be greater than 0.6 (see Figure 28d).

preselection cut	N_{data}	N_{bg}	ε_{87}
hadronic preselection $E_{\rm mis} > 5$ GeV $35 < M_{\rm vis} < 120$	519	509.6	88.2%
$E_{/}/E_{\rm vis} < 0.7$ $40 < M_{\rm vis} < 115$ $E_\perp > 5$ GeV	399	363.4	86.4%
$\alpha_{\rm j-j} > 1.2$ $50 < M_{\rm mis} < 130$	296	266.1	85.6%
$E_{\rm lumi} < 15$ GeV	233	213.4	85.3%
$B_{\rm tag} > 0.6$	121	103.2	78.2%
$\alpha^* > 0.1$	61	54.0	72.9%
cuts on NN inputs	56	50.4	72.3%

Table 14: Number of events expected from SM physics processes compared to the observed number of events in the data, after each major selection step. The MC expectations are normalised to the luminosity and the SM cross sections. The signal efficiencies for a Higgs of 87 GeV as function of the cuts, are also presented.

The number of events satisfying the selection criteria are given in Table 14 for each major selection step. Fifty six candidate events are selected in the data sample consistent with the background expectation of 50.4. The signal efficiency as a function of Higgs Boson mass is presented in Table 15.

$M_{\rm H}$	65 GeV	70 GeV	75 GeV	80 GeV	85 GeV	90 GeV	Bkgd	Data
NN > 0.0	76.0%	75.4%	76.4%	76.7%	74.1%	67.0%	50.4	56
NN > 0.5	35.7%	39.2%	41.6%	44.6%	46.9%	42.5%	2.4	2

Table 15: The signal efficiency, expected background and the number of observed events as a function of Higgs mass.

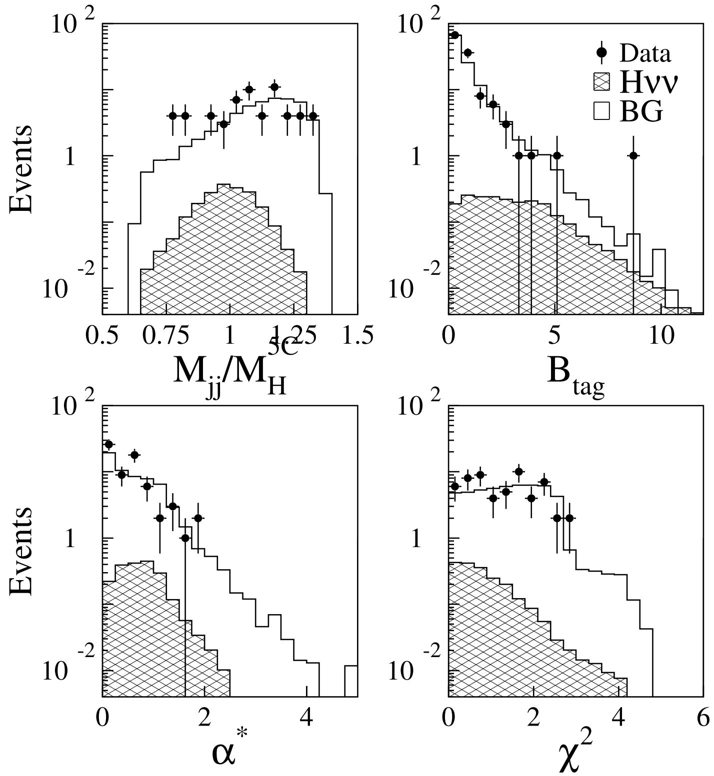

Figure 29: Data, expected background and 87 GeV signal for the most important variables used as inputs for $H\nu\bar{\nu}$ neural network: a) normalised hadronic mass; b) $B_{\rm tag}$ variable, c) normalised acoplanarity angle; d) χ^2 of the kinematic fit. For each figure all the cuts are applied except the cut on the variable presented in the figure.

Neural network is then used to construct a discriminant variable that further separates the signal from the background. The effort is made to make neural net inputs independent on the reconstructed $M_{\rm H}^{5C}$ mass. Eight variables are used as an input to the net, four of them are presented in Figure 29 before applying the cuts on that variable. In general they are similar to those used for last year analysis [1, 2] but are divided by a characteristic quantity that is derived from the kinematic fit. The neural network is trained over one-

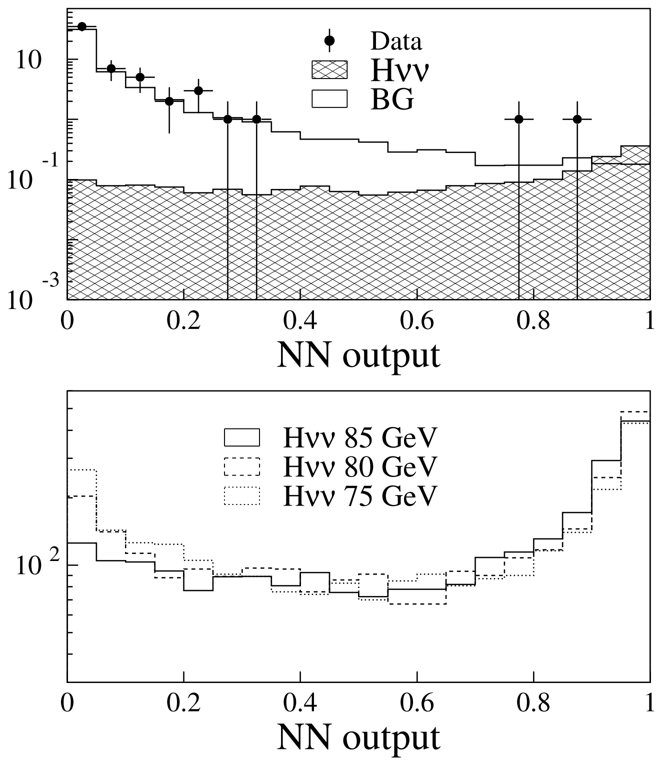

Figure 30: Data, expected background and 87 GeV signal for the $H\nu\bar{\nu}$ neural network output.

third the Monte Carlo sample. In the training procedure events $ZZ \to b\bar{b}\nu\bar{\nu}$ were not used as they are indistinguishable from the signal events. performance is then evaluated using the remaining-two thirds of the Monte Carlo sample. The spectrum of the neural net output is presented in Figure 30.

The kinematic fit that uses energy and momentum conservation and constrains the recoiling mass to M_Z is applied to the selected events in order to improve the mass resolution for the signal events. The two jet energies are varied in the fit according to their estimated resolutions, whereas the jet directions are left unchanged. The invariant mass resolution

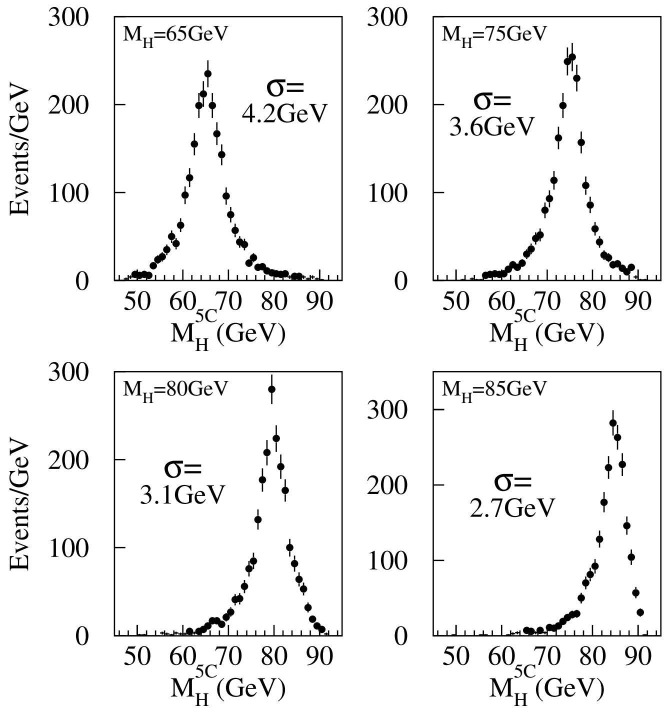

Figure 31: The spectrum of the reconstructed invariant mass M_H^{5C} for the signal events of different masses for the $H\nu\bar{\nu}$ analysis.

after this fit is about 2.8 GeV for the central part of the distribution in the mass range from 80 to 90 GeV (see Figure 31). This mass (M_H^{5C}) and the mass-independent neural net output are used to evaluate consistency of an event with the given Higgs mass hypothesis. To do this the purity variable, P_{M_H}, is defined as follows:

$$P_{M_H} = \frac{N_s \cdot f_s(M_H^{rec}, M_H) \cdot g_s(NN_{out})}{N_s \cdot f_s(M_H^{rec}, M_H) \cdot g_s(NN_{out}) + N_b \cdot f_b(M_H^{rec}, M_H) \cdot g_b(NN_{out})} \tag{7}$$

where N_s and N_b are the number of expected signal and background events, respectively,

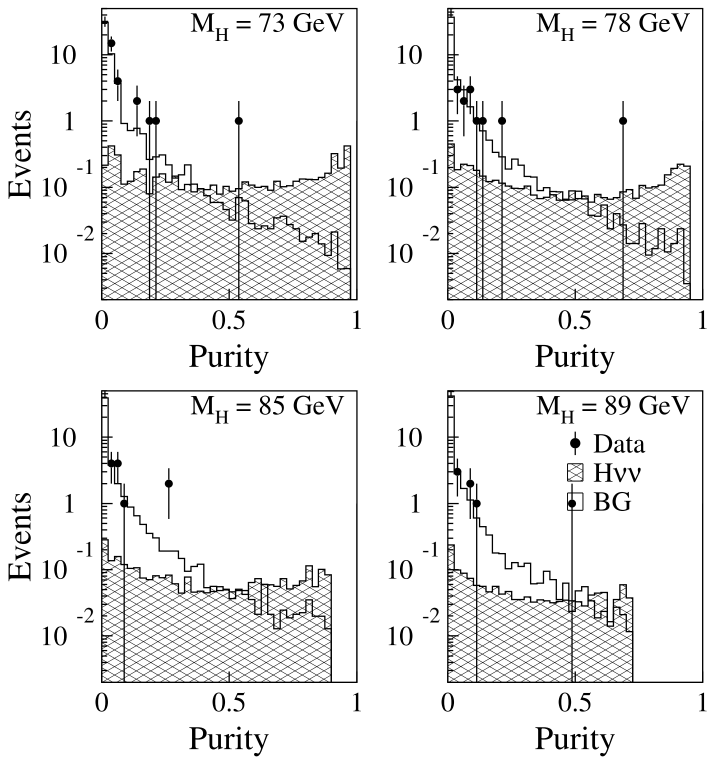

Figure 32: Data, expected background and signal for the purity variable for several Higgs mass hypotheses in the H$\nu\bar{\nu}$ analysis.

after preselection, and f_s (g_s) and f_b (g_b) are the one-variable probability density functions of $M_\mathrm{H}^\mathrm{rec}$ (NN_out) for the signal and background, respectively. The spectra of this variable for the several Higgs mass hypothesis are presented in Figure 32.

The final picture that represents the quality of this analysis is the Higgs signal efficiency versus the number of background events for 87 GeV Higgs mass hypothesis (Figure 33).

The systematics related to the use of the neural network was studied by changing the energy calibration by $\pm 2\%$ what corresponds to a maximal possible uncertainty in the calibration procedure. The 2% error on the signal efficiency is assigned due to the

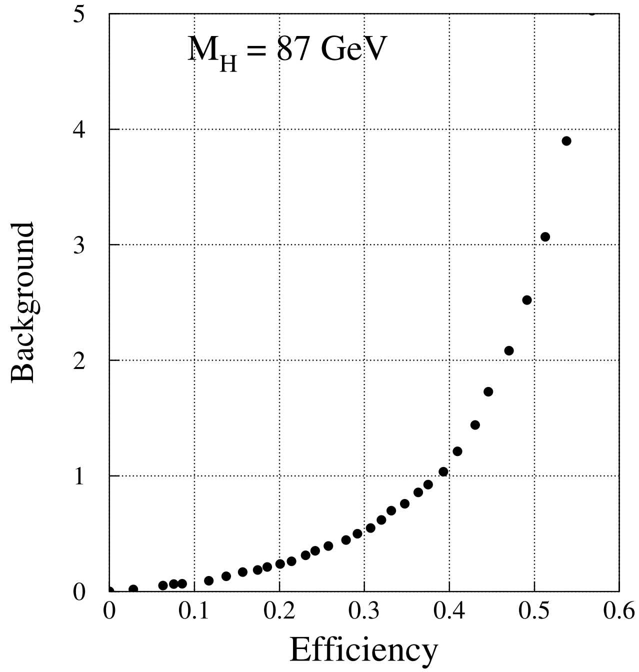

Figure 33: The Higgs signal efficiency versus the number of background events for 87 GeV Higgs mass hypothesis for the H$\nu\bar{\nu}$ analysis.

uncertainty in the $\mathrm{B_{tag}}$ spectrum. The influence on the final limit of this variations is found to be negligible compared to the pure statistical uncertainty on the number of the background events in the signal-sensitive regions (i.e. $NN_\mathrm{out} \simeq 1$) which is likely to be the dominant systematics. Other Higgs boson decays: $\mathrm{H} \to \mathrm{c\bar{c}}$, $\mathrm{H} \to \mathrm{gg}$ are also accounted for in the limit calculation as well as the contribution to the Higgs production from WW fusion.

6 The $HZ \to q\bar{q}\ell^+\ell^-(\ell = e, \mu, \tau)$ and $HZ \to \tau^+\tau^-q\bar{q}$ channels

6.1 Sequential cut analysis for $HZ \to q\bar{q}e^+e^-$ and $HZ \to q\bar{q}\mu^+\mu^-$ channels

We have used a sequential analysis to perform the search of HZ events at the centre of mass energy of 183 GeV. The integrated luminosity available after elimination of bad runs is 55 pb^{-1}.

The signature of the HZ process with $Z \longrightarrow ll$ decay is the presence of two energetic and well separated leptons coming from the Z boson and isolated from the Higgs decay products. The hadronic decays of the Higgs boson give high multiplicity events, and in the visible Higgs and Z decay modes, we expect a visible energy of about the centre of mass energy $\sqrt{s}$.

To reject all the low multiplicity events like Bhabha, we ask for at least 6 tracks and 16 Asrc's. A ratio Visible Energy/$\sqrt{s}$ > 70% is also required to reduce 2 photons events. Finally, to end the preselection, we ask for two patterns identified as lepton or photon, including MIP's. At least one of these patterns must have a minimum energy of 5 GeV.

With these cuts we select 1215 events for 1237 expected, in which we have 923 $Z/\gamma \longrightarrow q\bar{q}$, 284 WW, 11 ZZ, and 19 Zee. The efficiency on Higgs signal is about 90% for Hee channel and 75% for H$\mu\mu$ channel. Figure 34 shows the distributions of the number of ASRC's and the Visible Energy after the preselection.

Then we define a first step in the selection, to separate the Hee and H$\mu\mu$ analyses, this step is the identification.

For the Hee channel, we ask for 2 electrons or photons, but with at least one electron, in order to reduce the $q\bar{q}$ contribution.

For the H$\mu\mu$ channel, two muons are required.

Some final cuts complete the selection :

- $\sqrt{s'}$ > 120 GeV : reduces $q\bar{q}$ process,
- $M_{min} < M_{ll} < M_{max}$, to reduce all backgrounds,
- for Hee channel only, in order to reduce the $q\bar{q}$ background in which energetic photons can be found, we apply a tighter cut on the two leptons invariant mass when one of them doesn't match with a track. It enables to keep good events with TEC problem and to reject photons. The tighter range is $[85, 97]$ GeV/c^2.
- $min(Pt_1, Pt_2) > Pt_{min}$, to reduce all but ZZ processes. Pt_i is the transverse momentum of the lepton i with respect to the axis of the nearest jet reconstructed by masking the two leptons.

- for Hee channel only, in order to reduce Zee process, in which one electron can reach high energy, we ask for a maximum of 75 GeV : $E_1 < 75$ GeV.
- b-tag cut : we ask for a b-tag discriminant greater than 0.5. This cut is useful to reduce all backgrounds, and especially the irreducible ZZ process.

The dilepton mass and transverse momentum thresholds are given in the following table :

	Hee	H$\mu\mu$
M_{min}	75 GeV	60 GeV
M_{max}	105 GeV	120 GeV
Pt_{min}	9 GeV/c	3 GeV/c

The distributions of the selection variables are shown in the figures 35 and 36, after the identification step, an compared to the data.

The efficiencies for all the cuts are given in table 16 and table 17 for Hee and H$\mu\mu$, and the expected backgrounds are shown in tables 18 and 19.

The efficiencies on several Higgs mass simulations are displayed on the figure 37, and show the sequential analysis is quite mass independent. The lower efficiencies in the low mass range are due to the energy cut on the first electron. The lower efficiency on the last mass simulation point (93 GeV/c^2) is due to the transverse momentum cut.

We have finally tightened the btag and dilepton mass cuts in order to show the behaviour of the sequential analysis : the expected background versus the Higgs efficiency in shown on figure 38.

In conclusion, with cuts values given previously, we expect 0.68 background events with the Hee selection and 0.37 with the H$\mu\mu$ one, and we observe no event. The efficiency on 90 GeV/c^2 Higgs signal is about 60% for Hee and 40% for H$\mu\mu$.

selection step	qq	WW	ZZ	Zee	H 70 GeV	H 85	H 90
identification	3.1	9.5	12.6	6.7	85.6	84.8	82.0
$\sqrt{s'}$	1.6	9.1	12.1	5.3	77.8	81.0	80.9
M_{ll}A	0.021	0.073	2.1	0.39	66.8	71.0	68.7
M_{ll}B	0.010	0.059	2.0	0.34	65.9	69.2	67.4
$min(Pt_i)$	0.0033	0.013	1.9	0.24	63.5	67.7	65.7
E_1	0.0033	0.013	1.8	0.15	63.2	67.7	65.7
b tag	0.0018	0.0079	1.1	0.086	56.4	60	59.5

Table 16: Hee channel efficiencies (%) after selection cuts

selection step	qq	WW	ZZ	H 70 GeV	H 85	H 90
identification	0.028	0.16	4.2	52.5	50.4	53.8
$\sqrt{s'}$	0.021	0.15	4.1	52.1	50.2	53.8
M_{ll}	0.0010	0.012	1.8	44.5	43.8	47.9
$min(Pt_i)$	0.00021	0.0065	1.8	44.5	43.8	47.8
b tag	0.00021	0.0042	1.0	39.7	38.8	42.7

Table 17: H$\mu\mu$ channel efficiencies (%) after selection cuts

selection step	qq	WW	ZZ	Zee	total bkgd	DATA	H 70 GeV	H 85	H 90
identification	185.5	80.9	4.1	12.1	282.6	257	1.3	0.58	0.24
$\sqrt{s'}$	92.5	77.3	3.9	9.5	183.2	161	1.2	0.55	0.23
M_{ll}A	1.2	0.62	0.67	0.69	3.2	4	1.0	0.49	0.20
M_{ll}B	0.61	0.5	0.66	0.62	2.38	2	1.0	0.47	0.19
$min(Pt_i)$	0.19	0.11	0.63	0.43	1.4	1	0.97	0.46	0.19
E_1	0.19	0.11	0.59	0.26	1.2	1	0.96	0.46	0.19
btag	0.11	0.067	0.35	0.15	0.68	0	0.86	0.41	0.17

Table 18: Hee channel expected numbers after selection cuts

selection step	qq	WW	ZZ	total bkgd	DATA	H 70 GeV	H 85	H 90
identification	1.7	1.3	1.4	4.4	6	0.80	0.34	0.16
$\sqrt{s'}$	1.2	1.3	1.3	3.9	5	0.79	0.34	0.16
M_{ll}	0.061	0.10	0.58	0.74	1	0.68	0.30	0.14
$min(Pt_i)$	0.012	0.055	0.57	0.64	0	0.68	0.30	0.14
b tag	0.012	0.030	0.33	0.37	0	0.60	0.27	0.12

Table 19: H$\mu\mu$ channel expected numbers after selection cuts

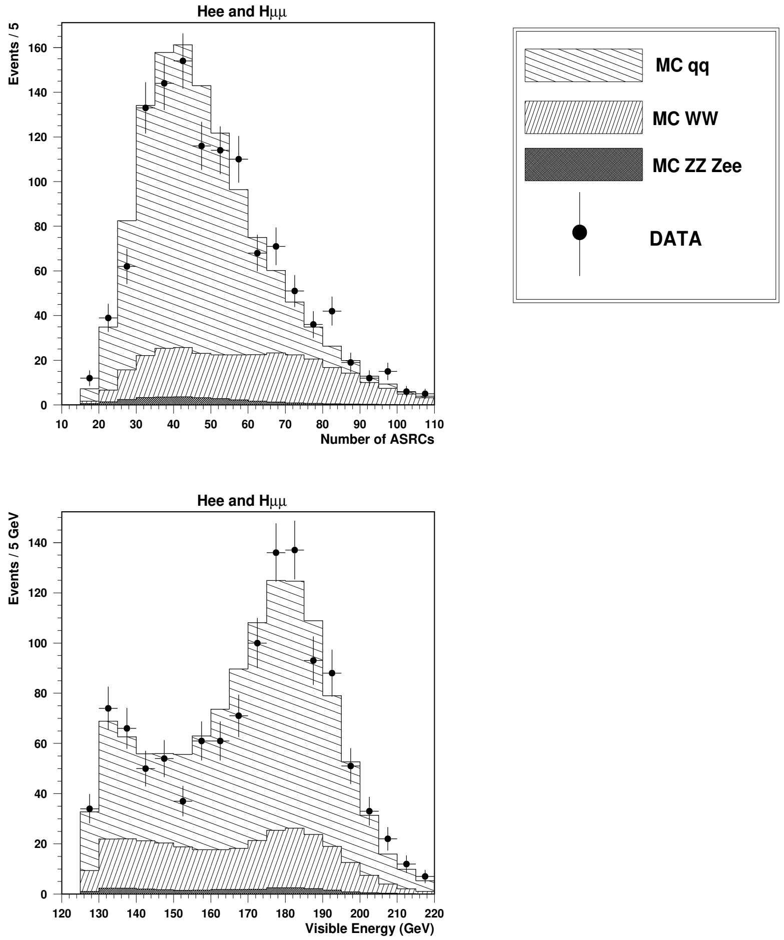

Figure 34: Number of ASRC'S and Visible energy distributions after preselection cuts ($\mathcal{L} = \bigtriangledown\bigtriangledown\sqrt{\lfloor^{-\infty}}$).

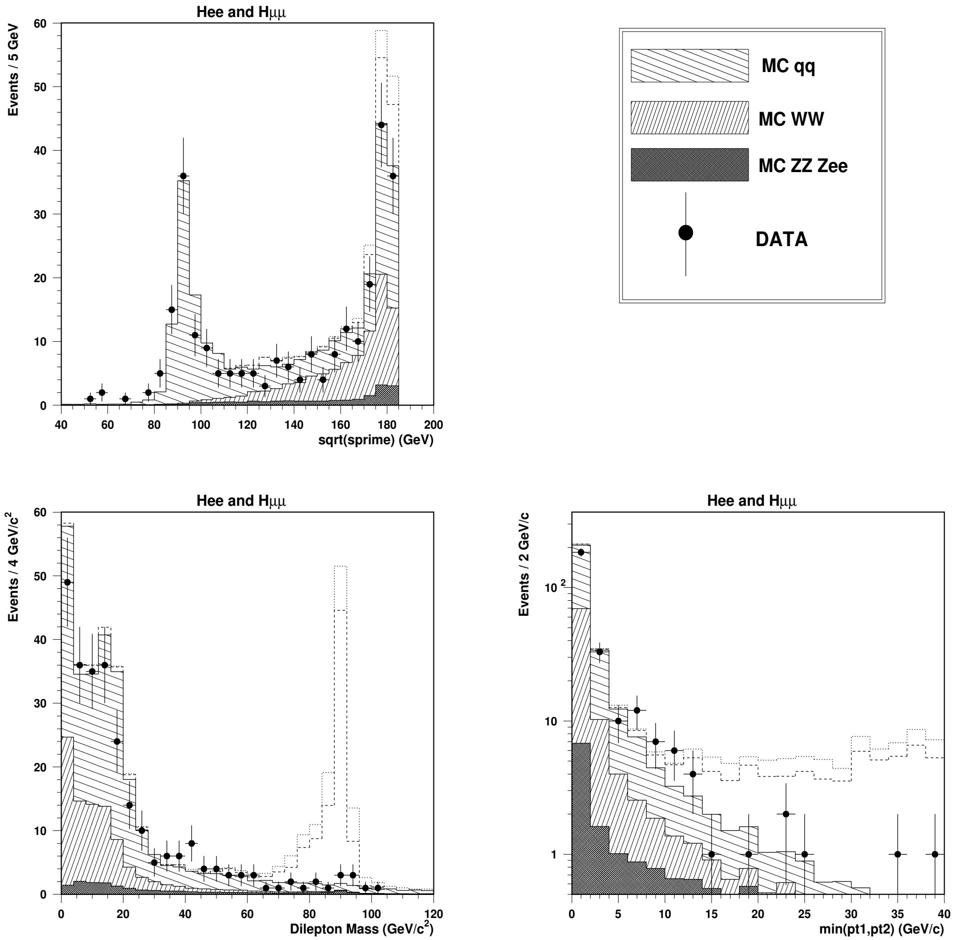

Figure 35: Distributions of selection variables, after identification ($\mathcal{L} = \bigtriangledown\bigtriangledown_{\surd}\lfloor^{-\infty}$). A Higgs signal of 90 GeV/c^2 is displayed on the same plot : Hee with dashed line and H$\mu\mu$ in dots.

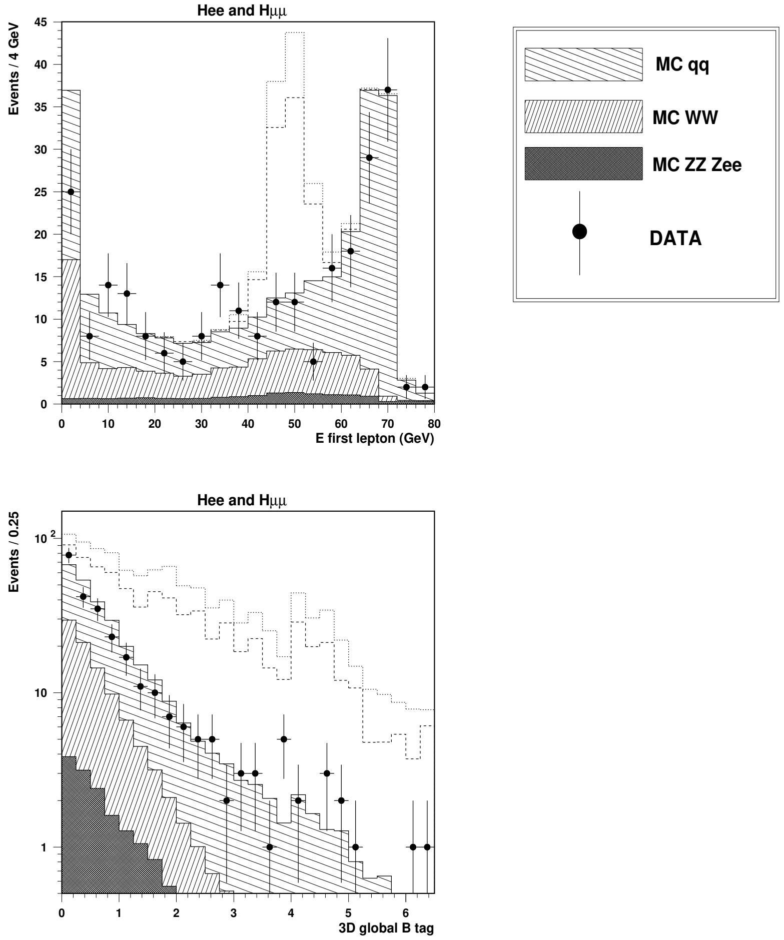

Figure 36: Distributions of selection variables, after identification ($\mathcal{L} = \bigtriangledown\bigtriangledown_{\surd}\lfloor^{-\infty}$). A Higgs signal of 90 GeV/c^2 is displayed on the same plot : Hee with dashed line and H$\mu\mu$ in dots.

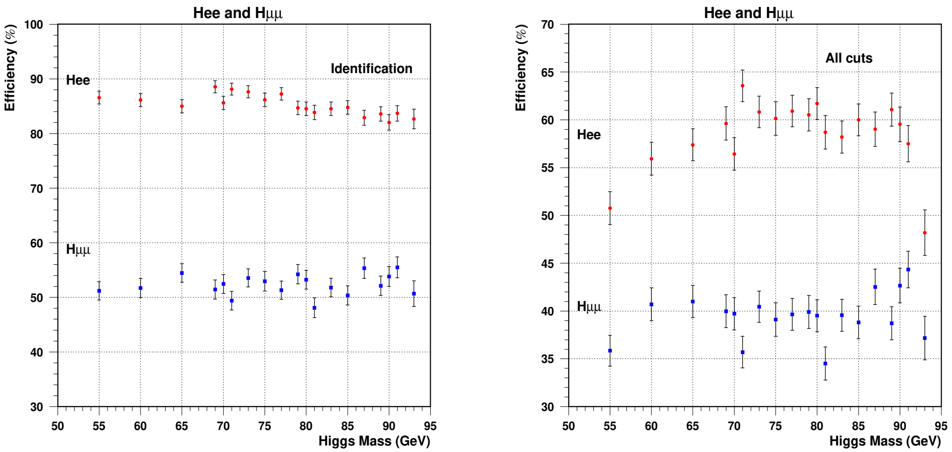

Figure 37: Higgs efficiencies after Identification and All cuts.

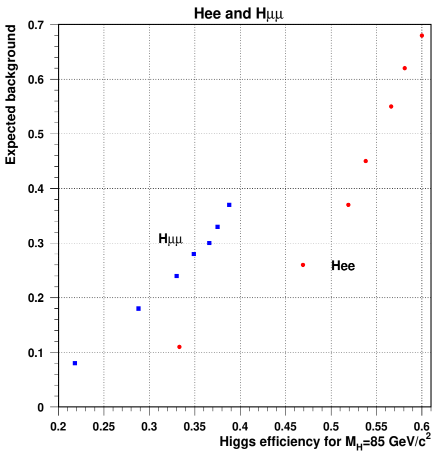

Figure 38: Expected background versus Higgs efficiency when tightening the cuts.

6.2 Discriminant Analysis for the $HZ \to q\bar{q}\ell^+\ell^-(\ell = e, \mu, \tau)$ and $HZ \to \tau^+\tau^- q\bar{q}$ channels

The analysis is based on an integrated luminosity of 55.3 pb $^{-1}$.

The selection procedure has been performed in 3 steps:

1. Common preselection for all channels: at least 4 scintillators in time, at least 9 tracks, at least 15 calorimetric clusters, $E_{vis}/\sqrt{s} \geq 0.4$, at least 2 leptons with $cos(\Theta_{ll}) \leq 0.7$, where Θ_{ll} is the opening angle between the leptons.
2. Channel dependent selection relying on particle identification and kinematics.
3. Construction of a final discriminant per channel using mass and btag information.

6.2.1 Selection for the $HZ \to q\bar{q}e^+e^-$ channel

The signature of the Hee channel is given by two hadronic jets and two high energetic electrons.

Two reconstructed jets and two identified electrons are required. At least one of the electrons must have a matched track (good electron). The selection criteria are shown in table 20. The comparison of data, expected background and signal efficiency can be found in table 21. The variable definitions are the following:
Θ_{JJ} : opening angle of the jets
E_{e_i} : energy of electron i
E_{J_i} : energy of jet i
$s_\Theta = |cos(\Theta_{e_1})| + |cos(\Theta_{e_2})|$, Θ_i polar angle of electron i
$A_{Sep_i} = min(\Theta_{e_iJ_1}, \Theta_{e_iJ_2})$: separation angle where $\Theta_{e_iJ_k}$ is the opening angle between electron i and jet k.
s' : reconstructed centre of mass energy
M_{ee}: reconstructed mass of the electron system
M_{JJ}: invariant mass of the jets after 5C-Fit
$A_{PLA} = min(|\phi_{J_1} - \phi_{J_2}|, 2 \cdot \pi - |\phi_{J_1} - \phi_{J_2}|)$
After performing a 5C kinematic Fit (assuming energy and momentum conservation and using the constraint that the invariant mass of the electrons equals the mass of the Z boson) a least square of the mass is defined as follows:

$$X_M = \frac{(M_{JJ} - M_H)^2}{\sigma^2_{M_{JJ}}}, \tag{8}$$

where M_H is the hypothesis on the Higgs mass.
A final discriminant is constructed using the distributions of X_M and the btag neural net output for the jets. The histograms of the distributions are shown in figure 40. The following functions are defined:

$$P_M(X_M) = \int_{X_M}^{\infty} p_M(X'_M)dX'_M \tag{9}$$

where p_M is the normalised distribution of X_M and

$$P_{J_i}(NN) = \int_0^{NN} p_{J_i}(NN')dNN' \tag{10}$$

where p_{J_i} is the normalised distribution of the NN for jet i from the signal. The final discriminant is defined as:

$$D = lg(P_M \cdot P_{J_1} \cdot P_{J_2}) \tag{11}$$

The distributions of D for different Higgs masses are shown in figure 41. The expected background as function of the signal efficiency can be derived from the final discriminant and is shown in figure 42.

Definition of selection steps	
C_1	2 jets, 1 good electron, 1 loose electron, $E_{e_i} \geq 20$ GeV,$cos(\Theta_{JJ}) \leq 0.2$, $s_\Theta \leq 1.88$ (1.83)
C_2	$70 \leq M_{ee}/GeV \leq 102$
C_3	$E_{J_1} + E_{J_2} \leq 115$ GeV (/), $A_{PLA} \leq 40°$ (/)
C_4	$A_{Sep_i} \geq 10°, i = 1, 2$
C_5	$\sqrt{s'}/\sqrt{s} \geq 0.82$
C_6	$D \geq -3.$

Table 20: Selection steps for which data and expectations for SM processes are compared for Hee (see Table 21). The number in brackets indicates the cut for the low mass range ($m_H \leq 75$ GeV)

Systematic and statistical errors: The uncertainties due to the topological cuts were estimated by varying all cuts of table 20 by a few percent and taking the biggest deviation from the original value (table 21) as systematic error on the cuts. The effect of this error

SM processes	N_{c1}	N_{c2}	N_{c3}	N_{c4}	N_{c5}	N_{c6}
$\gamma\gamma \rightarrow ee q\bar{q}$	8.1	3.6	0.	0.	0.	0.
$q\bar{q}(\gamma)$	5.1	2.5	2.3	1.3	0.8	0.3
$Z/\gamma^* Z/\gamma^* \rightarrow$all	0.8	0.6	0.6	0.6	0.5	0.4
WW$\rightarrow$all	1.0	1.0	0.3	0.2	0.04	0.02
Total Expected	15.0	7.7	3.2	2.1	1.3	0.7
Data	5	3	3	1	1	1
Eff.(%)(MH=87 GeV)	71.6	68.6	68.2	67.3	65.5	63.3

Table 21: Number of events expected from SM physics processes compared to the observed number of events in the data, after each selection step, described in Table 20. The MC expectations are normalised to the luminosity with the cross sections reported in Table 1. The signal efficiencies for a Higgs of 87 GeV as function of the cuts, are also shown.

on the signal efficiency is found to be 3 % and on the background expectation 12 % . The overall normalisation error on the background expectation is assumed to be 10 % .
The statistical error of the limited MC statistics is derived by dividing signal and background in 6 equally large event packets and calculating the variance assuming Gaussian statistics. The statistical error on the signal is calculated to be 6 % and on the background expectation it is 19 % .
Assuming that systematic and statistical errors are completely uncorrelated the error on the signal efficiency is 7 % and the uncertainty on the background expectation is 25 % .

6.2.2 Selection for $HZ \rightarrow q\bar{q}\mu^+\mu^-$ channel

The search for the Higgs boson in the decay channel $HZ \rightarrow bb\mu\mu$ is performed on analogy to the electron channel. Two high energetic muons are required accompanied by two hadronic jets. The cuts are defined in table 22. Signal efficiency, background expectation and the number of data events after each selection step are compared in table 23. The distribution, that are used for the construction of the final discriminant, are shown in figure 43. The background expectation as function of the signal efficiency is shown in figure 44.

Systematic and statistical errors: Following the procedure described in section 6.2.1, the systematic error on the signal efficiency is found to be 1 % and the systematic error on the background expectation is 11 %. The statistical uncertainty accounts 9 % for the signal efficiency and 20 % for the background leading to an overall error of 9 % for the signal efficiency and 25 % for the background expectation.

6.2.3 Inclusive selection for $HZ \rightarrow bb\tau\tau$ and $HZ \rightarrow \tau\tau qq$ channels

Tau leptons are identified as low multiplicity jets comprising not more than 5 calorimetric clusters in a cone of 10° and not more than 3 tracks in a cone of 30° half-angle around

Definition of selection steps	
C_1	2 Muons + 2 Jets $E_\mu \geq 5$ GeV
C_2	$\sqrt{s'}/\sqrt{s} \geq 0.7$
C_3	$\chi^2_{Fit} \leq 100$
C_4	$D \geq -3.5$

Table 22: Selection steps for which data and expectations for SM processes are compared for H$\mu\mu$ (see Table 23).

SM processes	N_{c1}	N_{c2}	N_{c3}	N_{c4}
$\gamma\gamma \to ee$q$\bar{\text{q}}$	0	0	0	0
q$\bar{\text{q}}(\gamma)$	1.0	0.6	0.3	0.3
Z/γ^*Z/γ^* $\to$all	1.2	1.2	0.6	0.5
WW$\to$all	1.0	0.5	0.1	0.1
Total Expected	3.2	2.3	1.0	0.9
Data	6	5	0	0
Eff.(%)(MH=87 GeV)	57.0	55.7	54.3	53.7

Table 23: Number of events expected from SM physics processes compared to the observed number of events in the data, after each selection step, described in Table 22. The MC expectations are normalised to the luminosity with the cross sections reported in Table 1. The signal efficiencies for a Higgs of 87 GeV as function of the cuts, are also shown.

their direction. The measured energy of the decay particles should be at least 4 GeV and the ratio of the energy, measured in the range of 10° to 30° and 0° to 10° around the flight direction, should not exceed 0.3. The reconstructed charge of the tau candidate is required to be one.
High multiplicity hadronic events are selected with at least 9 tracks and 15 calorimetric clusters. Two jets and two tau candidates with a separation angle of at least 0.17 rad are required. The effective centre-of-mass energy should be within $0.5 \leq \sqrt{s'}/\sqrt{s} \leq 0.97$ and the missing momentum vector must be larger than 5 GeV.

The $HZ \to bb\tau\tau$ and the $HZ \to \tau\tau qq$ channel are distinguished by using the mass and the btag information. The btag neural net output distribution for jet2 is integrated in the following way:

$$P_{J2}^{bb\tau\tau} = \int_0^{NN} p_{J2}^{bb\tau\tau}(NN')dNN' \qquad (12)$$

Definition of selection steps	
C_1	2 Jets + 2 Taus $E_\tau \geq 4GeV, A_{Sep_i} \geq 10°$, $i = 1,2$
C_2	$0.5 \leq \sqrt{s'}/\sqrt{s} \leq 0.97$, $P_{Miss} \geq 5$
C_3	$60 \leq M_Z^{Rec}/GeV \leq 118$, $\chi^2_{Fit} \leq 60$
C_4	$X_M \leq 8$

Table 24: Selection steps for the τ channels. Data and expectations for SM processes are compared in table 25 and in table 26

SM processes	N_{c1}	N_{c2}	N_{c3}	N_{c4}
$\gamma\gamma \to ee$q$\bar{\text{q}}$	1.8	0.9	0	0
q$\bar{\text{q}}(\gamma)$	1.6	1.0	0.1	0
Z/γ^*Z/γ^* $\to$all	0.7	0.5	0.3	0.2
WW$\to$all	4.7	4.3	0.7	0.2
Total Expected	8.8	6.7	1.1	0.4
Data	4	3	0	0
Eff.(%)(MH=87 GeV)	27.9	26.7	24.9	23.7

Table 25: Number of events expected from SM physics processes compared to the observed number of events in the data, after each selection step, described in Table 24 for $HZ \to qq\tau\tau$. The MC expectations are normalised to the luminosity with the cross sections reported in Table 1. The signal efficiencies for a Higgs of 87 GeV as function of the cuts, are also shown.

$$P_{J2}^{\tau\tau qq} = \int_{NN}^{1} p_{J2}^{\tau\tau qq}(NN')dNN' \qquad (13)$$

The obtained probability functions are shown in figure 39.

The least square X_M (see section 6.2.1) is constructed using the directly reconstructed dijet masses for both mass hypothesises. The product $P_M^{bb\tau\tau} \cdot P_{J2}^{bb\tau\tau}$ is compared to $P_M^{\tau\tau qq} P_{J2}^{\tau\tau qq}$ and the events are selected depending on the value of each of the products. A comparison of data, expected background and signal efficiency is given in the tables 25 and 26. The discriminants and the background expectation as function of the signal efficiency are presented in figure 45 and 46.

Systematic and statistical errors: The systematic error of the signal efficiency is found to be 3 %, on the background expectation it is 21 %. The statistical error for the signal efficiency is calculated to be 12 % and for the background expectation 14 % leading to a total error on the signal efficiency of 12 % and on the background expectation of 25 %.

SM processes	N_{c1}	N_{c2}	N_{c3}	N_{c4}
$\gamma\gamma \rightarrow ee\mathrm{q\bar{q}}$	1.8	0.9	0	0
$\mathrm{q\bar{q}}(\gamma)$	5.1	3.2	1.0	0.04
$\mathrm{Z}/\gamma^{*}\mathrm{Z}/\gamma^{*} \rightarrow$all	2.3	1.2	1.0	0.3
WW$\rightarrow$all	8.2	6.1	2.0	0.3
Total Expected	17.4	11.4	4.0	0.6
Data	17	9	4	1
Eff.(%)(MH=87 GeV)	28.8	27.2	25.2	22.7

Table 26: Number of events expected from SM physics processes compared to the observed number of events in the data, after each selection step, described in Table 24 for $HZ \rightarrow \tau\tau qq$. The MC expectations are normalised to the luminosity with the cross sections reported in Table 1. The signal efficiencies for a Higgs of 87 GeV as function of the cuts, are also shown.

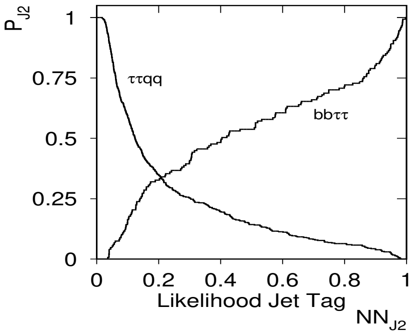

Figure 39: Integrated btag distribution for $bb\tau\tau$ and $\tau\tau qq$.

6.2.4 Results

There has been no excess seen in any of the investigated channels in comparison to the expectation from Standard Model background processes. Two candidates have been found with masses both around 90 GeV. Figure 47 summarises the behaviour of the analysis in the four investigated leptonic channels for different Higgs masses.

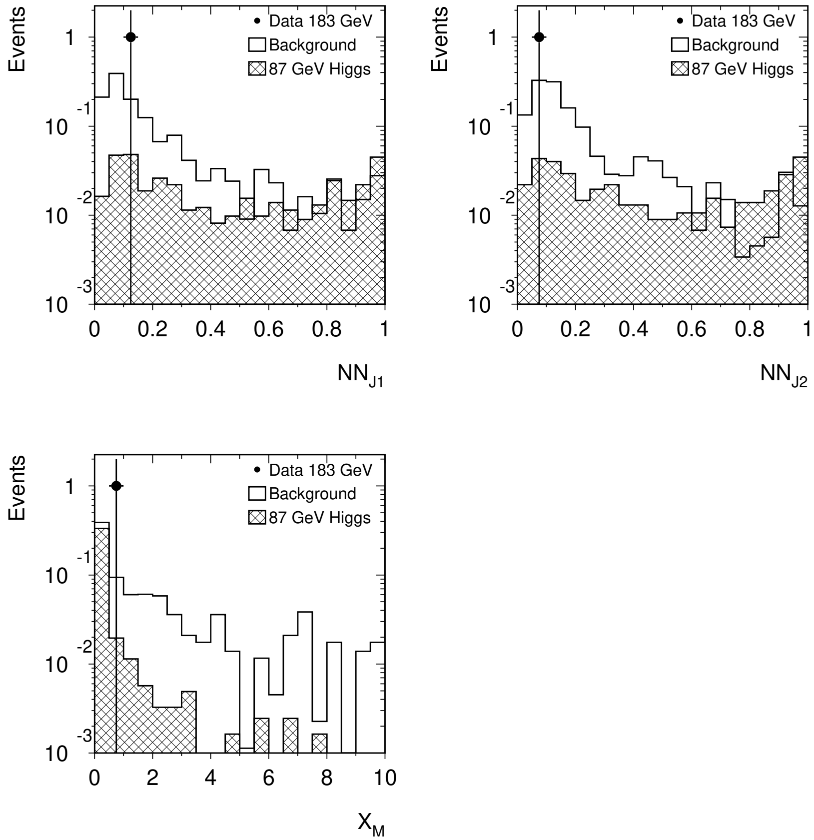

Figure 40: Btag neural net output for the jets and least square distribution X_M for Hee after the selection described in table 20 for data, background and signal for a Higgs mass of 87 GeV.

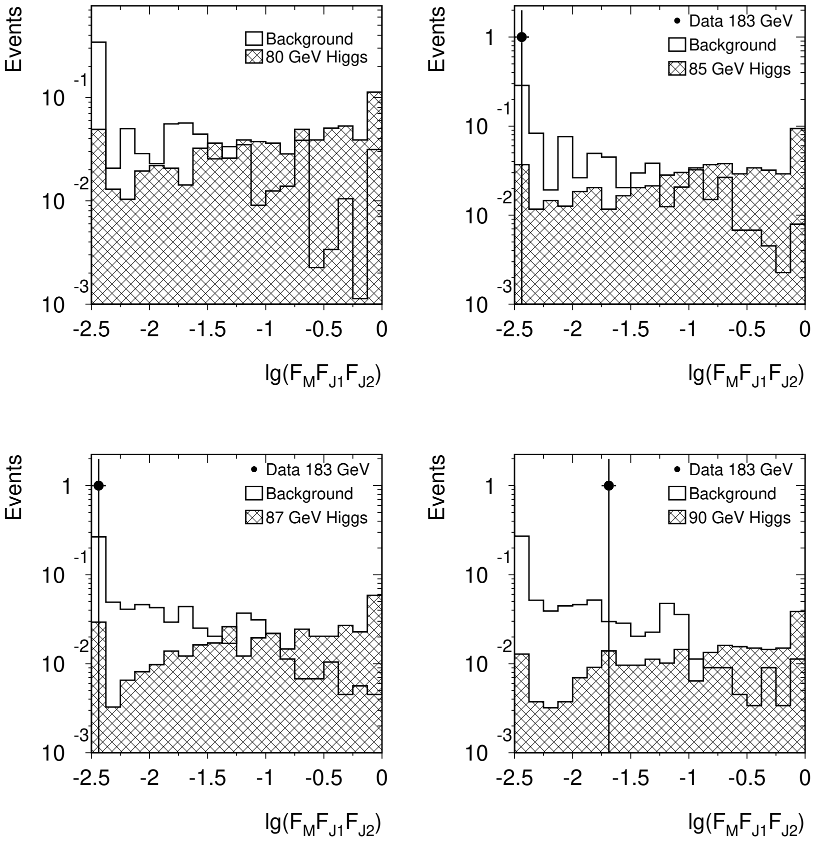

Figure 41: Final discriminant distribution for data, background and the signal Hee, for Higgs masses of 80, 85, 87 and 90 GeV. The candidate moves towards higher probability values if one goes to higher Higgs masses.

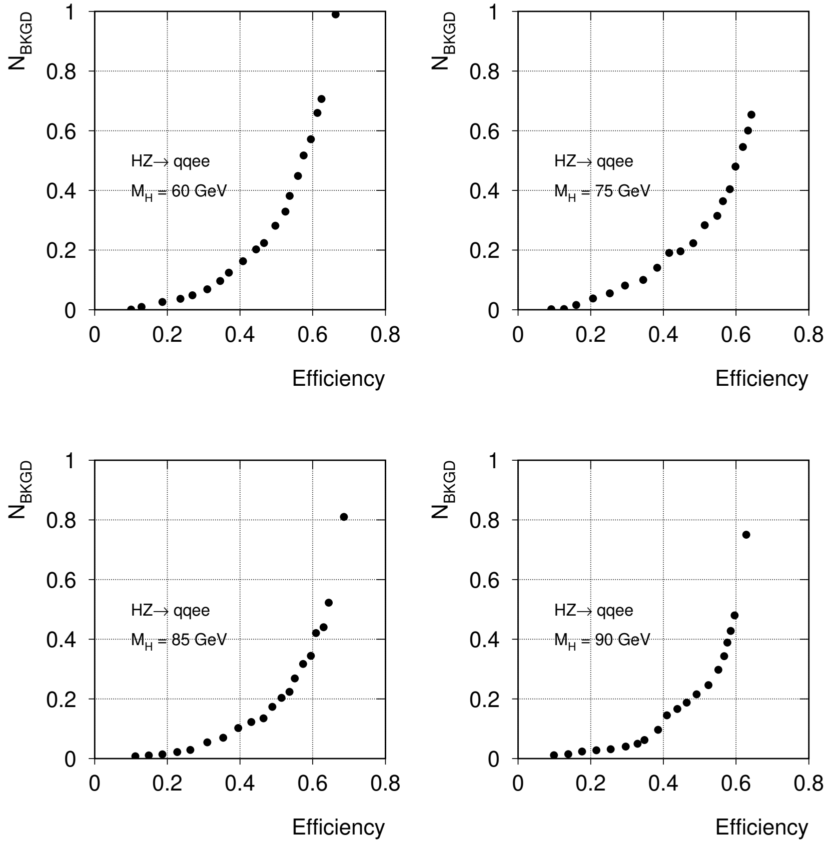

Figure 42: Expected background versus signal efficiency for Hee for $M_H = 60, 75, 85, 90$ GeV.

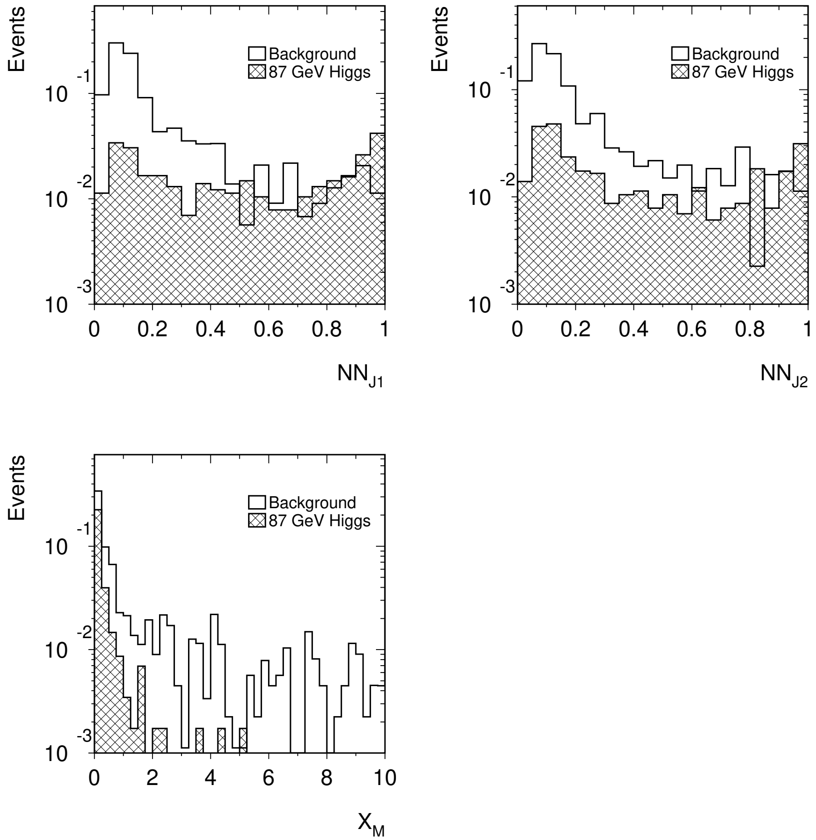

Figure 43: Btag neural net output for the jets and least square distribution X_M for H$\mu\mu$ after the selection described in table 22 for data, background and signal for a Higgs mass of 87 GeV.

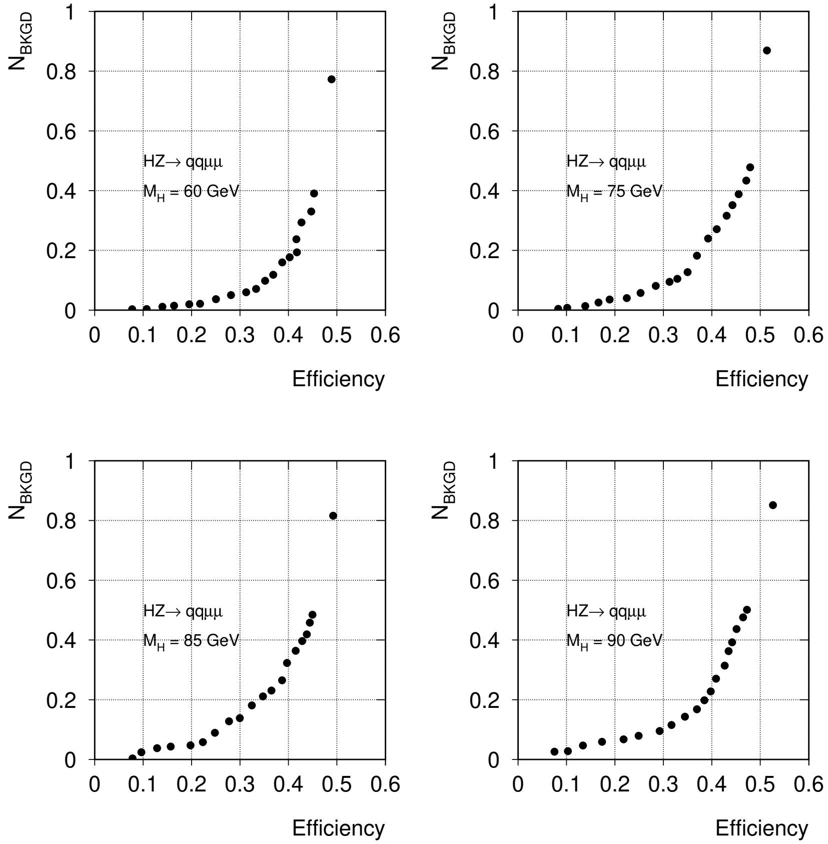

Figure 44: Expected background versus signal efficiency for H$\mu\mu$ for $M_H = 60, 75, 85, 90$ GeV.

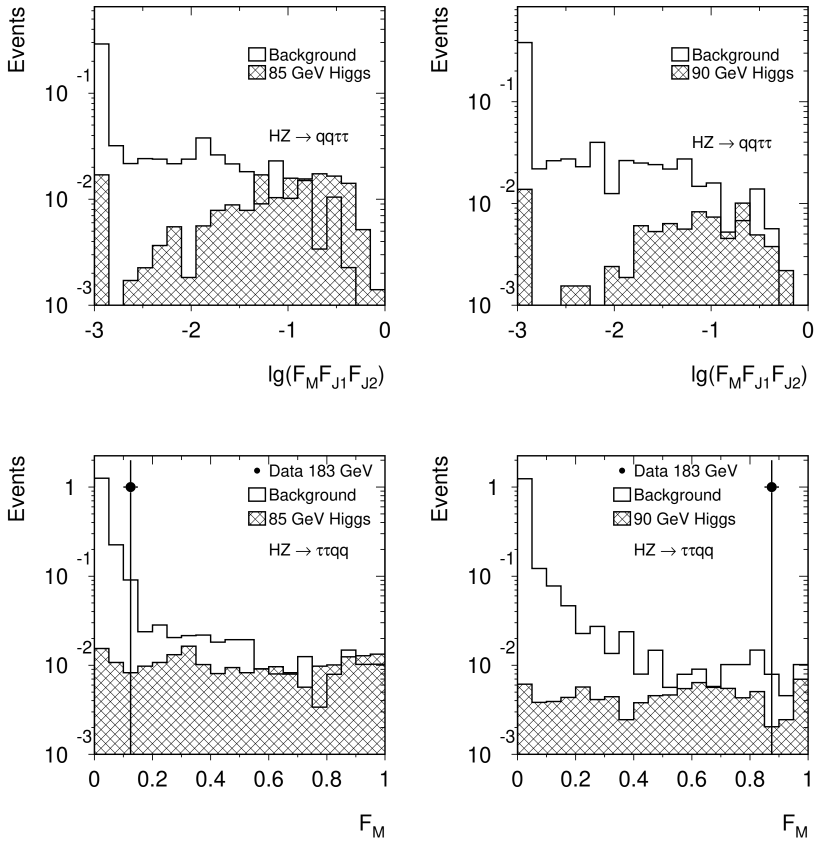

Figure 45: Final discriminant distribution for data, background and the signal (τ channels), for Higgs masses of 85 and 90 GeV.

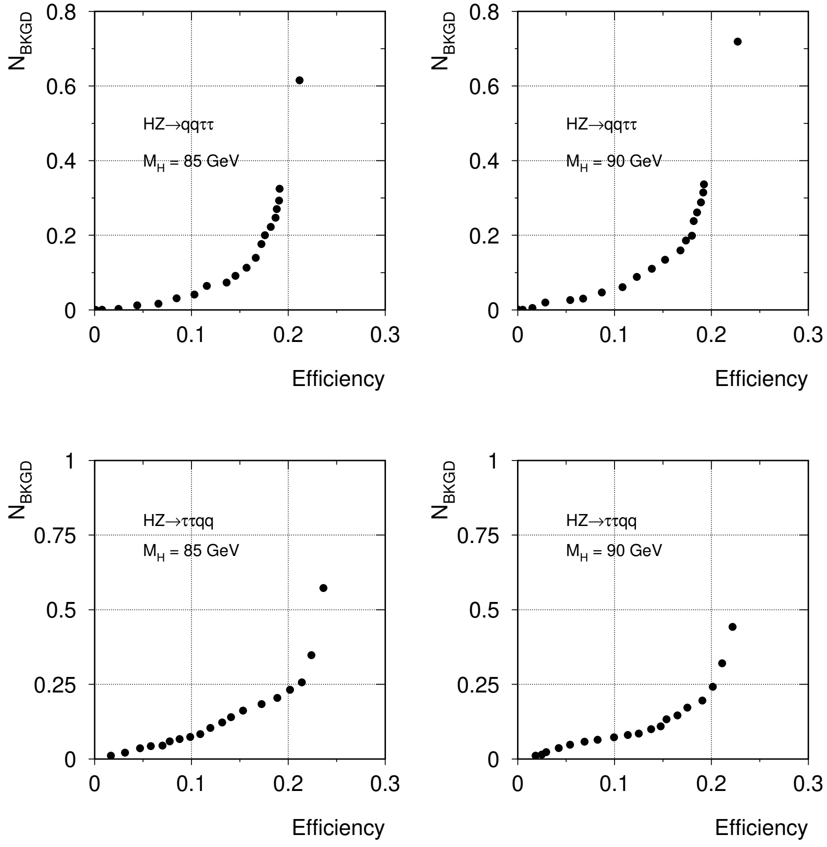

Figure 46: Expected background versus signal efficiency for the τ channels for Higgs masses of 85 and 90 GeV

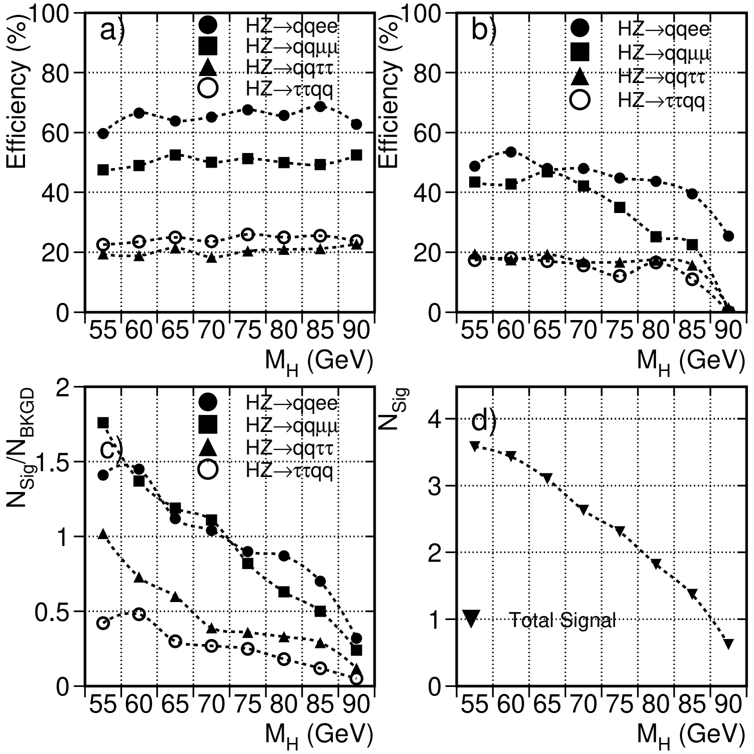

Figure 47: a) Comparison of the signal efficiency for different Higgs masses, b) Comparison of the signal efficiency after a Signal/Noise cut of 3 for Hee and H$\mu\mu$ and of 1 for the τ channels, c) Signal to Noise ratio, d) Total number of expected signal events for the 4 channels combined

6.3 Neural Network analysis for $HZ \to q\bar{q}e^+e^-$ and $HZ \to q\bar{q}\mu^+\mu^-$ channels

6.3.1 The He$^+$e$^-$ channel

The specific signature of He$^+$e$^-$ and is a pair of two high energy electrons with the invariant mass close to M_Z accompanied by two hadronic jets.

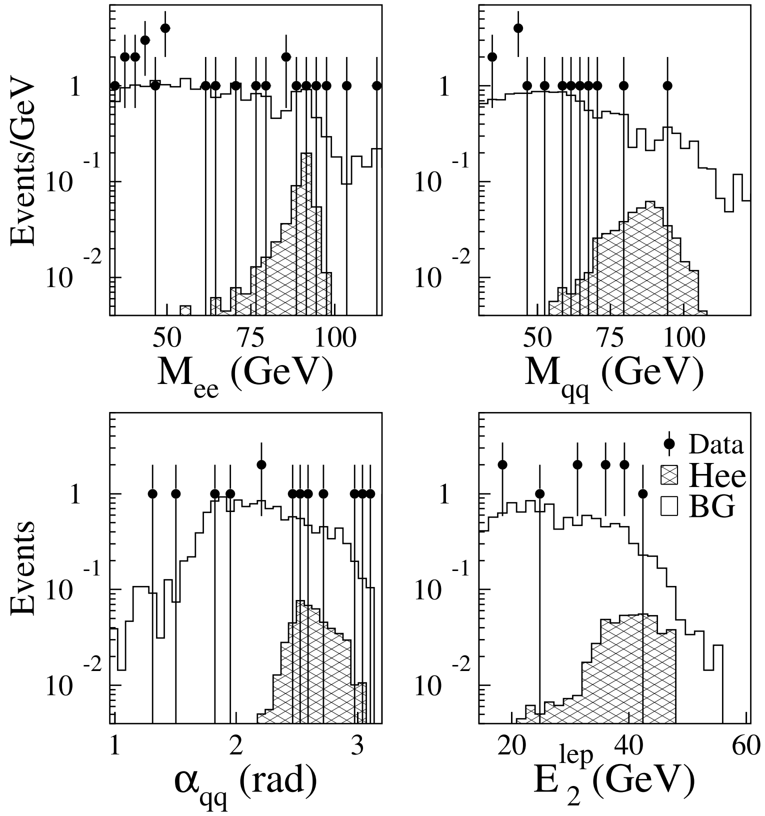

Figure 48: Data, expected background and 85 GeV signal for the most important variables used in the He$^+$e$^-$ preselection.

High multiplicity hadronic events with more than four tracks, more than twenty calorimetric energy clusters and two high energy electrons, $E_{\mathrm{lept}} > 15$ GeV, are selected. The $\mathrm{He^+e^-}$ selection requires one electron to be identified as a shower having an electromagnetic shape and a track pointing to it, while the only requirement on another is that it has at least 15 GeV of energy deposition in the calorimeters. The total energy deposition in the electromagnetic calorimeter must exceed 90 GeV. This selection allows to keep acceptance high for $\mathrm{He^+e^-}$ events where one of the electrons produces a shower in the vicinity of non-homogenius regions in the detector.

The angle between the electrons is required to exceed 1.8 rad and the invariant mass of the hadronic system, M_{had}, has to be greater than 35 GeV. The selection flow is presented in Table 27, and illustrated in Figure 48.

preselection cut	N_{data}	N_{bg}	ε_{87}
hadronic preselection 2 loose electrons 1 good electron	30	24.1	81.8%
$60 < \mathrm{M_{ee}} < 110$ GeV	21	17.0	81.5%
$35 < \mathrm{M_{qq}} < 120$ GeV	13	12.5	81.3%
$\alpha_{\mathrm{ee}} > 1.8$ rad $\alpha_{\mathrm{qq}} > 1.6$ rad	9	10.0	81.1%
$\mathrm{E}_{\ell_2} > 20$ GeV	7	8.1	80.1%
$\mathrm{E_{BGO}} > 90$ GeV	7	6.5	77.4%
cuts on NN inputs	6	5.7	74.3%

Table 27: Number of events expected from SM physics precesses compared to the observed number of events in the data, after each major selection step. The MC expectations are normalised to the luminosity and the SM cross sections. The signal efficiencies for a Higgs of 87 GeV as function of the cuts, are also shown.

Six $\mathrm{He^+e^-}$ candidate events are selected consistent with the background expectation of 5.7 events. The signal efficiency as a function of Higgs mass is presented in Table 28.

	65 GeV	70 GeV	75 GeV	80 GeV	85 GeV	90 GeV
NN > 0.0	68.6%	74.3%	76.1%	77.8%	79.7%	75.0%
NN > 0.5	54.2%	55.3%	58.4%	60.3%	61.6%	55.6%

Table 28: Signal efficiency as a function of Higgs mass.

Neural network is then used to construct a discriminant variable that further separates the signal from the background. The effort is made to make neural net inputs independent on the reconstructed $\mathrm{M_H^{5C}}$ mass. Six variables are used as an input to the net, four of them are presented in Figure 49 before applying the cuts on that variable. In general they

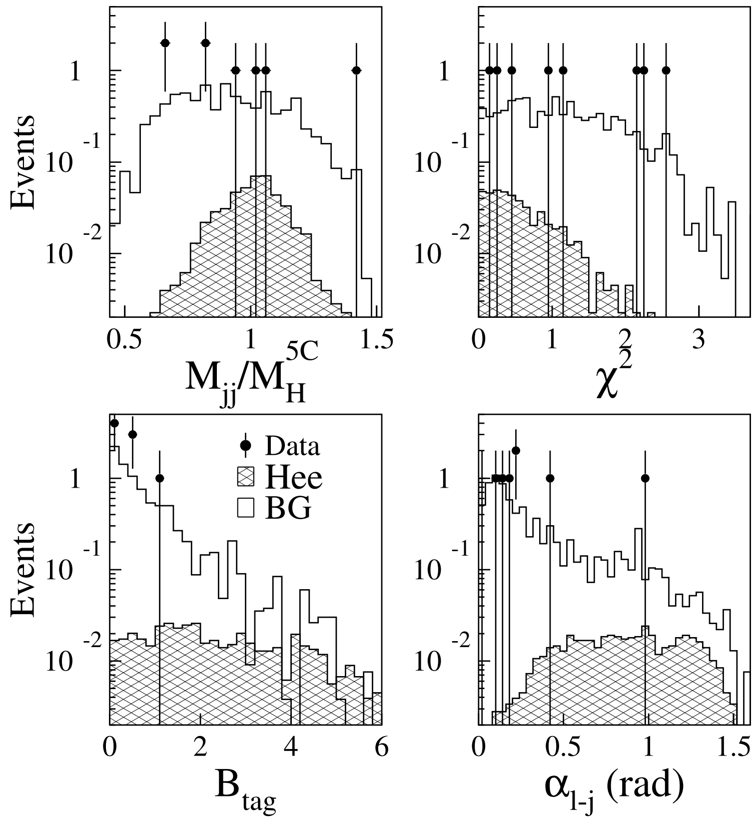

Figure 49: Data, expected background and 85 GeV signal for the most important variables used as inputs for $\mathrm{He^+e^-}$ neural network.

are similar to those used for last year analysis [1,2] but are normalised to a characteristic quantity derived from the kinematic fit. The neural network is trained over one-third the Monte Carlo sample. In the training procedure events $\mathrm{ZZ} \rightarrow \mathrm{b\bar{b}e^+e^-}$ were not used as they are indistinguishable from the signal events. The spectrum of the neural net output variable is presented in Figure 50a.

The kinematic fit that uses energy and momentum conservation and constrains the

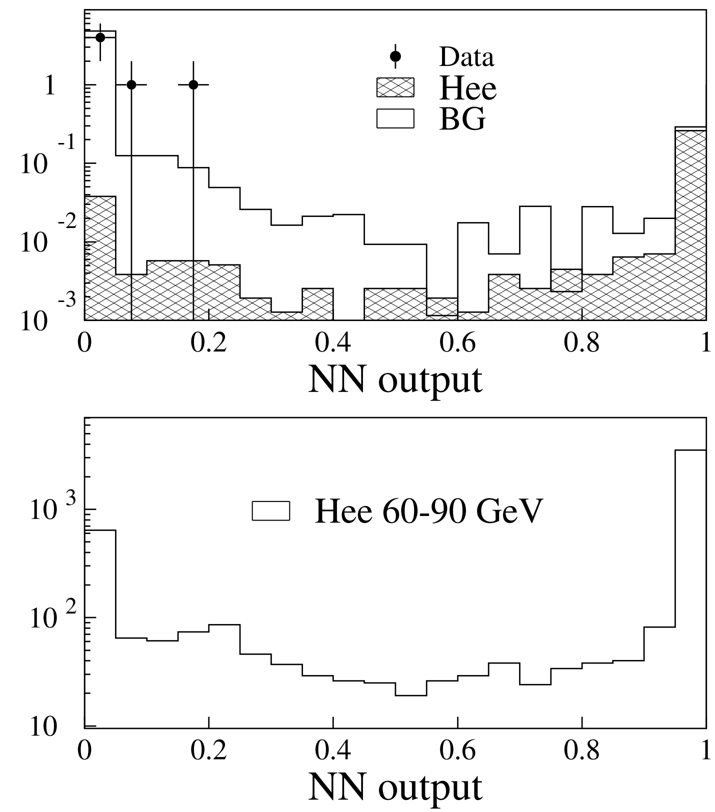

Figure 50: Data, expected background and 87 GeV signal for the He^+e^- neural network output.

recoiling mass to M_Z is applied to the hadronic jets in the selected events. The result of the fit along with the recoil mass to two electrons is used to build reconstructed Higgs mass to improve the mass resolution for the signal events. The invariant mass resolution after this fit is about 1.8 GeV for the central part of the distribution and the mass interval between 80 and 90 GeV (see Figure 51). This mass (M_H^{5C}) and the mass-independent neural net output (shown in Figure 50b) are used to evaluate consistency of an event with

the given Higgs mass hypothesis (this variable has meaning of purity for given values NN output and M_H^{5C}). The spectra of this variable for the several Higgs mass hypothesis are presented in Figure 52. They are used for the limit calculations.

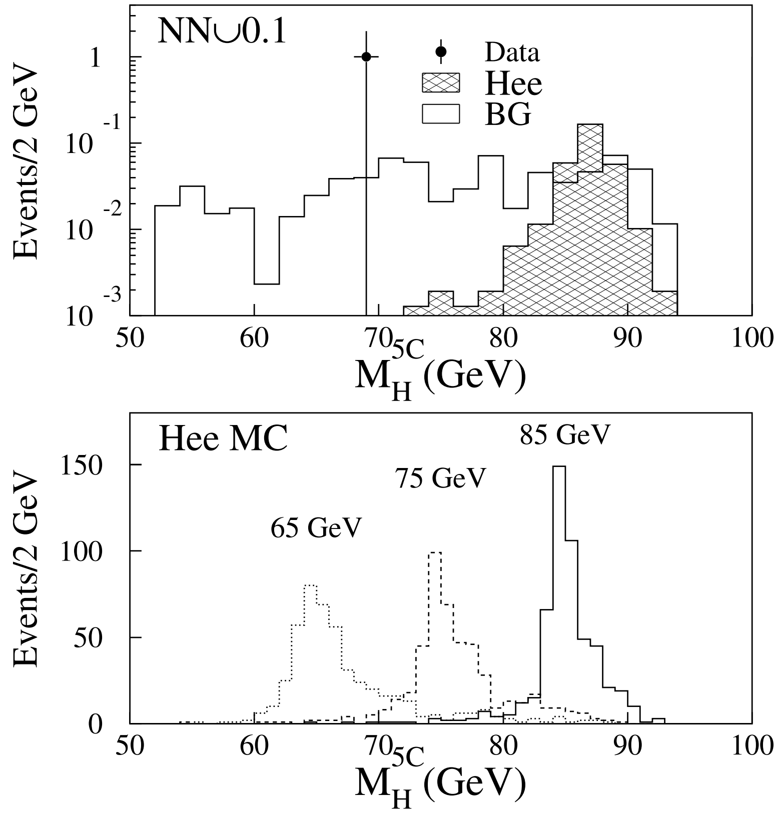

Figure 51: The M_H^{5C} spectrum for data, expected background and 87 GeV signal for the events satisfying NN > 0.1. The bottom plot shows M_H^{5C} spectra for the different Higgs boson masses for the He^+e^- analysis.

The final picture that represents the quality of this analysis is the Higgs signal efficiency versus the number of background events for 87 GeV Higgs mass hypothesis (Figure 53).

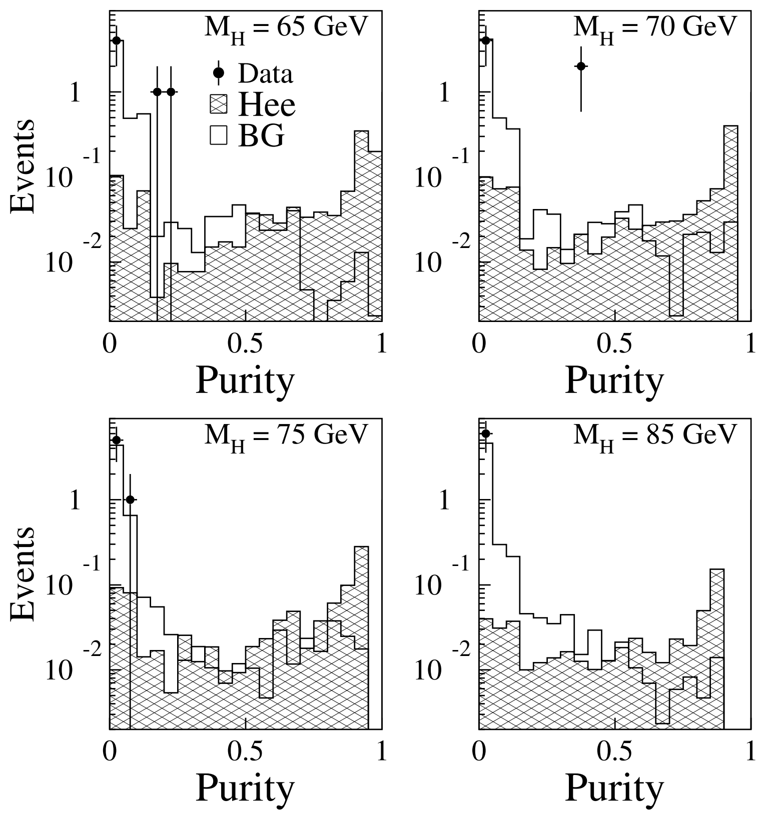

Figure 52: Data, expected background and signal for the purity variable for several Higgs mass hypotheses in the He^+e^- analysis.

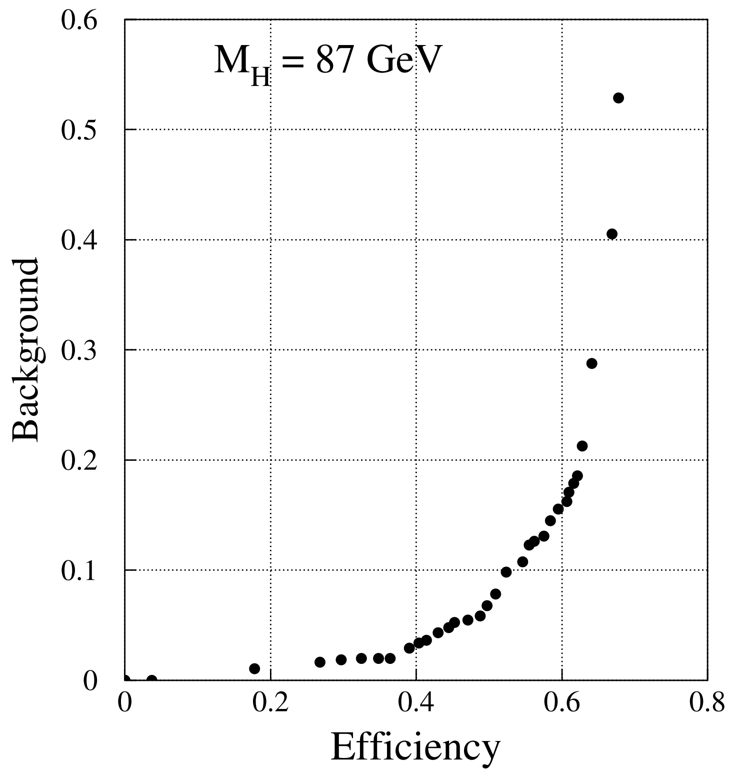

Figure 53: The Higgs signal efficiency versus the number of background events for 87 GeV Higgs mass hypothesis for the He^+e^- analysis.

6.3.2 The H$\mu^+\mu^-$ channel

The specific signature of H$\mu^+\mu^-$ and is a pair of two high energy muons with the invariant mass close to M_Z accompanied by two hadronic jets.

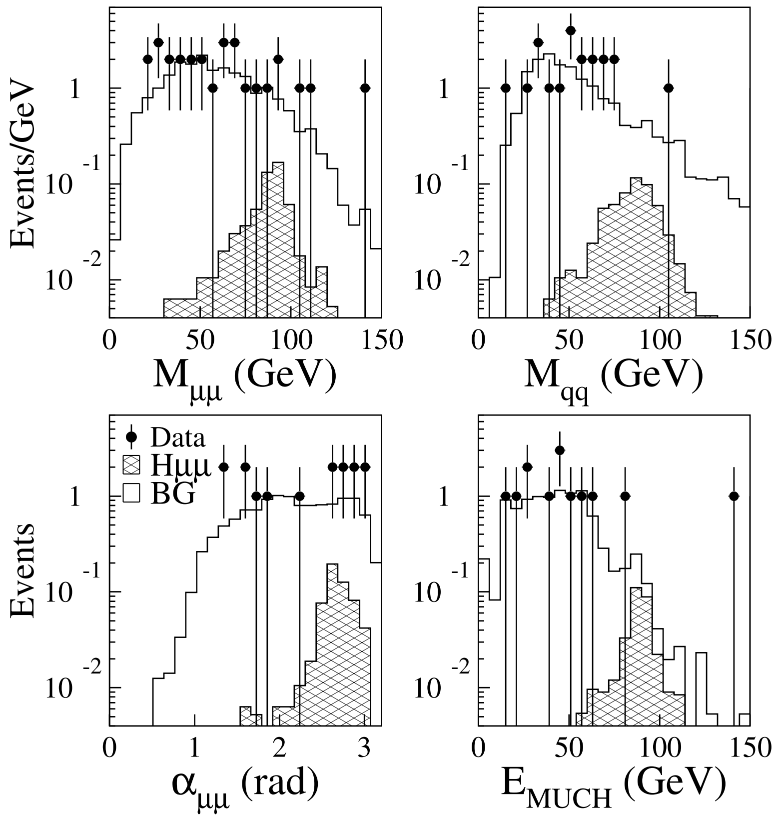

Figure 54: Data, expected background and 85 GeV signal for the most important variables used in the H$\mu^+\mu^-$ preselection. The selection criteria are applied sequentially as described in the text.

High multiplicity hadronic events with more than four tracks and more than twenty calorimetric energy clusters and two high energy leptons, $E_{\text{lept}} > 15$ GeV, are selected. One of the muons is required to be identified as a track in the Muon Chamber system, another is not. The total momentum of muons detected in the Muon Chambers must exceed 30 GeV. This selection allows to keep acceptance high for H$\mu^+\mu^-$ events where one of the muons escapes detection in the Muon Chambers and is identified as a minimum ionising particle in the calorimeters.

The angle between the leptons is required to exceed 1.5 rad, the invariant mass of the muons, $M_{\mu\mu}$, has to be greater than 35 GeV and the invariant mass of the hadronic system, M_{had}, has to be greater than 35 GeV. The selection flow is presented in Table 29, and is illustrated in Figure 54.

preselection cut	N_{data}	N_{bg}	ε_{87}
hadronic preselection 2 loose muons 1 good muon	30	20.3	59.4%
35 < $M_{\mu\mu}$ < 125 GeV	20	16.5	56.8%
35 < M_{qq} < 125 GeV	15	12.2	54.9%
$\alpha_{\mu\mu}$ > 1.5 rad α_{qq} > 1.5 rad	13	10.0	53.7%
E_{MUCH} > 30 GeV	9	7.1	53.6%
E_{MUCH}/E_Z^{5C} > 0.5	4	2.4	50.7%
cuts on NN inputs	2	1.4	47.5%

Table 29: Number of events expected from SM physics precesses compared to the observed number of events in the data, after each major selection step. The MC expectations are normalised to the luminosity with the SM cross sections. The signal efficiencies for a Higgs of 87 GeV as function of the cuts, are also shown.

Two H$\mu^+\mu^-$ candidate events are selected consistent with the background expectation of 1.4 events. The signal efficiency as a function of Higgs mass is presented in Table 30.

	65 GeV	70 GeV	75 GeV	80 GeV	85 GeV	90 GeV
NN > 0.0	45.7%	44.0%	42.4%	44.9%	44.5%	48.6%
NN > 0.5	40.2%	38.7%	39.2%	39.7%	40.5%	42.4%

Table 30: Signal efficiency as a function of Higgs mass.

Neural network is then used to construct a discriminant variable that further separates the signal from the background. The effort is made to make neural net inputs independent on the reconstructed M_H^{5C} mass. Six variables are used as an input to the net, four of them are presented in Figure 55 before applying the cuts on that variable. In general they are similar to those used for last year analysis [1, 2] but are normalised to a characteristic quantity derived from the kinematic fit. The neural network is trained over one-third the

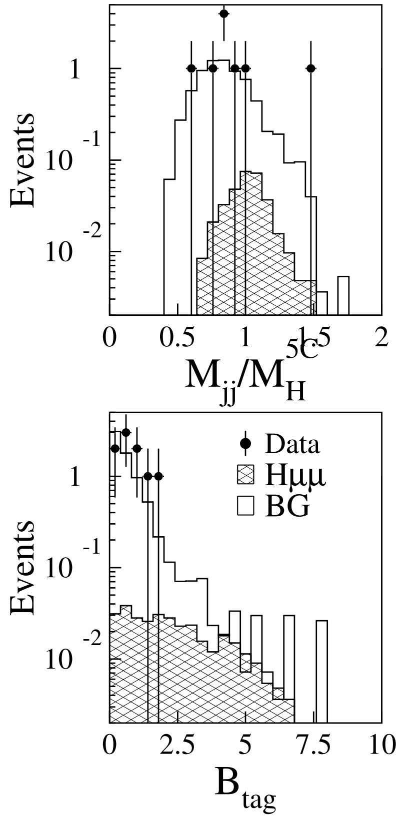

Figure 55: Data, expected background and 85 GeV signal for the most important variables used as inputs for $H\mu^+\mu^-$ neural network.

Monte Carlo sample. In the training procedure events $ZZ \to b\bar{b}\mu^+\mu^-$ were not used as they are indistinguishable from the signal events. The spectrum of the neural net output variable is presented in Figure 56a.

The kinematic fit that uses energy and momentum conservation and constrains the recoiling mass to M_Z is applied to the hadronic jets in the selected events. The result of the fit along with the recoil mass to two muons is used to build reconstructed Higgs mass

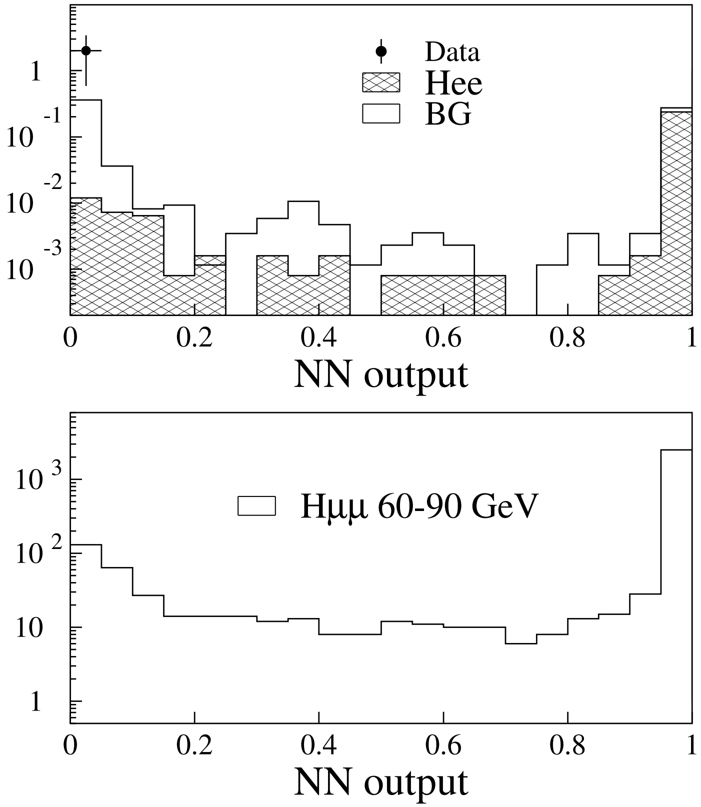

Figure 56: Data, expected background and 85 GeV signal for the $H\mu^+\mu^-$ neural network output.

to improve the mass resolution for the signal events. The invariant mass resolution after this fit is about 2.4 GeV for the central part of the distribution (see Figure 57). This mass (M_H^{5C}) and the mass independent neural net output (presented in Figure 56b) are used to evaluate consistency of an event with the given Higgs mass hypothesis (this variable has meaning of purity for given values NN output and M_H^{5C}). The spectra of this variable for the several Higgs mass hypothesis are presented in Figure 58.

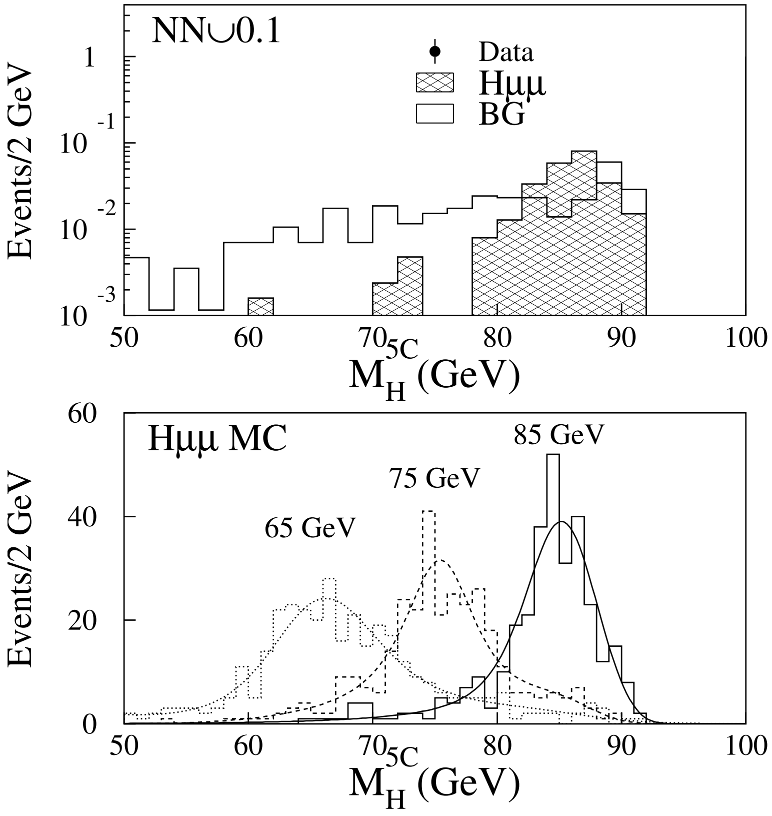

Figure 57: The reconstructed Higgs mass distribution for the $H\mu^+\mu^-$ events satisfying the requirement NN > 0.1.

The final picture that represents the quality of this analysis is the Higgs signal efficiency versus the number of background events for 85 GeV Higgs mass hypothesis (Figure 59).

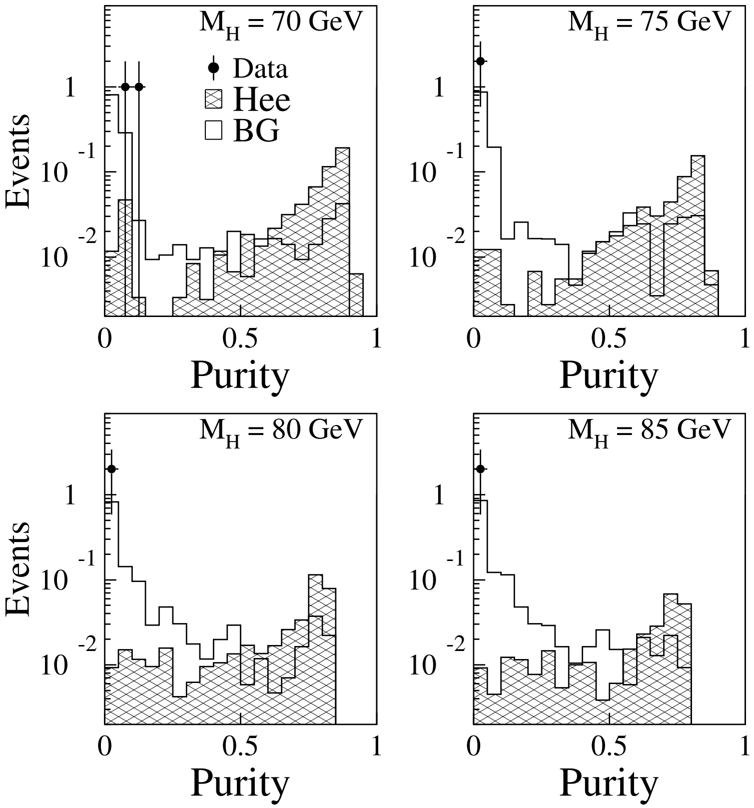

Figure 58: Data, expected background and signal for the purity variable for several Higgs mass hypotheses in the $H\mu^+\mu^-$ analysis.

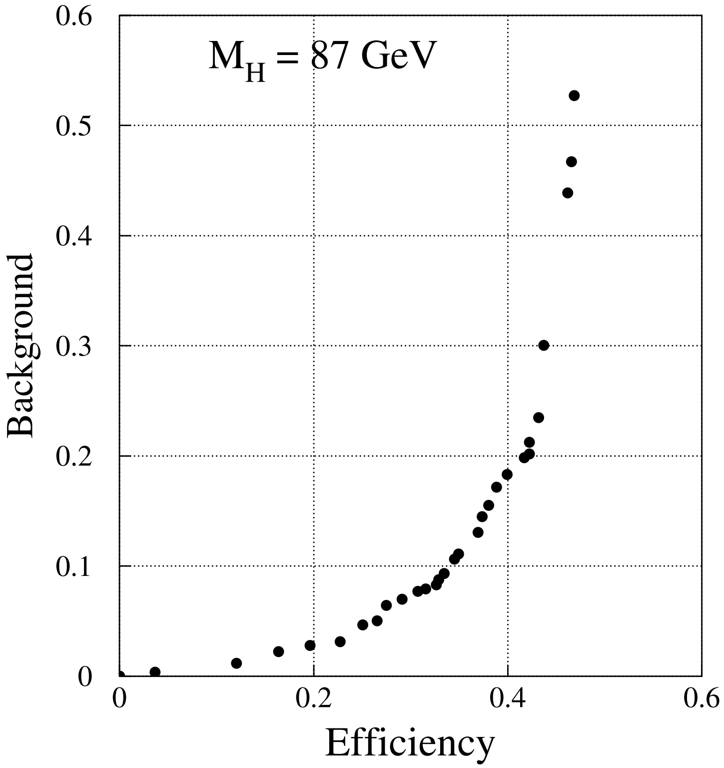

Figure 59: The number of expected Higgs signal events (dashed line) and the number of signal events excluded at 95% confidence level as functions of the Higgs boson mass for the $H\mu^+\mu^-$ analysis.

6.4 The optimised cuts analysis for the $HZ \to \tau^+\tau^- b\bar{b}$ and $HZ \to q\bar{q}\tau^+\tau^-$ channels

The following analysis is a straightforward product of the dedicated analysis to the search for the MSSM Higgs bosons. It is here applied to the SM channels, as a check of the dedicated analysis for the SM Higgs boson search. The used luminosity is 55.3 pb^{-1}. The correction factor of 1.03 is taken into account in the computation of the signal and background events. The signatures of these events are a pair of high energy taus accompanied by two hadronic jets. The identification criteria of hadronically and leptonically decaying taus (the last are identified as either electrons or muons) are given in [7].

An automated procedure [8] is used to optimise the selection criteria. The optimised values of the cuts are rounded to 4 significant digits. At first, high multiplicity events are requested asking for a number of tracks ($N_{\rm gtk}$) greater than 5 and a number of calorimetric clusters ($N_{\rm cl}$) greater than 15. Then, cuts on the visible energy ($E_{\rm vis}$) and on the visible mass ($M_{\rm vis}$) of the event are applied. Finally, two taus are required (which means both hadronically and leptonically decaying taus). To avoid overlap with the Hee and $H\mu\mu$ channels, neither two electrons nor two muons are requested. Energy cuts are then applied on the two selected leptons, differently for the most or least energetic and depending on the lepton type ($E^{l,j}_{min}, l = e, \mu, \tau, j = 1, 2$). As isolation criteria for electrons and muons, the number of tracks in a 20^0 cone around the electron one, N^t_{20}, and the number of clusters between a 5^0 and a 20^0 cone, around a muon, $N^c_{20/5}$ are used. The selected hadronically decaying τ candidates have to fulfil some isolation requirements mainly dedicated to a rejection of the $Z/\gamma^* \to q\bar{q}$ and the $WW \to$ four jets background: a low number of tracks in a 10^0 cone around the τ (N^t_{10}) and a low ratio of the energies deposited between 10^0 and 30^0 and below 10^0 ($\frac{E_{30/10}}{E_{10}}$). To further reduce the background from radiative return to the Z events, a cut on $\sqrt{s'}$ is applied. Moreover, to reduce the contribution due to semileptonic decays of the W, a cut on the sum of the maximal energy of the two identified leptons and the missing energy of the event (Σ_{lm}) is applied. Once the two leptons are selected, the rest of the event is forced in two jets and the di–jet and di–tau invariant masses (M_{jj} and $M_{\tau\tau}$ respectively) are built. A kinematic fit is applied to improve the invariant mass resolution which uses the four–momentum conservation constraint. To reduce the background, each mass is required to be in the following mass interval (quite large according to the chosen mass points):

$$30 \text{ GeV} \le M_{jj},\, M_{\tau\tau} \le 120 \text{ GeV}$$
$$115 \text{ GeV} \le M_{jj} + M_{\tau\tau} \le 220 \text{ GeV}$$

All the cuts, except the ones on the number of tracks and clusters and on the invariant masses, are automatically optimised. The optimised cuts are shown in Table 31.

A total of 10.1 background events are expected after the selection, with 12 data observed. For a 87 GeV Higgs mass, an efficiency of 27.2% and 28.4% is found in the $\tau^+\tau^- b\bar{b}$ and $q\bar{q}\tau^+\tau^-$ channel respectively.

After the optimised selection, the final discriminating variable to distinguish signal from

cut		$\sqrt{s} = 183$ GeV
$\frac{E_{\rm vis}}{\sqrt{s}}$	$>$	0.4170
$\frac{E_{\rm vis}}{\sqrt{s}}$	$<$	1.0100
$\frac{M_{\rm vis}}{\sqrt{s}}$	$>$	0.4320
$\frac{M_{\rm vis}}{\sqrt{s}}$	$<$	1.2600
$\sqrt{\frac{s'}{s}}$	$>$	0.7150
Σ_{lm} (GeV)	$<$	50.1000
$E^{e,2}_{min}$ (GeV)	$>$	3.2200
$E^{\mu,2}_{min}$ (GeV)	$>$	3.0100
$E^{\tau,2}_{min}$ (GeV)	$>$	3.1500
$E^{e,1}_{min}$ (GeV)	$>$	3.1900
$E^{\mu,1}_{min}$ (GeV)	$>$	3.0200
$E^{\tau,1}_{min}$ (GeV)	$>$	5.9800
N^{t}_{20}	$<$	2.0900
$N^{c}_{20/5}$	$<$	4.0400
N^{t}_{10}	$<$	6.8400
$\frac{E_{30/10}}{E_{10}}$	$<$	0.2170

Table 31: The optimised sets of cuts for the tau–channels.

background is built. It is the statistical combination of the probability of b–content in the event (or not b–content in case of $q\bar{q}\tau^+\tau^-$) and the consistency with the mass hypothesis.

In case of the channel $\tau^+\tau^-b\bar{b}$, the probability to have b quarks ($\mathcal{P}_{\rm b}$) in the event is high, while the probability of not having b quarks $(1-\mathcal{P}_{\rm b})$ in the event is high for the $\tau^+\tau^-q\bar{q}$ channel. The probability of (non) b–content is computed having subtracted the two identified leptons from the event.

To account for the mass configuration, we define

$$\chi^2 = (\frac{\Sigma_M - M_{\tau\tau} - M_{jj}}{\sigma_\Sigma})^2 + (\frac{\delta_M - |M_{\tau\tau} - M_{jj}|}{\sigma_\delta})^2.$$

The variables Σ_M and δ_M are the sum and the difference of the two–invariant mass hypotheses (i.e. $m_{\rm H}$ and the Z boson mass). Their resolutions are $\sigma_\Sigma = 5$ GeV and $\sigma_\delta = 10$ GeV, respectively. The probability of the χ^2 having a value bigger than a given one is $\mathcal{P}_{\mathcal{M}}$.

Finally, the total probability is built as

$$\mathcal{P}_{\tau^+\tau^-b\bar{b}} = \mathcal{P}_{\rm b} * \mathcal{P}_{\mathcal{M}} * (1 - \ln(\mathcal{P}_{\rm b} * \mathcal{P}_{\mathcal{M}}))$$

for the $\tau^+\tau^-b\bar{b}$ channel and

$$\mathcal{P}_{q\bar{q}\tau^+\tau^-} = \mathcal{P}_{\mathcal{M}}$$

for the $q\bar{q}\tau^+\tau^-$ channel.

Given the two probabilities per event, the maxima among them ($\mathcal{P}$), weighted with the production cross section of the two channels, is taken as the final most discriminating variable:

$$\mathcal{P} = \frac{max(\sigma_{HZ\to\tau^+\tau^-b\bar{b}} * \mathcal{P}_{\tau^+\tau^-b\bar{b}}, \sigma_{HZ\to q\bar{q}\tau^+\tau^-} * \mathcal{P}_{q\bar{q}\tau^+\tau^-})}{\sigma_{\rm tot}}$$

where $\sigma_{HZ\to\tau^+\tau^-b\bar{b}}$, $\sigma_{HZ\to q\bar{q}\tau^+\tau^-}$ and $\sigma_{\rm tot}$ are the cross sections for the $HZ \to \tau^+\tau^-b\bar{b}$ and $HZ \to q\bar{q}\tau^+\tau^-$ processes and the sum of them respectively, This choice takes into account both the topological properties of the event and the cross section of the two processes. Since there is only one selection, there is only one background, each time reconstructed according to the right mass hypothesis, and two types of signal events. In Figures 60, 61, 62 the three probabilities $\mathcal{P}_{\rm b}$, $\mathcal{P}_{\mathcal{M}}$ and $\mathcal{P}$ are shown. Moreover, in Figure 63 the integral of the expected background events and the data as a function of the cuts on the final distribution $\mathcal{P}$ are shown. In Figure 64, the number of background expected events versus the signal efficiencies as a function of the cuts on the final distribution $\mathcal{P}$ are shown. In all the plots, the $HZ \to \tau^+\tau^-$ $b\bar{b}$ and $HZ \to \tau^+\tau^-$, $q\bar{q}$ channel are summed together. All the plots refer to a Higgs boson of $m_{\rm H} = 87$ GeV.

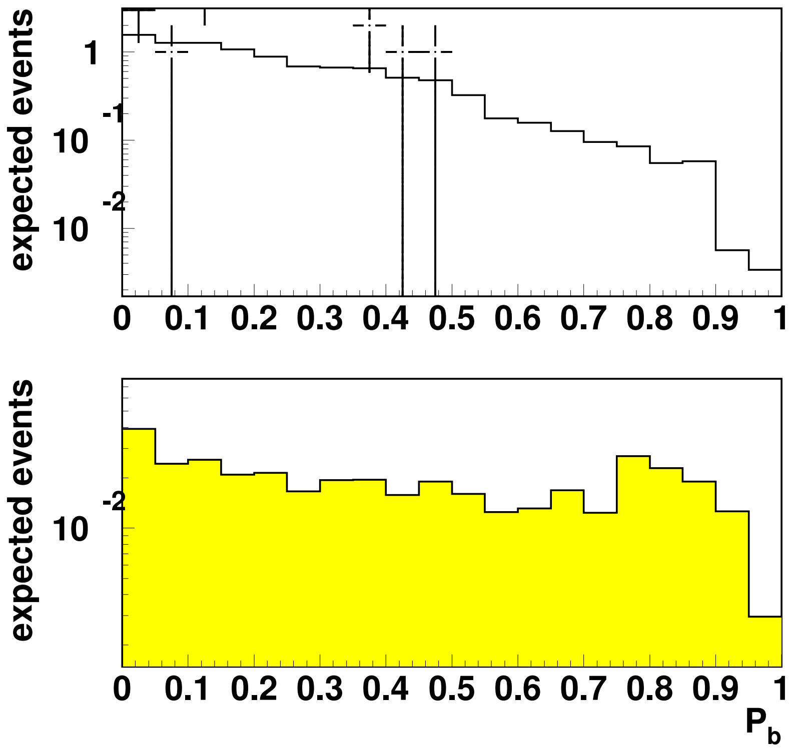

Figure 60: The $\mathcal{P}_{\mathrm{b}}$ distribution is shown for the background (upper plot, solid line), the data (upper plot, dots), and a Higgs signal of 87 GeV(lower plot). The $\tau^+\tau^-\mathrm{b}\bar{\mathrm{b}}$ and $\mathrm{q}\bar{\mathrm{q}}\tau^+\tau^-$ channels are summed together.

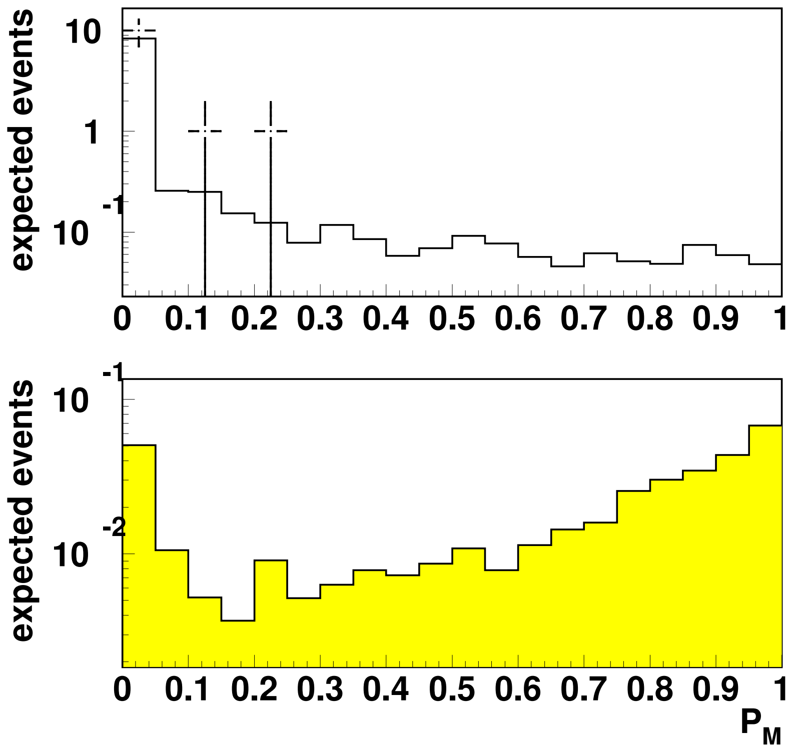

Figure 61: The $\mathcal{P}_{\mathcal{M}}$ distribution is shown for the background (upper plot, solid line), the data (upper plot, dots), and a Higgs signal of 87 GeV(lower plot). The $\tau^+\tau^-\mathrm{b}\bar{\mathrm{b}}$ and $\mathrm{q}\bar{\mathrm{q}}\tau^+\tau^-$ channels are summed together.

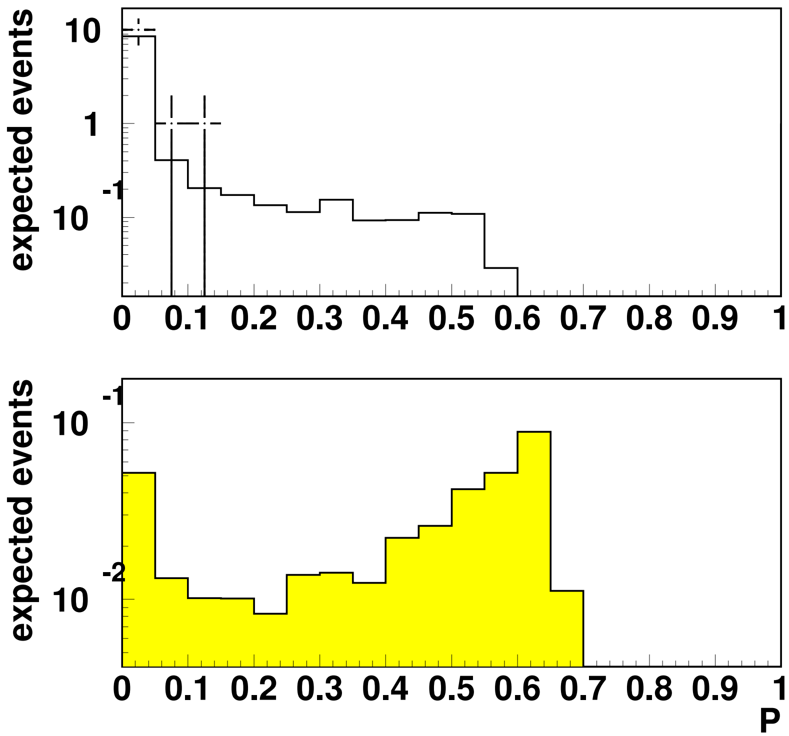

Figure 62: The $\mathcal{P}$ distribution is shown for the background (upper plot, solid line), the data (upper plot, dots), and a Higgs signal of 87 GeV(lower plot). The $\tau^+\tau^-\mathrm{b\bar{b}}$ and $\mathrm{q\bar{q}}\tau^+\tau^-$ channels are summed together.

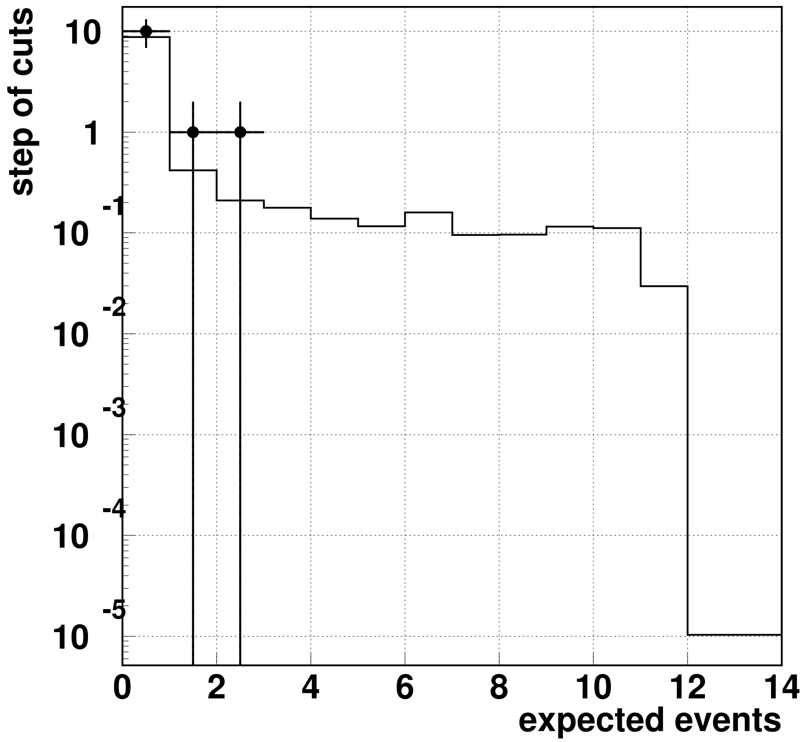

Figure 63: Integral of the expected background events (solid line) and the data (dots) as a function of the cuts on the final distribution $\mathcal{P}$ for a Higgs boson of 87 GeV.

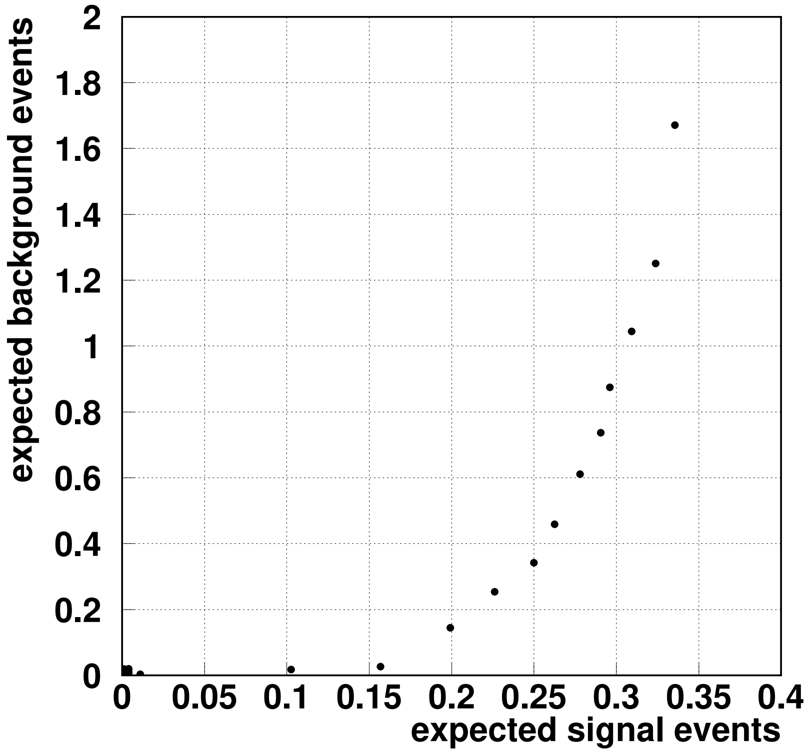

Figure 64: Number of expected background events and corresponding signal events varying the cuts on the final distribution $\mathcal{P}$ for a Higgs boson of 87 GeV.

6.5 Search in $\tau\tau$ channels using neural network.

Analysis is made in two steps: at first selection suppresses the bulk of background, and then a neural network is applied to further distinguish between signal and background. A feed-forward neural network with one layer of input nodes, one layer of hidden nodes and one output node is used.

Common preselection for both channels:
1) Event contains two jets and two leptons with energy more than $5Gev$.
2) Number of clusters is at least 20 and number of tracks is at least 4.
3) Number of scintillators in time is more than 2.
4) Energy in BGO and HCAL is more than 30% of visible energy.
5) Visible mass is more than $60Gev$.
6) Thrust of an event is less than 0.95.
7) Energy in luminosity monitor plus ALR is less than $10Gev$.
8) $6Gev < E_{miss} < 50Gev$.
9) If τ decays hadronically then
a) Number of clusters inside cone 10^0 around τ direction is not more than 6;
b) Number of tracks in cone 30^0 is not more than 3;
c) Ratio of energies in cones $10^0 - 30^0$ and $0^0 - 10^0$ is less than 0.3.
10) Each τ candidate has charge one, and two charges have an opposite sign.
11) Angle between each τ and closest jet is more than 0.3 rad. Sum of these angles is more than 1 rad.

6.5.1 The HZ $\rightarrow \tau^+\tau^- q\bar{q}$ channel.

Selection for this channel:
1) Energy of more energetic τ is less than $60Gev$ and of less energetic τ is less than 40 Gev.
2) $35Gev < E_{jet1} < 86Gev$ ($jet1$ is more energetic jet).
3) $M_{\tau\tau} < 90Gev$.
4) $66Gev < M_{jj} < 115Gev$.
5) Angle between two leptons is greater than 1.8 rad, angle between two jets is greater than 2 rad.

Energies of jets are fitted to have a mass of two jets equal to Z mass (in events passing the selection). After the fit additional cuts are applied:
1) $-15Gev < E^f_{j1} - E_{j1} < 25Gev$ (E^f_j - energy of jet after the fit, E_j - energy before the fit).
2) $-12Gev < E^f_{j2} - E_{j2} < 12Gev$.
3) $0.8 < E^f_{j2}/E_{j2} < 1.35$.
4) Recoil mass to two jets after the fit is greater than $40Gev$.
5) Angle between recoil momentum to two jets after the fit and a plane of $\tau\tau$ is less than 1 rad.
6) $(\pi - \theta_{\tau\tau})/(\pi - 2 \cdot \arctan(M^f_r/P^f_r))$ is less than 2 rad (where $\theta_{\tau\tau}$ is an angle between measured τ directions, M^f_r - recoil mass to two jets after the fit, P^f_r - recoil momentum to

two jets after the fit).

Efficiency of selection versus Higgs mass is shown in figure 65a.

A neural network has 10 input nodes and 18 hidden nodes. Input values:
1) Measured energy of $\tau 1$ decay products.
2) Measured energy of $\tau 2$ decay products.
3) Visible mass of $\tau\tau$ decay products.
4) Missing energy.
5) Difference between measured and fitted energy of $jet1$.
6) $(E_{cone1} + E_{cone2})/(E_{\tau 1} + E_{\tau 2})$, where E_{cone} is an energy between cones of 10^0 and 30^0 around τ direction.
7) Mass of two jets before fit.
8) $\sqrt{2 \cdot E_r \cdot E_{cm} - {M_r}^2}$, where E_r is recoil energy to two jets and M_r - recoil mass to two jets before fit.
9) Angle between $\tau 1$ and closest jet.
10) Angle between $\tau 2$ and closest jet.

Efficiency of neural network (fraction of signal events with NN output more than 0.5) versus Higgs mass is shown in figure 65b.

Figure 66 shows expected NN output for background ($q\bar{q}$, WW and ZZ) events (open histogram) and signal events (hatched histogram) for mass of Higgs $83 Gev$ (a) and $87 Gev$ (b).

Number of expected background events after cuts is 1.3 ± 0.1. No events are found in data.

6.5.2 The HZ $\rightarrow b\bar{b}\tau^+\tau^-$ channel.

Selection for this channel:
1) Energy of more energetic τ is less than $70 Gev$ and of less energetic τ is less than 42 Gev.
3) $32 Gev < E_{jet1} < 76 Gev$, $15 Gev < E_{jet2} < 56 Gev$ ($jet1$ is more energetic jet).
4) $5 Gev < M_{jet1} < 52 Gev$, $4 Gev < M_{jet2} < 33 Gev$.
5) $10 Gev < M_{\tau\tau} < 100 Gev$.
6) $M_{jj} < 115 Gev$.
7) Angle between two leptons and angle between two jets are greater than 1.8 rad.
8) Angle between two leptons in XY-plane is greater than 1.7 rad.
9) Recoil momentum to two jets is less than $59 Gev$.
10) $60 Gev < M_r < 120 Gev$ (M_r - recoil mass to two jets).

Energies of jets are fitted to have a recoil mass to two jets equal to Z mass. After the fit additional cuts are applied:
1) $-20 Gev < E^f_{j1} - E_{j1} < 20 Gev$ (E^f_j - energy of jet after the fit, E_j - energy before the fit).
2) $0.75 < E^f_{j1}/E_{j1} < 1.5$.
3) $-12 Gev < E^f_{j2} - E_{j2} < 12 Gev$.
4) Recoil momentum to two jets after the fit is less than $50 Gev$.
5) Recoil mass to two jets after the fit is greater than $90 Gev$.

6) Angle between recoil momentum to two jets after the fit and a plane of $\tau\tau$ is less than 1 rad.
7) $(\pi - \theta_{\tau\tau})/(\pi - 2 \cdot \arctan(M^f_r/P^f_r))$ is less than 1.6 rad (where $\theta_{\tau\tau}$ is an angle between measured τ directions, M^f_r - recoil mass to two jets after the fit, P^f_r - recoil momentum to two jets after the fit).
8) $(\pi - \theta_{jj})/(\pi - 2 \cdot \arctan(M^f_{jj}/P^f_{jj}))$ is less than 1.3 rad (where θ_{jj} is an angle between jets directions, M^f_{jj} - mass of two jets after the fit, P^f_{jj} - momentum of two jets after the fit).

Efficiency of selection versus Higgs mass is shown in figure 65c.

A neural network has 8 input nodes and 16 hidden nodes. Input values:
1) Measured energy of $\tau 1$ decay products.
2) Visible mass of $\tau\tau$ decay products.
3) $(\pi - \theta_{jj})/(\pi - 2 \cdot \arctan(M^f_{jj}/P^f_{jj}))$
4) $(E_{cone1} + E_{cone2})/(E_{\tau 1} + E_{\tau 2})$, where E_{cone} is an energy between cones of 10^0 and 30^0 around τ direction.
5) Recoil mass to two jets before fit.
6) $\sqrt{2 \cdot (E_{jet1} + E_{jet2}) \cdot E_{cm} - {M_{jj}}^2}$
7) Difference between measured and fitted energy of $jet1$.
8) B-tag.

Efficiency of neural network (fraction of signal events with NN output more than 0.5) versus Higgs mass is shown in figure 65d.

Figure 66 shows expected NN output for background ($q\bar{q}$, WW and ZZ) events (open histogram) and signal events (hatched histogram) for mass of Higgs $83 Gev$ (c) and $87 Gev$ (d).

Number of expected background events after cuts is 1.5 ± 0.1. No events are found in data.

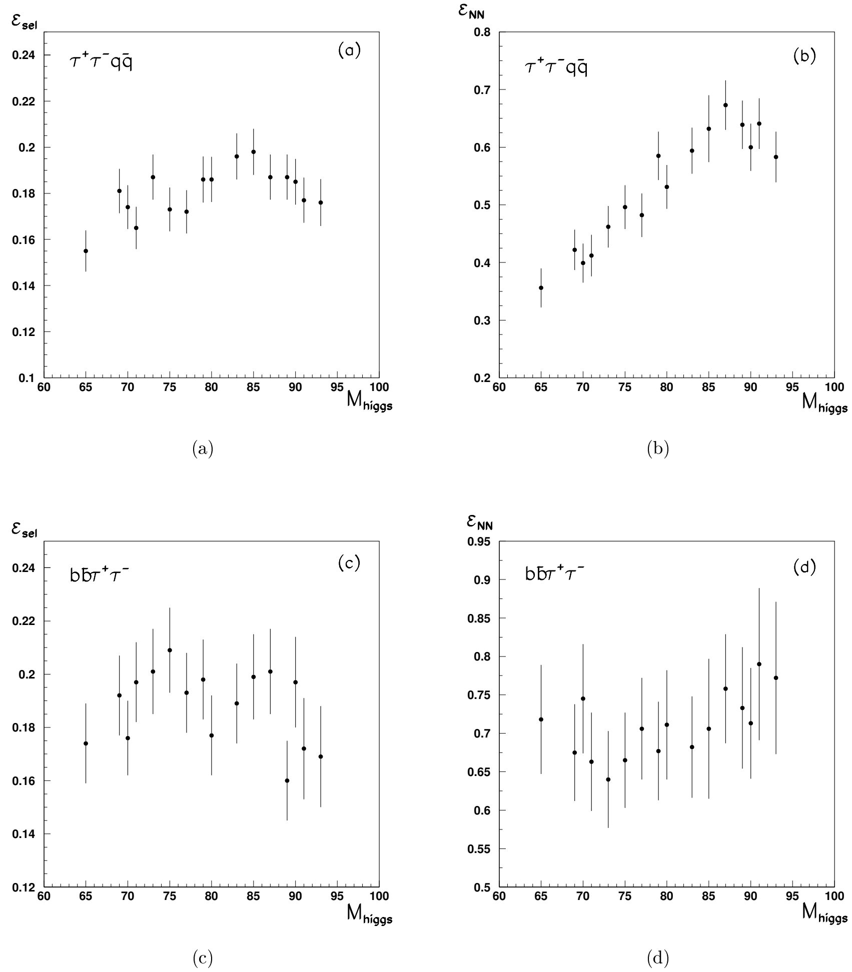

(a) (b) (c) (d)

Figure 65: Efficiency: of selection for $\tau^+\tau^-q\bar{q}$ (a), of neural network for $\tau^+\tau^-q\bar{q}$ (b), of selection for $b\bar{b}\tau^+\tau^-$ (c), of neural network for $b\bar{b}\tau^+\tau^-$ (d).

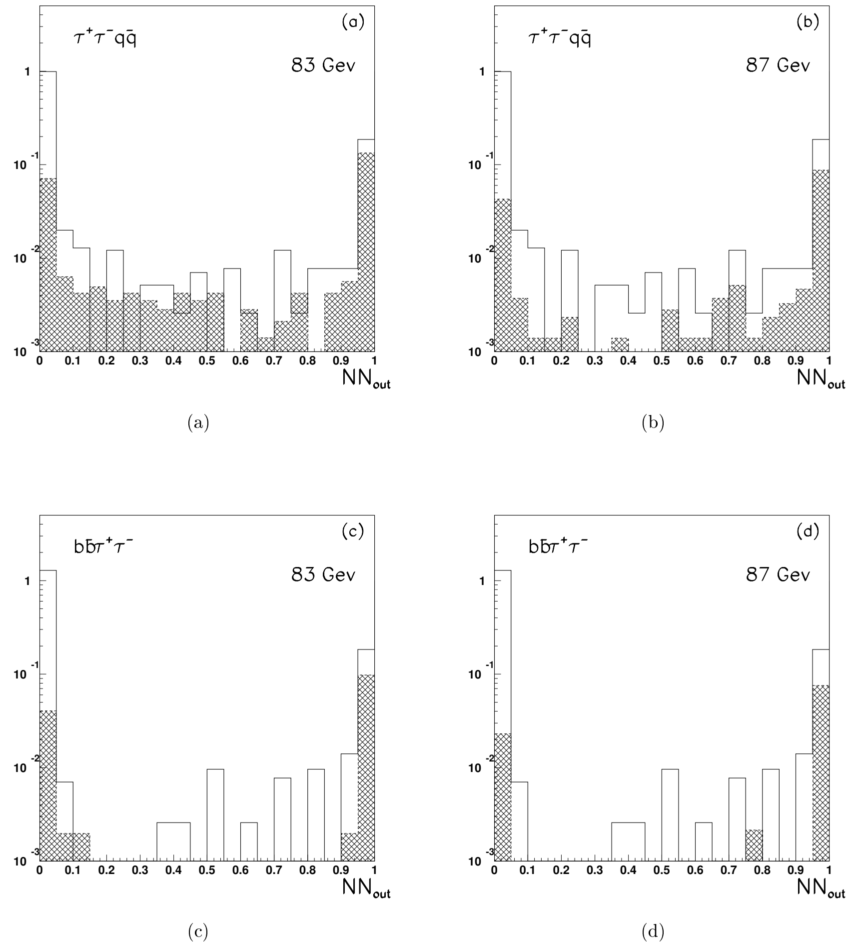

(a) (b) (c) (d)

Figure 66: Neural network output: for $\tau^+\tau^-q\bar{q}$ $M_{higgs} = 83Gev$ (a), for $\tau^+\tau^-q\bar{q}$ $M_{higgs} = 87Gev$ (b), for $b\bar{b}\tau^+\tau^-$ $M_{higgs} = 83Gev$ (c), for $b\bar{b}\tau^+\tau^-$ $M_{higgs} = 87Gev$ (d). Open histogram - background, hatched histogram - signal.

7 Combination of results and Higgs mass limit

7.1 Combined results I

No statistically significant excess is observed in the mass range under investigation by all the analyses described in the note. To make a quantitative conclusions the neural network analyses for the H$q\bar{q}$ (Section 3.3), H$\nu\bar{\nu}$ (Section 5.1), He^+e^- and H$\mu^+\mu^-$ channels (Section 6.3) and the optimised cuts analyses for the HZ $\rightarrow \tau^+\tau^-$ $q\bar{q}$ and HZ $\rightarrow q\bar{q}\,\tau^+\tau^-$ channels (Section 6.2) are used in this section.

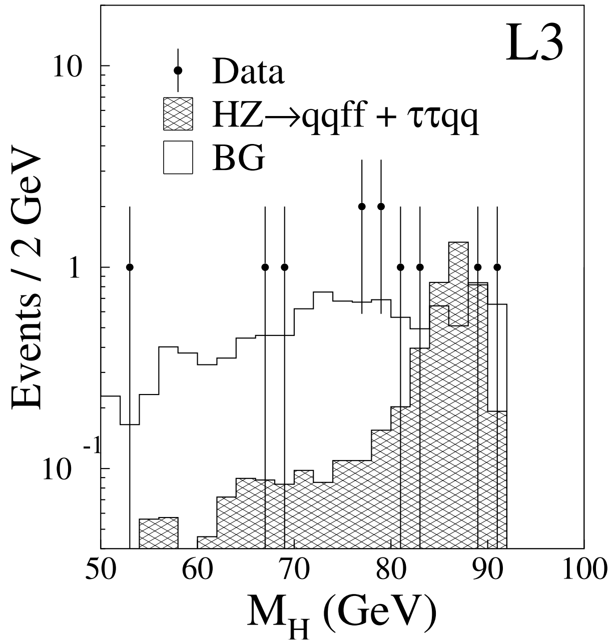

Figure 67: The reconstructed Higgs mass distribution of the 11 most significant candidates selected in the data with $NN_{\mathrm{out}} > 0.7$, 0.5 and 0.1 for the $q\bar{q}q\bar{q}$, $q\bar{q}\nu\bar{\nu}$ and $q\bar{q}\ell^+\ell^-$ selections, respectively, and with $D_{M_{\mathrm{H}}} > -3$ for the $b\bar{b}\tau^+\tau^-$ and $\tau^+\tau^-q\bar{q}$ selections. The corresponding distributions for an 87 GeV Higgs signal and for the background are also shown for comparison.

For the illustration purposes the reconstructed Higgs mass distribution of the 11 most significant candidates (selected in with the following cuts: $NN_{\mathrm{out}} > 0.7$, 0.5 and 0.1 for the $q\bar{q}q\bar{q}$, $q\bar{q}\nu\bar{\nu}$ and $q\bar{q}\ell^+\ell^-$ selections, respectively, and with $D_{M_{\mathrm{H}}} > -3$ for the $b\bar{b}\tau^+\tau^-$ and $\tau^+\tau^-q\bar{q}$ selections) is shown in Figure 67, where the corresponding distributions for a 87 GeV Higgs signal and for the background are also shown for comparison. A total of 10.6 events are expected from background processes.

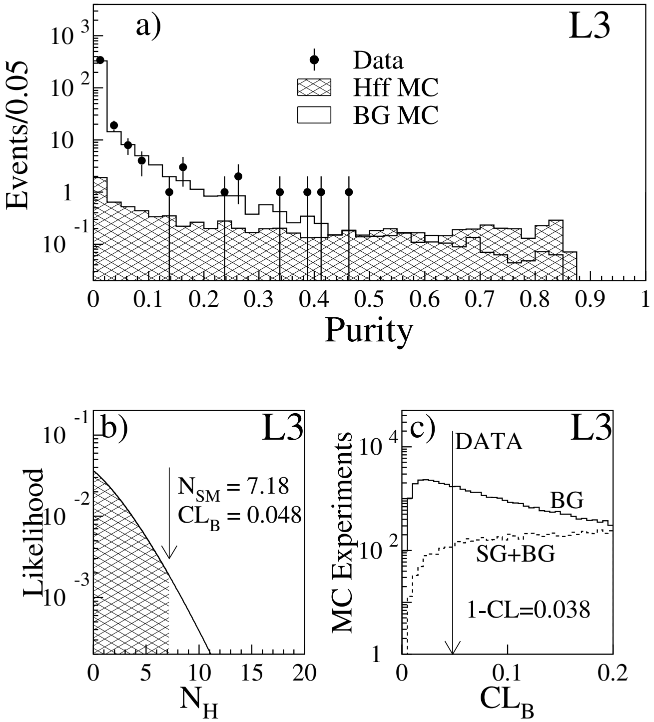

Figure 68: (a) The purity variable spectrum for 87 Higgs mass hypotheses. All search channels are combined. (b) Bayesian likelihood as a function of number of 87 GeV Higgs events. (c) Spectra of Bayesian probabilities for background only (solid line) and signal and background (dashed line) hypotheses.

The likelihood as a function of the number of expected signal events is determined from the distributions of the purity variable for the H$q\bar{q}$, H$\nu\bar{\nu}$, He^+e^- and H$\mu^+\mu^-$. For the $\tau^+\tau^-q\bar{q}$ channels the optimised cuts analyses were used. An example of the combined purity distribution for the 87 GeV Higgs mass hypothesis is presented in Figure 68a. The likelihood is constructed using Poisson statistics for the number of observed data events, $N_{i,k}$:

$$\mathcal{L}(\mu_{\rm H}) = \prod_{k=1}^{n_{\rm ch}} \prod_{i=1}^{n_{\rm bn}^k} \frac{e^{-(\mu_{{\rm H},i,k}+\mu_{{\rm b},i,k})}(\mu_{{\rm H},i,k}+\mu_{{\rm b},i,k})^{N_{i,k}}}{N_{i,k}!}, \quad (14)$$

where the product is taken over all search channels ($k = (1, n_{\rm ch})$) and all bins ($i = (1, n_{\rm bn})$). The background shapes and normalisations are fixed to the Monte Carlo prediction ($\mu_{{\rm b},i,k}$). The individual signal expectations, ($\mu_{{\rm H},i,k}$), are proportional to the total number of signal events, $\mu_{\rm H}$, corresponding branching fractions, $\mathcal{B}_k$, and efficiencies, $\epsilon_{i,k}$. In the calculation of the likelihood the lower cut on purity of 0.1 was applied aiming to save computer time (it goes up dramatically with the number of data events). The binning is chosen to be 20 bins for all the six distributions and smoothing of the signal and background spectra are applied to decrease statistical fluctuations in the signal-to-background ratio from one bin to another. An example of the likelihood as a function of signal events is shown in Figure 68b.

As no indication for the signal is observed the exclusion confidence level (CL) is calculated for the various Higgs mass hypotheses: with 0.2 GeV step from 60 to 75 GeV and with 0.1 GeV step from 75 to 92 GeV.

The signal probability density function is then constructed using Bayesian statistics:

$$\mathrm{P}(\mu_{\rm H})\mathrm{d}\mu_{\rm H} = \frac{\mathcal{L}(\mu_{\rm H})\mathrm{d}\mu_{\rm H}}{\int \mathcal{L}(\mu_{\rm H})\mathrm{d}\mu_{\rm H}} \quad (15)$$

For the CL calculations the frequentistis corrections are applied to Bayesian probability. This is done by generating 50000 MC outcomes for two hypothesis: 1) both the signal and background and 2) the background only (the corresponding spectra are shown in Figure 68c). The systematic errors on the signal (4% Gaussian) and background expectations (bin-by-bin Poissonian corresponding to the Monte-Carlo statistics) are taken into account during the generation of the Monte Carlo experiments.

The exclusion confidence level (1-CL) for the SM Higgs signal is shown in Figure 69 as a function of the Higgs boson mass together with the median of the (1-CL) over a sample of Monte Carlo experiments. The probability that, in absence of a signal, the actual CL will be either higher or lower than its median is 50%, by definition. The Higgs mass value at which the median confidence level crosses the 95% is 86.7 GeV. The average of the CL over a sample of Monte Carlo experiments crosses the 95% line at 85.1 GeV.

The non-regular behaviour of the actual and the median lines (especially at low values of 1-CL) reflects limited statistics of the Monte Carlo experiments for the hypothesis of both the signal and background. For example, if the 1-CL value is estimated to be 10^{-3}, the relative error can be roughly evaluated from the fluctuations of the number of MC outcomes $\mathrm{N_{outcomes}} = 50000 \cdot 10^{-3} \cdot 0.5 = 25$. In this example the relative error is 20%.

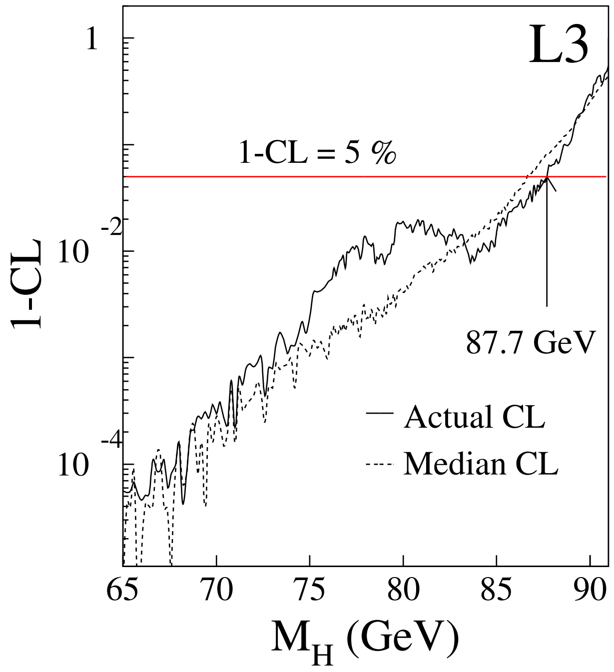

Figure 69: The actual 1-CL exclusion (solid line) and the median 1-CL line (dashed line) as a functions of the Higgs boson mass.

In order to reduce this error the neighbouring mass points can be used to make interpolation, as the generated MC experiments are not statistically correlated for any pair of mass points. The result of this interpolation is presented in Figure 70 for the number of signal events excluded at 95% CL and for the actual 1-CL exclusion. It reduces the actual Higgs mass limit by 0.1 GeV.

The lower limit on the Higgs boson mass is

$$M_{\rm H} > 87.6 \text{ GeV} \quad \text{at } 95\% \text{ CL}.$$

The probability to obtain a higher limit is estimated to be 34%.

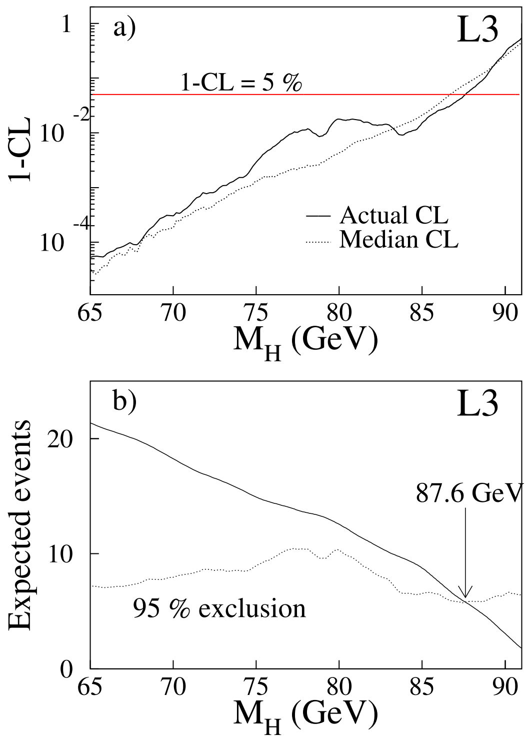

Figure 70: (a) The actual 1-CL exclusion (solid line) and the median 1-CL line (dashed line) as a functions of the Higgs boson mass. (b) The number of expected Higgs signal events (solid line) and the number of signal events excluded at 95% confidence level (dashed line) as functions of the Higgs boson mass.

7.2 Combination of the results II

The method described in [5] is used to derive the confidence levels.

In the Figures 71, 72, 73 and 74, the $1 - C.L.$, $< 1 - C.L. >$ and CL_b are shown for the four jet, missing energy and leptonic channels as a function of $m_{\rm H}$. The lower is the 1-C.L. or $< 1 - C.L. >$, the better is the result. Moreover, CL_b is the probability that to have a smaller observation for the expected background (a number around $\sim 50\%$ would be the optimum). A lower cut on the signal–over–background ratio of .15 is applied.

The set of the analyses with the the higher average [1)] is:

Hqq	H$\nu\nu$	Hee	H$\mu\mu$	H$\tau\tau$	$\tau\tau$qq
NN2	NN	NN	NN	Sequential Cuts	Sequential Cuts

In the Figure 75, the number of expected signal events (top), background events (middle) and data (bottom) are shown for this set. To minimise the impact of statistical flucuaction on the Montecarlo distributions, all the Neural Network inputs are smoothed. A lower cut on the signal–over–background ratio of .10 is applied.

In the Figures 76, $1 - C.L.$ and the $< 1 - C.L. >$ are shown for the chosen final set of analyses.

When the confidence levels cross the 95%, the following mass limits are obtained:

$m_{\rm H}$ (GeV)	$CL_b(m_{\rm H}^{limit})$	$< m_{\rm H} >$ (GeV)	$\overline{m_{\rm H}}$ (GeV)
87.8	36 %	85.6	86.9

The probability is computed at the measured mass limit.

Systematical Errors: The systematic errors on the signal and background expectations are taken into account during the generation of the Monte Carlo experiments. In each trial experiment, both the total number of signal and background events is smeared according to a gaussian distribution with standard deviation 4% for signal and 10% for the background, and the expected events bin–by–bin are extracted according to a Poisson distribution in the hypothesis that there are ~ 150 MC events for a signal one, and ~ 50 MC events for a background event. The nominal expected signal and background are then used to calculate the confidence level. The combined effect is dominated by the error on the background. The final results are:

$m_{\rm H}$ (GeV)	$CL_b(m_{\rm H}^{limit})$	$< m_{\rm H} >$ (GeV)	$\overline{m_{\rm H}}$ (GeV)
87.6	35 %	85.0	86.8

[1)] In case of the tau channel, the one specifically dedicated to the SM Higgs search is taken

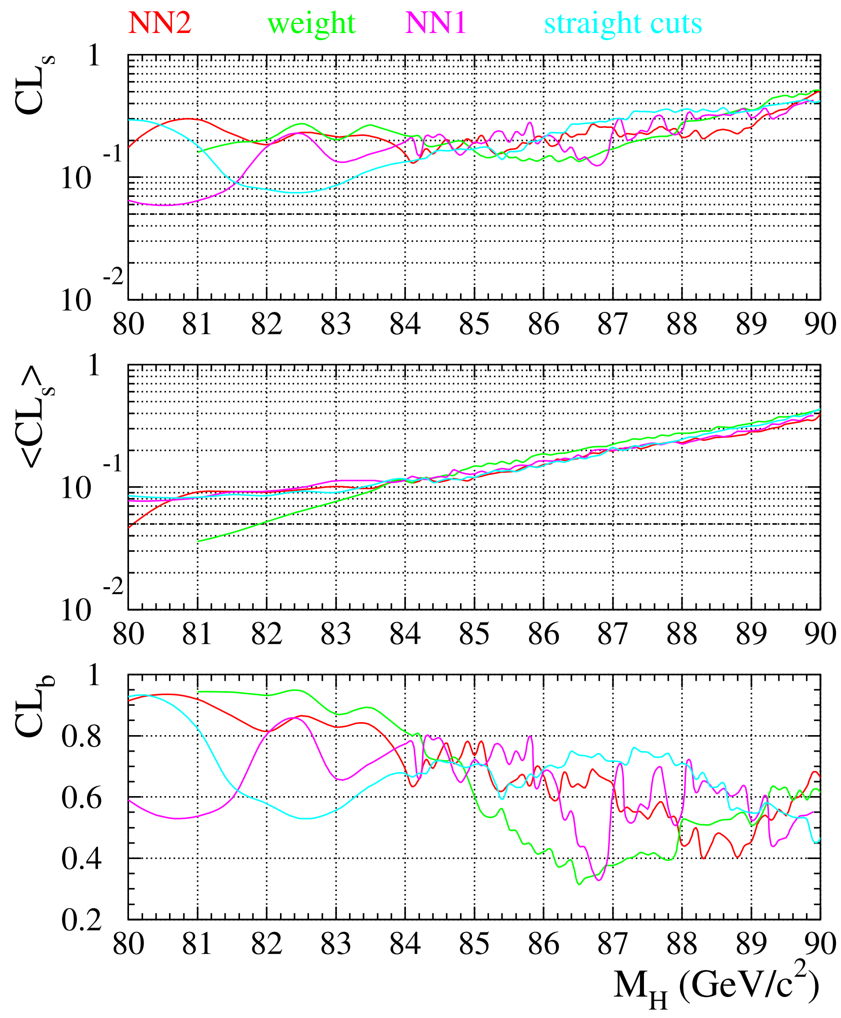

Figure 71: $CL_s = 1 - C.L.$, $< CL_s > = < 1 - C.L. >$, CL_b for the three four–jet analyses.

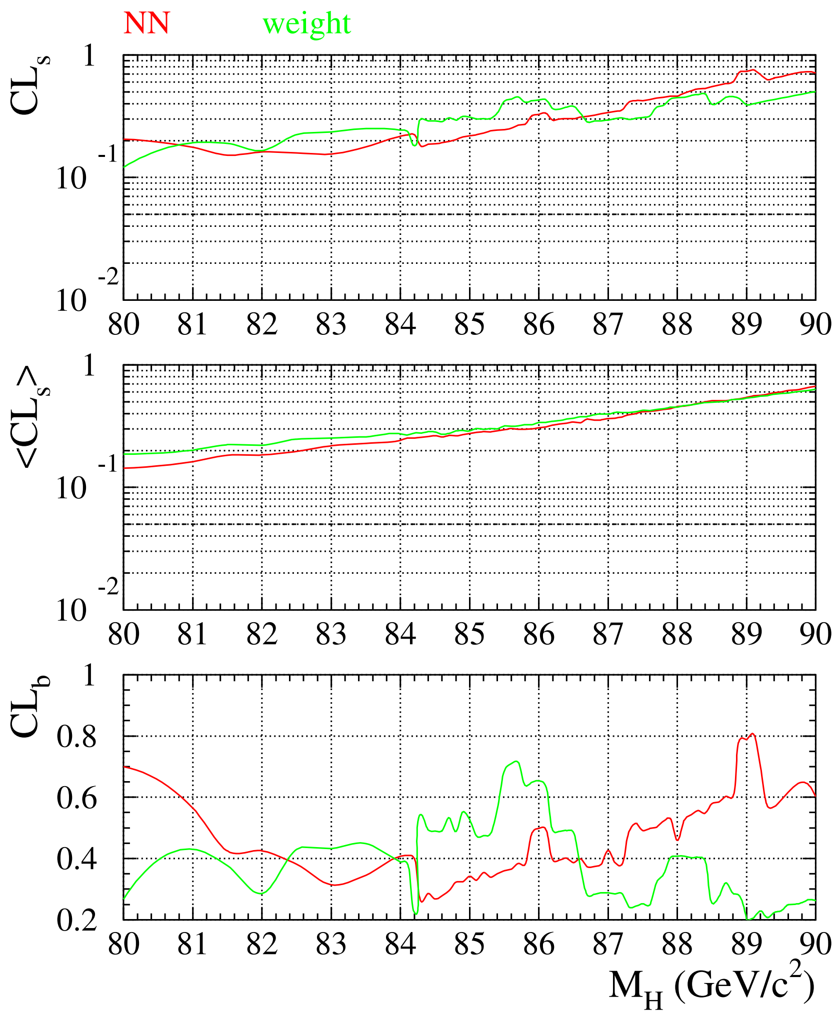

Figure 72: $CL_s = 1 - C.L.$, $< CL_s > = < 1 - C.L. >$, CL_b for the two missing energy analyses.

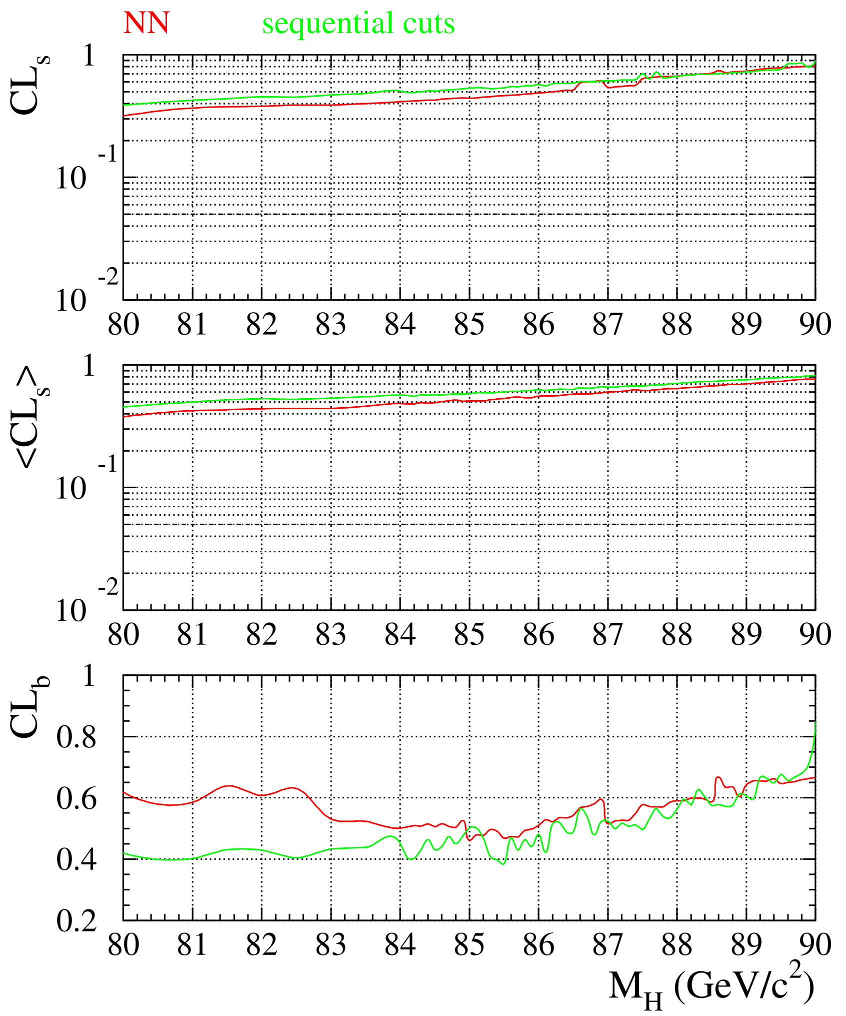

Figure 73: $CL_s = 1 - C.L.$, $< CL_s > = < 1 - C.L. >$, CL_b for the two leptonic analyses.

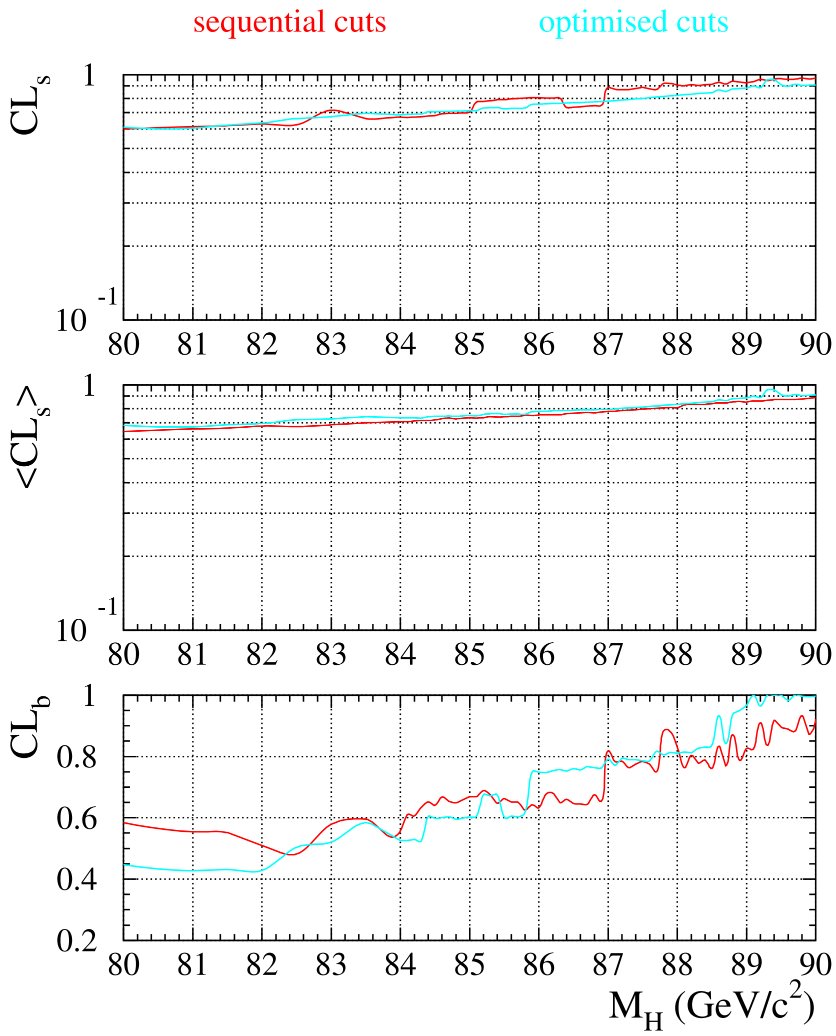

Figure 74: $CL_s = 1 - C.L.$, $< CL_s > = < 1 - C.L. >$, CL_b for the two tau–channel analyses.

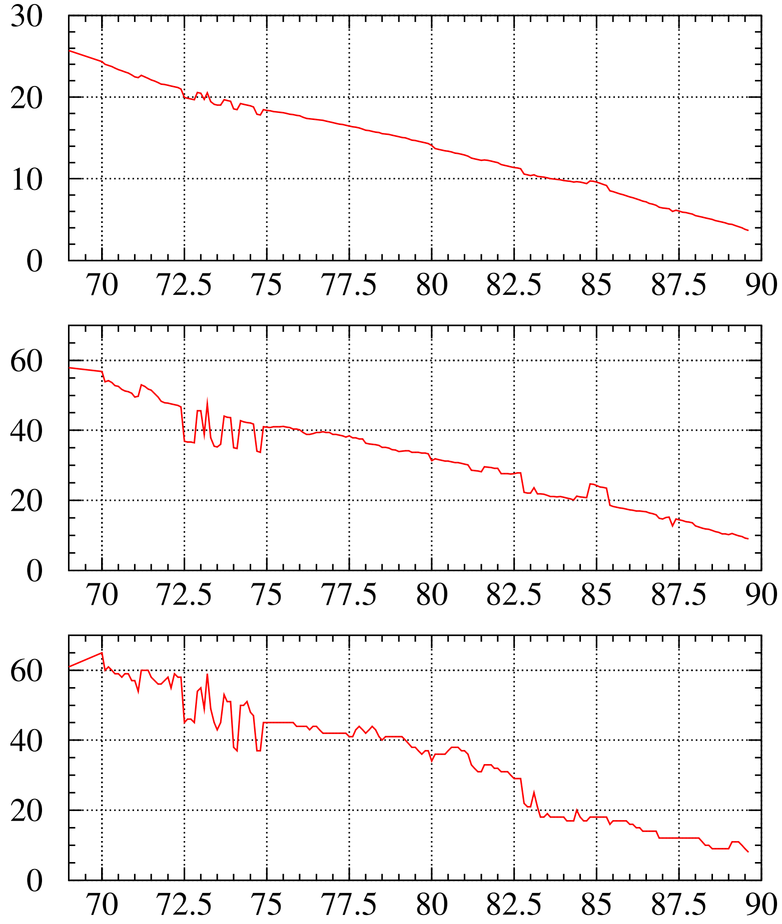

Figure 75: Number of expected signal events (top), background events (middle) and data (bottom) are shown for the chosen final set of analyses.

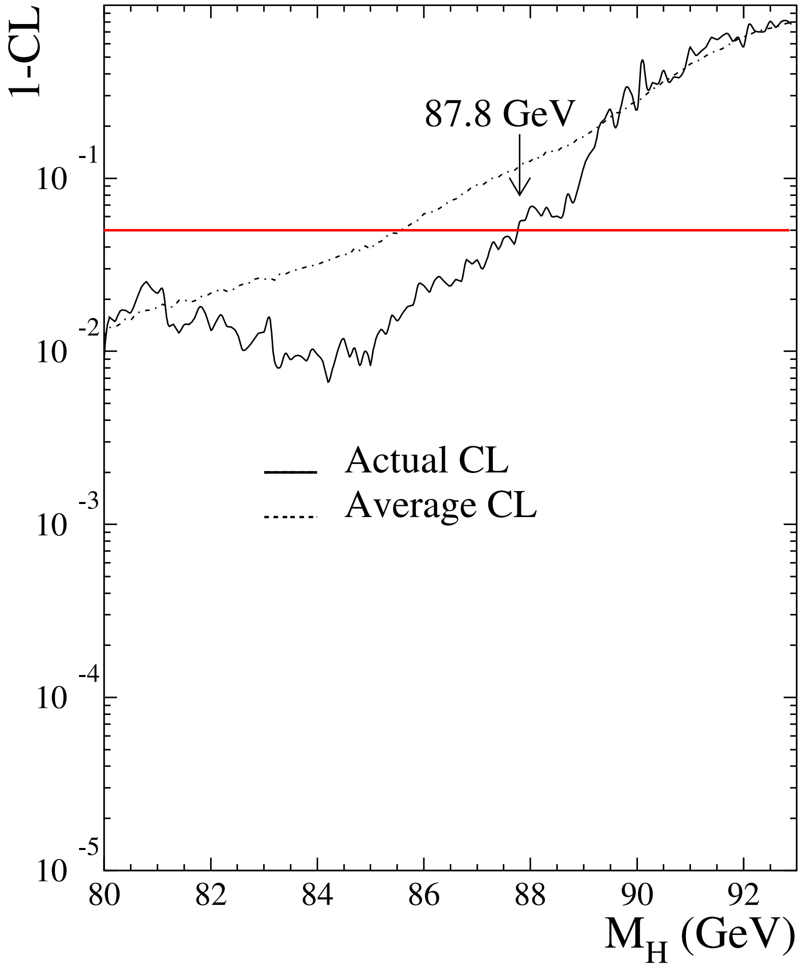

Figure 76: $CL_s = 1 - C.L.$ and $< CL_s > = < 1 - C.L. >$ for the chosen set of analyses.

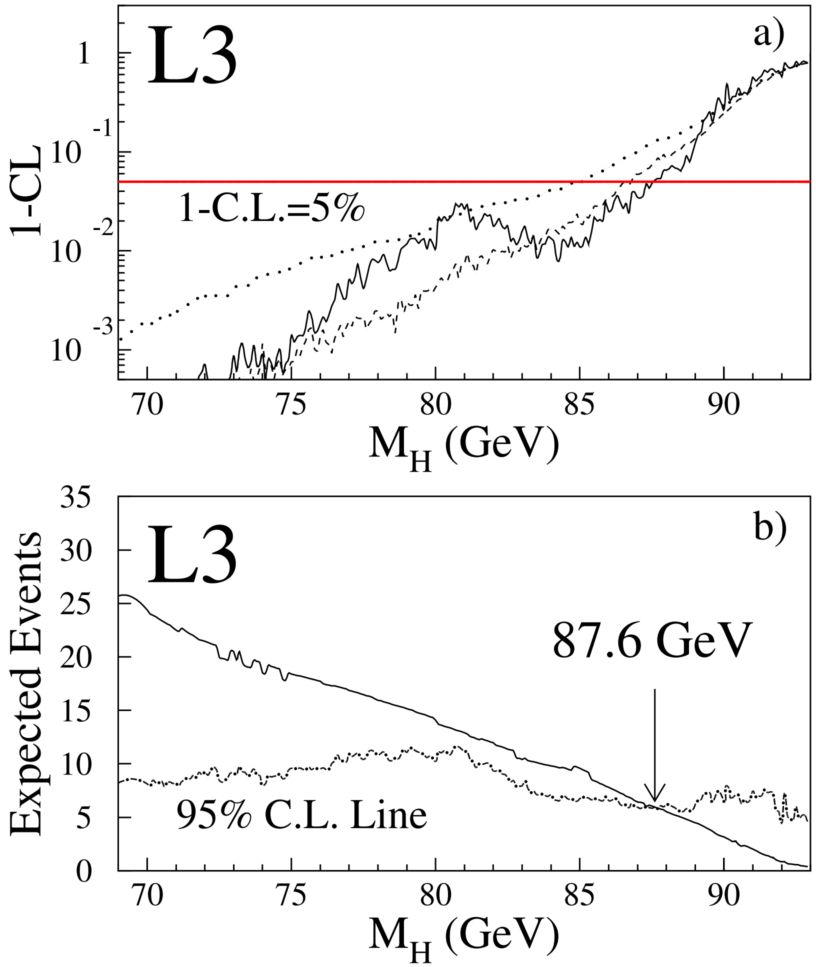

Figure 77: a) $CL_s = 1 - C.L.$, $< CL_s > = < 1 - C.L. >$ and $\overline{1 - C.L.}$, b) expected number of signal events and 95% C.L. line for the chosen set of analyses.

In the Figures 77, $1 - C.L.$, the $< 1 - C.L. >$ and the $\overline{1 - C.L.}$ are shown for the chosen final set of analyses having applied the systematic computation.

A smoothing is then applied to minimise the impact of the statistical fluctuactions, due to the actual number of MC events used in the analysis and the number of gedanden experiments used in the derivation of the CL. The comparison with the derived curved and the smoothed is in Figure 78, and the final plot is in Figure 79.

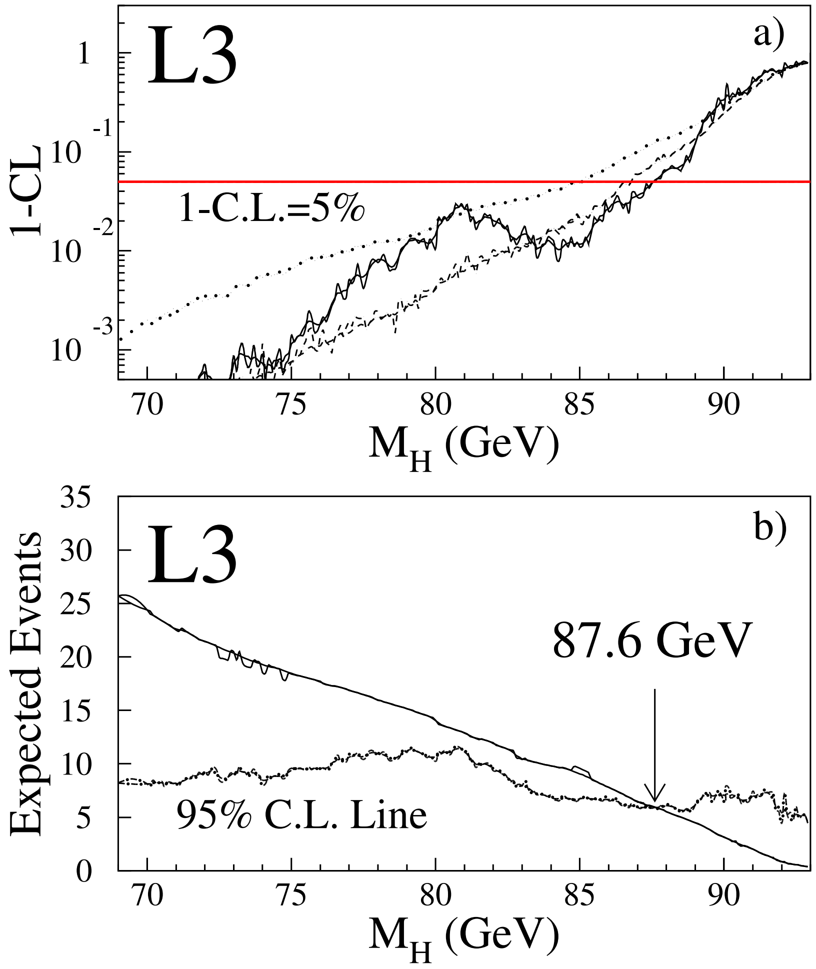

Figure 78: a) $CL_s = 1 - C.L.$, $< CL_s > = < 1 - C.L. >$ and $\overline{1 - C.L.}$ b) expected number of signal events and 95% C.L. line for the chosen set of analyses. Comparison of smoothed and no–smoothed curves.

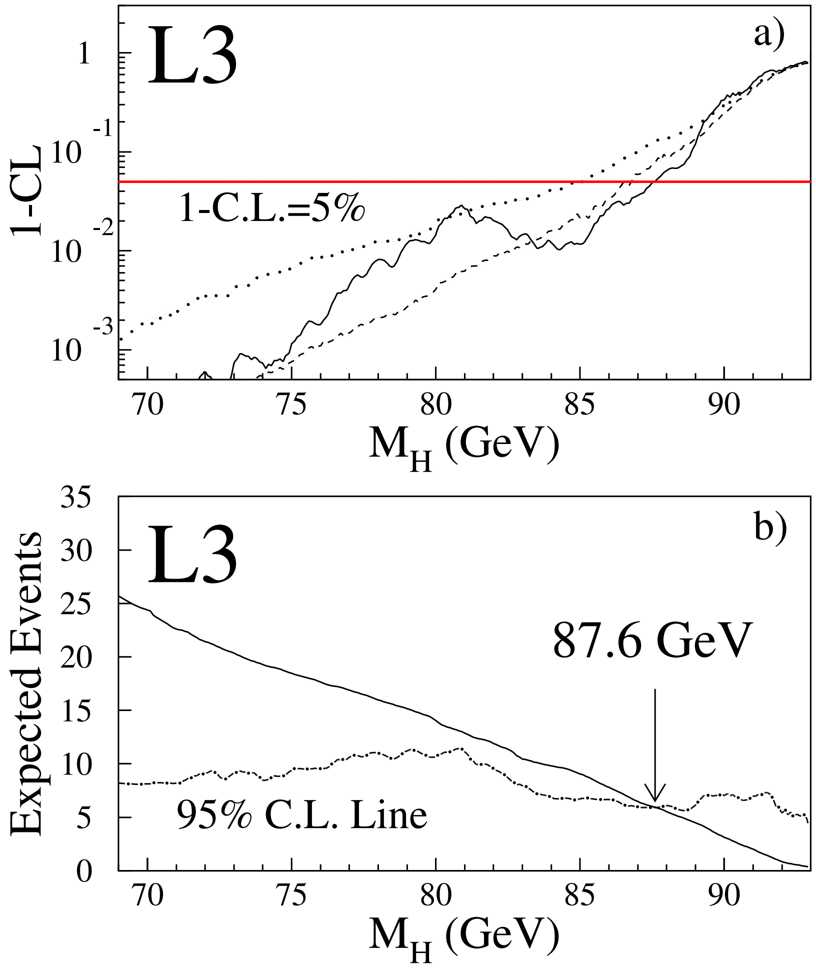

Figure 79: a) $CL_s = 1 - C.L.$, $< CL_s > = < 1 - C.L. >$ and $\overline{1 - C.L.}$ b) expected number of signal events and 95% C.L. line for the chosen set of analyses after smoothing

7.3 Combined results III

Another computation of the confidence levels and mass limits was performed as a cross check of the results presented in Sections 7.1 and 7.2. The method of confidence level and mass limit computation is described in [2] with only one main computational difference. The final distributions of all the search channels ($\mathrm{Hq\bar{q}}, \mathrm{H}\nu\bar{\nu}, \mathrm{H}\ell^+\ell^-$ and $\mathrm{H}\tau^+\tau^-$) are combined into one histogram with bins of signal-to-background (S/B) by computing the S/B ratio in each bin of a given channel's final distribution. It is then the S/B distributions for MC signal, background and observed data that are used to calculate the likelihood. The systematic corrections described in Section 5 of [6] have been applied *before* this rebinning of the final distributions, however.

The $\mathrm{Hq\bar{q}}$ analysis described in Section 3.2 was found to have an average confidence level, $< 1 - CL >$, equivalent (within the precision of the computation) to the $< 1 - CL >$ for the $\mathrm{Hq\bar{q}}$ analysis described in Section 3.3. This can be seen in Fig. 80. The final 95% CL lower limit on the Higgs mass is calculated using the analyses listed in the table in Section 7.2 with the exception of $\mathrm{Hq\bar{q}}$, where the optimised cuts analysis of Section 3.2 was used.

The confidence levels shown in Fig. 81 cross the 95% level at the mass points listed in Table 32.

m_{H}(GeV)	$CL_b(m_{\mathrm{H}}^{limit})$ (%)	$< m_{\mathrm{H}} >$ (GeV)	$\overline{m_{\mathrm{H}}}$ (GeV)
87.3	39%	84.9	86.6

Table 32: From left to right: observed 95% lower limit on m_{H}; probability of observing a larger confidence level at limit; lower limit on m_{H} at 95% crossing of average CL; 95% crossing of median CL.

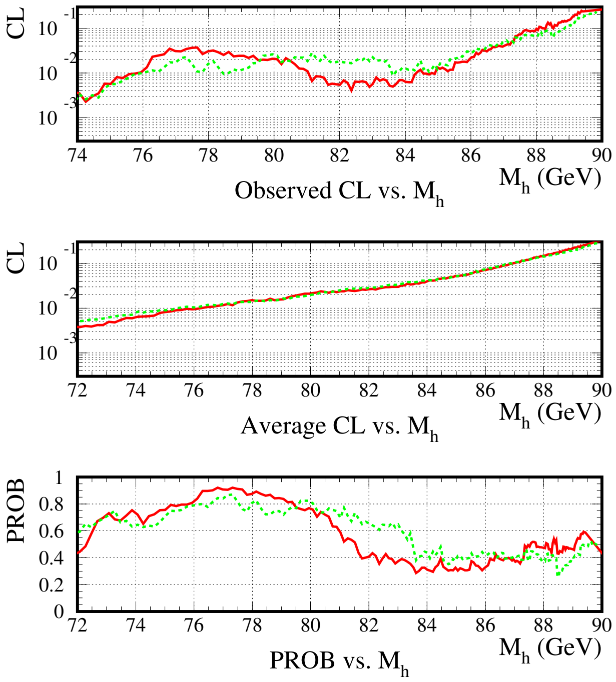

Figure 80: From top to bottom: The observed confidence level; The average confidence level; The probability of observing a confidence level larger than the one observed. The neural network $\mathrm{Hq\bar{q}}$ analysis (Section 3.3) is shown as the dashed lines, and the optimised cuts $\mathrm{Hq\bar{q}}$ analysis (Section 3.2) is shown as the solid lines. For the calculation of these curves, the same analyses other than $\mathrm{Hq\bar{q}}$ were used.

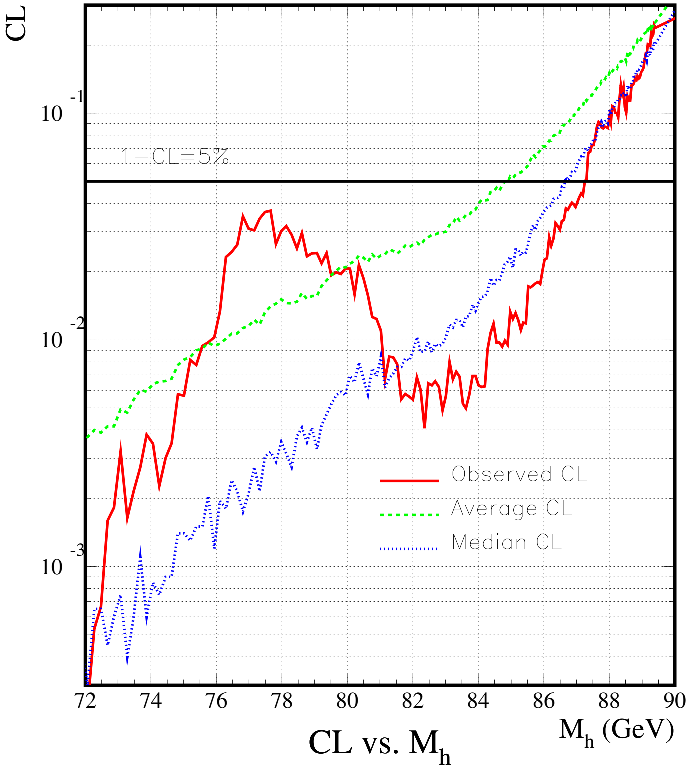

Figure 81: The lower limit on the Standard Model Higgs mass using the analyses listed in Section 7.3 is found to be 87.3 GeV.

References

[1] J. Branson et al., "Search for the Standard model Higgs Boson at LEP2", L3 note 2086;
J. Branson et al., "Final results on the Standard Model Higgs Boson at 161≤ $\sqrt{s}$ ≤ 172 GeV", L3 note 2107.

[2] **L3** Collaboration, M. Acciarri *et. al.*, "Search for the Standard Model Higgs boson in e^+e^- interactions at 161 GeV≤ $\sqrt{s}$ ≤ 172 GeV", *Phys. Lett.* **B411** (1997) 373–386.

[3] J. Branson, A. Dominguez, I. Fisk and G. Raven, "UCSD B-tagging in 1996", L3 note 2108.

[4] F. Filthaut, D. Bourilkov and V. Briglevic, "A Comparison of 1995 L3 Vertex Data with LEP BOM and QS0 Measurements", L3 note 1943.

[5] Alvise Favara and Marco Pieri, "New Method of Analysis Optimization," L3 note 2066.

[6] "Search for the Standard Model Higgs Boson in $\mathbf{e^+e^-}$ Interactions at $\mathbf{\sqrt{s} = 183}$ **GeV**," L3 collaboration, CERN-EP/98-XXXX. *Submitted to Phys. Lett. B.*

[7] M. Acciarri *et al.*, L3 Collaboration, Phys.Lett. **B 413** (1997) 191.

[8] M. Acciarri *et al.*, L3 Collaboration, Phys.Lett. **B 385** (1996) 454.